

LIFE OF A PHOTON IN X-RAY SPECTROSCOPY

Jens Uhlig

Doctoral Thesis
2011



LUND UNIVERSITY

LIFE OF A PHOTON IN X-RAY SPECTROSCOPY

© 2011 Jens Uhlig
All rights reserved
Printed in Sweden by Media-Tryck, Lund, 2011

Division of Chemical Physics
Department of Chemistry
Lund University
P.O. Box 124
SE-221 00 Lund
Sweden
<http://www.chemphys.lu.se>

ISBN 978-91-7422-284-5

"The beginning is the most important part of the work."

Plato

The Republic

ABSTRACT

This thesis summarizes the experimental work in which an ultrafast X-ray laser plasma source was combined with various scalable direct detection schemes to test a novel approach for lab-based time-resolved X-ray absorption spectroscopy. A laser plasma source based on a water jet target was built and commissioned. X-ray and electron emissions of this source were characterized with various direct detection schemes. The procedures for spectral retrieval with direct detection CCD's were optimized with regard to the laser plasma source. The novel approach of using a single photon measuring cryogenic microcalorimeter array as a high-resolution ($\Delta E/E \approx 2000 @ 6 \text{ keV}$) energy-dispersive detector was investigated. The potentially very high quantum efficiency, large detection angle and straightforward scalability make this device an interesting photon analyzer for low photon yield experiments. In this thesis a prototype version of this detector was built (in cooperation), implemented and commissioned into the laser plasma setup. With this combination of a lab-based broad-band source and the free standing microcalorimeter spectrometer high resolution X-ray absorption spectra in transmission mode were achieved. The thesis presents the first hard X-ray absorption fine structure (XAFS) spectrum taken with this novel approach and discusses further improvements and applications.

POPULÄRVETENSKAPLIG SAMMANFATTNING

Denna avhandling ger en introduktion till laser-plasmaröntgenkällor och olika direkta detektionsmetoder sammankopplade till en laboriebaserad uppställning för tidsupplöst röntgenabsorptionsspektroskopi. Molekylär funktion innebär att molekyler uträttar arbete genom strukturförändringar. Tidsupplöst röntgenabsorption kan i realtid följa dessa strukturförändringar och därmed bidra till förståelse och optimering av processer och material. Tillämpningarna sträcker sig från organiska solceller över artificiell fotosyntes till ljusaktiverade kemiska reaktioner.

I många storskaliga faciliteter (tex synkrotronanläggningar) över hela världen används röntgenabsorptionsspektroskopi som ett verktyg för att undersöka molekylära strukturer. Antalet anläggningar som erbjuder ultrasnabb tidsupplöst spektroskopi för studier av kemisk dynamik är mycket begränsat. Detta skapar ett stort behov av laboriebaserad utrustning som medger sådana experiment.

Intensiva laserpulser fokuserade på ytan av ett material genererar kortvariga pulser av högenergetisk, s.k. hård, röntgenstrålning med ett brett spektrum. Braggreflektion, den klassiska metoden för att analysera ett röntgenspektrum, ger med dess smala energiacceptans mycket låg transmission av röntgenfotonerna och är därmed en mycket ineffektiv analysmetod. Detta blir särskilt problematiskt för den lågintensiva isotropa röntgenstrålningen genererad med vår laserplasma källa. För att förbättra effektiviteten undersöktes och optimerades olika direkta detektionsmetoder med fokus på absorptionsspektroskopi.

I avhandlingen introduceras en ny typ av supraledande detektor som registrerar enskilda röntgenfotoner genom att mäta den värme de utvecklar. Med denna detektor uppmättes de första röntgenspektra med hög upplösning. Framtida utveckling och förbättring av denna nya detektor presenteras och visar lovande framtidsutsikter.

LIST OF PUBLICATIONS

This thesis is based on the following papers, which will be referred to by their Roman numerals in the text.

I A broadband laser plasma x-ray source for application in ultrafast chemical structure dynamics.

W. Fullagar, M. Harbst, S. Canton, J. Uhlig, M. Walczak, C.-G. Wahlström, V. Sundström.
Review of Scientific Instruments **78(11)**, 115105 (2007).

II The use and characterization of a backilluminated charge-coupled device in investigations of pulsed x-ray and radiation sources.

W. Fullagar, J. Uhlig, M. Walczak, S. Canton, I. Maasilta, V. Sundström.
Review of Scientific Instruments **79(10)**, 103302 (2008).

III Lab-based Ultrafast Molecular Structure

W. Fullagar, J. Uhlig, N. Gador, K. Kinnunen, I. Maasilta, C.-G. Wahlström, V. Sundström.
AIP Conference Proceedings **1234(1)**, 919-922 (2010).

IV Laser generated 300 keV electron beams from water

J. Uhlig, C.-G. Wahlström, M. Walczak, V. Sundström, W. Fullagar.
Laser and particle beams **29-4**, 415-424(2011).

V Table-top ultrafast x-ray microcalorimeter spectrometry for molecular structure

J. Uhlig, W. Fullagar, J. Ullom, W.B. Doriese, N. Gador, S. Canton, K. Kinnunen, J. Fowler, C. Reintsema, D. Swetz, D. Bennett, G. Hilton, K. Irwin, D. Schmidt, V. Sundström.
Physical Review Letter **110(13)**, 138302(2013).

CONTENTS

1	Introduction	1
2	X-ray Generation	5
2.1	Basic principles of X-ray generation	5
2.2	Ultra short X-ray pulses produced in large scale facilities	6
2.2.1	Bending magnets and wigglers	7
2.2.2	Undulator, the "coherent" wiggler	8
2.2.3	Short pulses at large scale facilities	9
2.3	Pulsed lasers	11
2.3.1	Oscillator model	12
2.4	Lasers and optical setups used in experiments	13
2.4.1	High contrast, high power laser system	13
2.4.2	Laser used in the high repetition rate laser plasma source	14
2.4.3	Optical setup for time resolved absorption experiments	15
2.5	Laser-plasma X-ray source	16
2.5.1	Ionization	17
2.5.2	Plasma oscillation	18
2.5.3	Propagation in under-dense plasma	18
2.5.4	Plasma heating and generation of bremsstrahlung	19
2.5.5	Sample chamber, water jet target, debris protection and sample jet	21
2.5.6	X-ray flux considerations	23
2.5.7	X-ray optics with potential use in tabletop absorption spectroscopy with direct detection	24
3	Interaction	27
3.1	Main interactions	27
3.2	X-ray Absorption processes in spectroscopic methods	28
3.3	X-ray Absorption fine structure (XAFS) spectroscopy	30
3.3.1	Evolution of Ru-Pt and Ru-Pd catalysts upon optical excitation	31
3.4	Ultra fast experiments, filters and examples	32
3.5	First results	34
4	X-ray Detection	37
4.1	Introduction	37
4.2	Overview of X-ray detection schemes	38
4.3	Excitation cloud generation and energy resolution limit	39
4.4	Semiconductor detectors	41
4.4.1	Charge coupled devices (CCD)	41
4.4.2	Application of CCDs in the laser-plasma setup	44
4.4.3	Bragg optics	45
4.5	Cryogenic photon detection	47
4.5.1	Low temperature effects	49

4.5.2	Superconductivity	50
4.5.3	Microcalorimeter array basic principle	52
4.5.4	Types of thermometers	53
4.5.5	Transition edge sensor (TES)	54
4.5.6	TES readout	56
4.5.7	Multiplexing	57
4.5.8	Signal transport and amplification	60
4.5.9	Temperature and noise shielding	60
4.5.10	Data recording and synchronization	61
4.5.11	Temperature control system	62
4.5.12	Calibration lines	64
4.5.13	Data extraction, energy calibration and drift correction	65
	Abbreviations	69
	Appendix	71
	Vectorized single pixel analysis method	71
	Laser alignment procedure by Jens Uhlig January 2012	72
	References	77
	Acknowledgments	99
	Comments on the Papers	101

Papers

I	A broadband laser plasma x-ray source for application in ultrafast chemical structure dynamics.	105
II	The use and characterization of a backilluminated charge-coupled device in investigations of pulsed x-ray and radiation sources.	107
III	Lab-based Ultrafast Molecular Structure	109
IV	Laser generated 300 keV electron beams from water	115
V	Table-top ultrafast x-ray microcalorimeter spectrometry for molecular structure	117

INTRODUCTION

The life of a photon spans its "birth", or generation, over its "working life" during sample interaction, to its "death", resulting in observable consequences in a detector. This thesis introduces a highly efficient new way to analyze photons in ultrafast table top X-ray schemes, with a prototypical application in X-ray absorption spectroscopy. It discusses some of the consequences for the source, the interaction and the detection.

The optical, electrical and mechanical properties of any material are determined by its internal structure. Activating materials with light and understanding its effects is one of the big scientific challenges of these days. Breaking and formation of chemical bonds upon light activation is a very dynamic process involving the motion of electrons and nuclei. Brief pulses of light can freeze and temporally resolve these events and allow us a snapshot of an evolving structure¹. Investigating the evolution of molecular structures in real-time will aid the understanding of the properties and function of these materials, both in ordinary fundamental chemical processes, and when under coherent optical control. Figure 1.1 shows a schematic with a brief overview

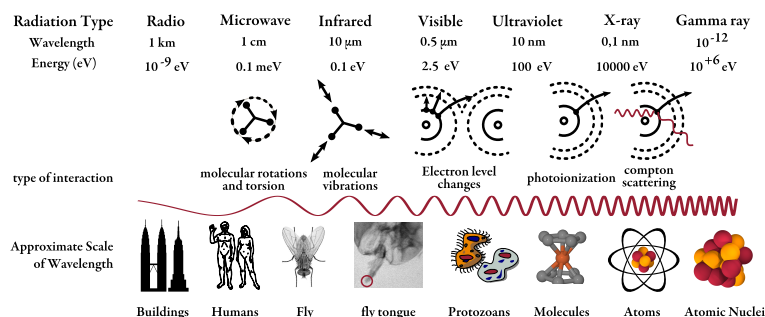


Figure 1.1. First row shows a schematic with length scales and corresponding photon energies. The next row gives the symbolic interactions that are typically excited by photons of this wavelength. That last row depicts objects with the typical size of this length.²

of the typical interactions excited by different wavelengths and some objects that show these length scales. Interatomic distances in condensed matter and molecules are of the order of Ångströms ($1 \text{ \AA} = 10^{-10} \text{ m}$). To probe structural changes in molecules wavelength of similar dimensions are needed^{3;4}. X-rays can be used to explore such molecular structures. In pump probe techniques a brief first pulse starts a reaction. Then after a period of evolution a second brief pulse takes a snapshot of the current state. This process is typically repeated in a stroboscopic experiment to acquire data of adequate quality. Laboratory based ultra-fast pump-probe capability is a particular incentive in this work. A variety of time resolved X-ray based techniques have been and are being developed to probe structural changes in matter⁵⁻¹⁰. This thesis focuses on X-ray absorption fine structure spectroscopy.

In chapter 2 sources for ultra-fast X-rays are presented. Large facilities were also visited and used in course of this work, whose operation is briefly described. The chapter also describes this work's development of a setup with a laser plasma X-ray source based on a water jet target for the generation of ultra-brief pulses of hard X-ray broadband radiation.

The characteristics of the source were chosen to match the direct detection approach in the novel combination of this "hot" source with a "cold" micro calorimetric direct detection array. Such detectors are in a rapidly maturing stage of international development, and our particular array is the focus of chapter 4.

In the closing months of this work the detector and the source were married for the first time. Chapter 3 presents the first promising results of this novel combination, as the "working life" aspect of the X-ray photon, and as the central aspect of this work.

This work started under the framework of the European MAXLAS project whose aim was to stimulate the cooperation between the different institutions of the MAX-lab synchrotron facility and the Lund Laser Centre. At the commencement of the presented thesis, X-rays had already been produced from metal target plasma sources at the Lund High-Power Laser Facility¹¹⁻¹⁴, the first versions of the water jet source were recently built and work to characterize it were underway (paper I). During my time systematic studies of the source emission and its optimization were carried out. A backilluminated CCD was used very extensively which in due course became the subject of a manuscript (paper II). The High Power Laser Facility had been carefully designed to have an excellent temporal contrast¹⁵⁻¹⁷ and this fact enabled a number of useful studies of electron beam generation and its relation to prepulses using the water jet source (paper IV). The perspective of high repetition rate readout with a simultaneously limited need of X-rays motivated the development of the new system designed to work together with a microcalorimeter based detection system. The microcalorimeter detector array

was built in cooperation with the Quantum Device Group at the National Institute of Standards and Technology in Boulder Colorado. The incentive brought by this thesis led to a new collaboration between this group, a research group in Jyväskylä (Finland) developing similar detectors and several groups within the JILA initiative in Boulder (USA) , resulting in a similar laser plasma microcalorimeter setup that will be built in early 2012.

Throughout this work, substantial time was devoted to the design, building, characterization and commissioning of the new plasma setup. This work also led to the design, building and commissioning of the detector periphery in Lund. It further developed part of the control and analysis techniques and codes for the cryostat and calorimeter. In addition, it measured and analyzed samples using the plasma source as well as potential samples at a few large scale facilities. The blend of optics, particle acceleration, chemistry, plasma physics, detector development and spectroscopy is highly multidisciplinary! This is reflected in this thesis, which had to deal with all those aspects. The unifying feature in this work is the "life" of the photon and the steps that can be taken to put them to use. An effort is made to present the life of the photon from its generation (birth), through the time it interacts with a sample to its detection (demise).

Paper **I** describes the stable X-ray emissions from our water plasma source. Paper **II** describes how a direct detection charge coupled device (CCD) can be used to calibrate, characterize and measure emissions from a laser plasma source. In paper **IV** a presentation of fast electron beams using a double pulse or temporally impaired pulse is given; this impacted the further developments of the X-ray source and also suggests new application based on the fast electrons. Paper **III** develops the idea of a microcalorimeter based setup and outlines some new ideas that will become possible with this unique combination. Manuscript **III** is still in preparation and presents the "first light" XAS spectrum measured using a laser-plasma and a microcalorimeter array.

X-RAY GENERATION

This chapter presents the generation or birth of ultrafast X-rays. Beginning with a general discussion about ultrafast X-ray generation the specific systems used will be investigated. The last sections are the theory, present status and some prospective developments for the laser plasma setup that was built during this thesis.

2.1 Basic principles of X-ray generation

X-rays were discovered by Wilhelm Conrad Röntgen in 1895¹⁸. He observed a penetrating radiation from the anode of a discharge tube, using a fluorescent screen and later photographic film. Most modern sources of hard radiation work on a similar principle. Charged particles are made to interact with strong electrical and/or magnetic fields to achieve a strong acceleration. Electrons have a favorable charge/mass ratio and most technical sources of hard X-ray radiation are based on them.

The emission of X-rays can be understood as a transition of a charged particle from a higher energetic state to a lower state. In a simple picture a free electron being decelerated from a high kinetic energy to a lower kinetic energy performs such a transition and emits a photon. If both states correspond to bound states the emitted spectrum will have a discrete and narrow distribution. The transition energies are characteristic for the emitting atoms. X-ray emission spectroscopy uses these spectra to obtain information about the energetic levels of bound states. Vacancies in deeply bound states of atoms are generated by ionizing radiation (e.g. X-rays or electrons see chapter 3), multi-photon absorption (see section 2.5.1) or capture of an electron in the nucleus during a radioactive decay process (see section 4.5.12). If an unbound electron in a material is captured into a bound state the emitted excess energy is the characteristic line energy broadened

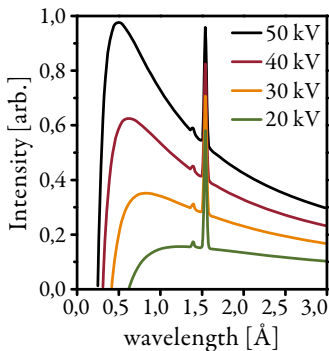


Figure 2.1. Simulated copper bremsstrahlung spectrum with artificially broadened characteristic lines.

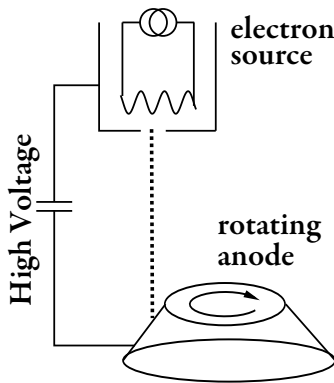


Figure 2.2. Principle of rotation anode X-ray tube. Constantly replacing the target material increased the power densities on the target before the structures started to melt. Even smaller target sizes can be achieved by using liquid targets like laser plasma sources^{11–13}.

by the thermal electron distribution and phononic/electronic excitations.

A fast electron striking a thick material undergoes a cascade of stochastic processes and transfers most of its energy into material excitations and finally the lattice (see section 4.3). During each step a part or all of the energy can be emitted as photon forming the so called "bremsstrahlung" (braking radiation) spectrum. The initially fast electrons can excite core electrons which give rise to characteristic line emission. The observable spectrum is the sum of both bremsstrahlung and line spectra (figure 2.1). The efficiencies depend on material, electron energy, temperature and have been studied since the early days of X-ray spectroscopy^{19–25}.

Most of the electron energy is converted into heat in this cascade. Medical or scientific applications which desire high fluxes on small foci need to dissipate higher power densities than any solid material can withstand. Examples of schemes to relieve the target material are to rotate the anode (figure 2.2) and give it time to cool, to use liquid metal target jets hit by electron guns^{26,27} or to use a variety of other movable target systems and a laser plasma source.

X-ray tubes are the most widespread sources for hard X-ray generation. We will revisit them while discussing table top sources of pulsed X-rays in section 2.5.4. In contrast to these stochastic processes the electron trajectory and angular acceleration is highly controlled in modern large scale research facilities (section 2.2).

2.2 Ultra short X-ray pulses produced in large scale facilities

Gaining control over the path of the charged particles and its acceleration enabled a huge jump in the quality and amount of emitted radiation. Electrons are accelerated to relativistic energies and guided once or repetitively through a bent trajectory. The acceleration during the bend stimulates the emission of radiation. The very first of these devices synchronously accelerated an electron beam in a circular motion in a permanent magnetic field, with the constant emission of radiation. The next generation of ring shaped storage facilities introduced local magnetic fields breaking up the circular motion into several smaller bends linked by straight sections (figure 2.3 a). In the straight sections the electron bunch can be accelerated to compensate for the radiation loss, reshaped in chicanes for recompression, or guided through the insertion devices. During the bends controlled emission occurs^{28,29}.

Electron bunches can be generated by many methods including emission from hot cathodes (the classical glowing wire), field

emission from a cold cathode or via photoemission from a photocathode excited by an optical pulse. The latter method is often preferred by modern facilities built to generate very short and temporally controlled pulses for femtosecond X-ray sources³⁰. After extraction the electrons are rapidly accelerated to relativistic energies. Once at relativistic speed the electron bunch has (in its own frame of reference) not much time to feel the Coulomb repulsion and so remains compressed as seen in the laboratory frame. The acceleration is often done in radio frequency resonant structures as shown in figure 2.4. A radio wave is coupled into the cavities in the device so that energy is synchronously transferred as it moves along. A detailed description of the methods used to accelerate, shape and re-compress the bunches can be found in reference³¹.

2.2.1 Bending magnets and wigglers

The breakup of the circular electron motion into many small angular bends allows the use of stronger and smaller superconducting magnets and higher electron energy. Both lead to more intense and harder radiation. The schematic of the electron trajectory in figure 2.3 shows a section of a synchrotron ring. To each of the small bends an effective radius r can be assigned (figure 2.3 a):

$$r = \frac{\gamma m_0 v}{eB} \quad \text{with } v \approx c, \quad (2.1)$$

where m_0 is the classical mass of the electron, v its speed, e the elementary charge and B the magnetic field that asserts the Lorentz-force. For a correct description the relativistic energies require the correction factor γ .

$$\gamma = \frac{E_{\text{electron}}}{m_0 c^2} = \frac{1}{\sqrt{1 - (v/c)^2}} \quad (2.2)$$

In the observation plane of the synchrotron the electron moves in a straight line emitting linearly polarized light. Perpendicular to the plane the radiation has a circularly polarized component. The relativistic movement of the electron has the following effect. A electron on a linear path emits an energy flux density S shown in figure 2.5 a. For particles at relativistic velocities the Doppler shift introduced for observations in the laboratory frame of reference compresses the emitted radiation into a small cone with a total opening angle $\Phi \sim 1/\gamma$.

A typical bending magnet spectrum was generated for different field strength and electron energies in figure 2.6. The energy of maximum emission is often called the characteristic energy and is approximated by⁴:

$$E_{\text{characteristic}} [\text{keV}] = 0,665 \cdot E_{\text{electron}}^2 [\text{GeV}] \cdot B [\text{T}] \quad (2.3)$$

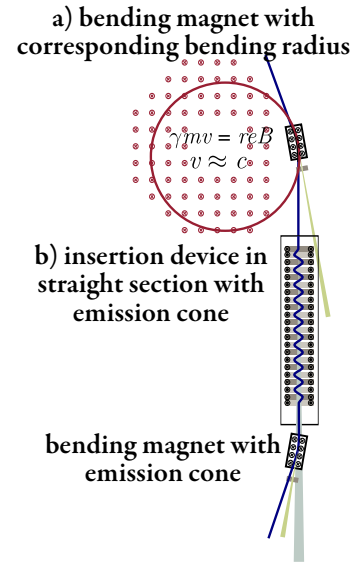


Figure 2.3. The original round synchrotron is broken up in bent and straight sections.

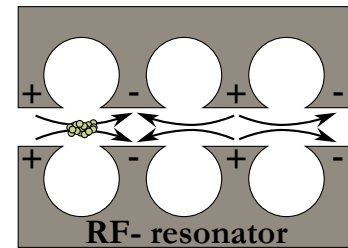


Figure 2.4. Schematic of radio frequency (RF) resonator for electron acceleration (Klystron). The surface charge inside the structure changes synchronously with the electron movement.

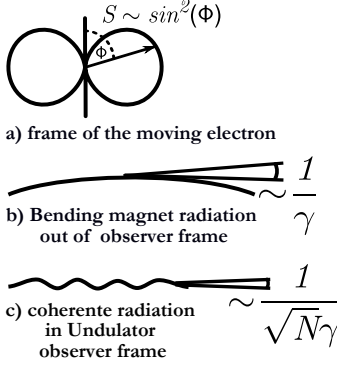


Figure 2.5. The relativistic Doppler effect³² compresses the wavefront in the frame of the observer along the direction of the moving electron. The resulting emission cone shows a strong compression in the forward direction. The coherent X-ray generation in an undulator compresses the cone even further.

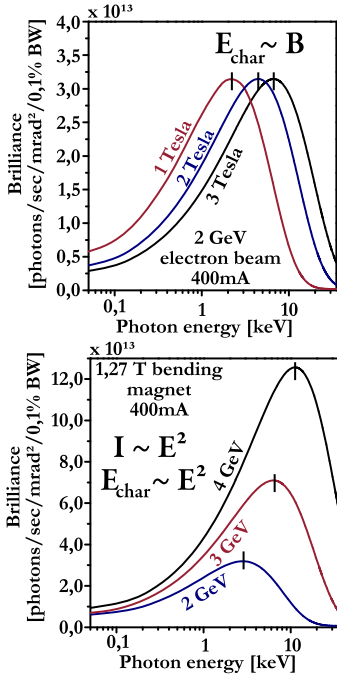


Figure 2.6. Emission from a bending magnet as function of energy and current

Bending magnets produce a broad spectrum with temporal duration only slightly longer than the electron bunch.

Since most experiments at synchrotrons use monochromatic radiation a convenient unit to compare the emission of different devices is the brilliance which is often stated in units of photons/second mrad⁻² 0.1% bandwidth.

Many small bending magnets brought close together force the electrons to execute a wiggling motion in the straight sections of the ring (figure 2.3 b). Modern wigglers use strong, often superconducting magnets and produce a broad spectrum. In figure 2.7 the path of the electron bunch through the wiggler follows several small bends. Considering only the emission of a single electron, at the same point of observation and energy we can write the phase information of the emitted electric field and the intensity in a qualitative way as follows:

$$E_{\text{single electron}} = \sum_{i=1}^{N_{\text{magnets}}} \cos(\omega t + \phi_i)$$

$$I_{\text{single electron}} = E^2 = \sum_{i=1}^{N_{\text{magnets}}} \cos^2(\omega t + \phi_i)^2 + \sum_{i \neq j}^{N_{\text{magnets}}} \cos(\omega t + \phi_i) \cos(\omega t + \phi_j) \quad (2.4)$$

There is no controlled relation between the position of the electron in the bends and the wavelength of the emitted hard radiation within the coherence length. The phase ϕ_i between the magnets and the radiation will therefore vary over 2π and the cross products vanish. Different electrons in the bunch have no fixed phase relation either and are therefore adding linearly to the summed intensity. Wigglers are built to produce a smooth and broadband radiation that scales like

$$I_{\text{wiggler}} \sim N_{\text{magnets}} * N_{\text{electrons}} \quad (2.5)$$

and offer a wide stable spectrum which extends often well beyond 20 keV. They are often the preferred choice in these energy regions.

2.2.2 Undulator, the "coherent" wiggler

In an undulator the electron pathlength is matched to multiples of the emitted wavelength. To fulfill this condition the (n-th multiple) wavelength λ_n of the emitted radiation must be on the order of the Doppler corrected undulator wavelength $\lambda_u/2\gamma^2n$. The electron follows a curved trajectory which is often described by its maximum angular deviation

$$K = eB_0\lambda_u/2\pi m_e c, \quad (2.6)$$

with the electron charge e , the magnetic field B_0 and the electron mass m_e . In an undulator the relative oscillatory amplitude A is smaller, and the bending radius larger, than in a wiggler. This leads to softer and less intense emitted radiation from each bend.

The often stated undulator coherence condition for the first order on the undulator axis is then:

$$\lambda = \frac{\lambda_u}{2\gamma^2} (1 + K^2/2) \quad (2.7)$$

The undulator wavelength λ_u is mechanically fixed but B_0 and consequently also K can be adjusted by varying the gap between the two magnet poles³⁴. For photons at the fundamental wavelength (or multiples of it) the phase factor in equation 2.4 is resonant.

$$I_{single\ electron}^h = \sum_{i,j}^{N_{magnets}} \cos(h\omega t + n_i h\pi) \cos(h\omega t + n_j h\pi) \quad (2.8)$$

For all uneven harmonics ($n=1,3,5$) the photons interfere constructively and lead to a $\sin(Nx)/\sin(x)$ interference envelope where N is the number of magnets. The even harmonics vanish (figure 2.7c). The intensity in this case scales as:

$$I_{undulator} \sim N_{magnets}^2 * N_{electrons} \quad (2.9)$$

This spectrally narrow flux can be guided through a monochromator to further limit the bandwidth. The opening angle is compressed to $1/\sqrt{N_{magnets}}$ compared to the natural linewidth $1/\gamma$ (figure 2.5 c). Variations like "tempering" (tuning to different wavelength at the begin and at the end of an undulator), circular polarized undulators and asymmetric magnetic structures are discussed in textbooks^{4;35}.

Note that the resonance wavelength has a squared dependence on the electron energy γ^{-2} (formula 2.7). A small change in the electron energy observed at the end of linear accelerators can result in a substantial shift of the center wavelength in the undulator. After the narrow bandpass of a monochromator the fluctuations are in the range of several percent and in many cases pose demand on the detector to resolve single pulses for normalization (see also chapter 4).

2.2.3 Short pulses at large scale facilities

In a classical storage ring the electron bunch is ≈ 3 cm long, corresponding to a duration of ≈ 100 ps. Several techniques have been developed to shorten the pulse duration of the generated X-rays to sub ps pulses.

Numerical example: Typical numbers are ≈ 100 magnets and 10^{11} electrons for a 1.2 km long ring with 100 mA and 24 equal bunches.

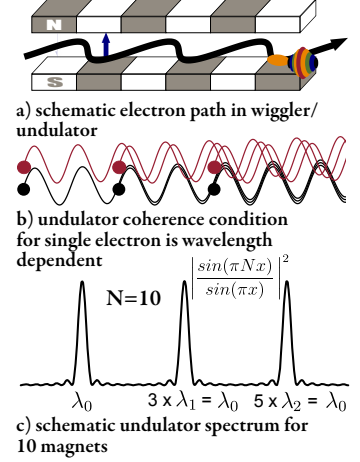


Figure 2.7. a: Oscillating movement of an electron through a periodic magnetic field. b: The coherence condition between electron movement and emitted radiation of periodic wavelength. c: schematic undulator spectrum for N magnets. Several codes like SPEC-TRA³³ are used to simulate the emission

Comment: The amplitude A of the oscillation and the smallest bending radius can be estimated by:

$$A = \frac{K\lambda_u}{2\pi\gamma}$$

$$r = \frac{\gamma\lambda_u}{K2\pi}$$

Numerical example: Assuming a 6 GeV electron beam the order of magnitudes are:

$$\begin{array}{lcl} \gamma & \approx & 10^4 \\ K & \approx & 1 \text{ for undulator,} \\ & \geq & 10 \text{ for wiggler,} \end{array}$$

For $K=1$

$$\begin{array}{lcl} \lambda_u & \geq & 1.5 \text{ cm} \\ \lambda & \approx & 0.8 \text{ \AA} \\ A & \approx & 0.2 \text{ \mu m} \\ r & \approx & 28 \text{ m} \end{array}$$

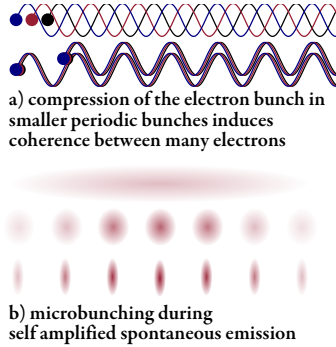


Figure 2.8. *a: Applying a coherence condition to the electron distribution within the bunch leads to constructive superposition of the emitted radiation. b: The induced electric field leads to a micro bunching and local compression of the electron bunch.*

Energy can be transferred from or into a strong optical laser field by parts of the electron bunch during the oscillatory movement in an insertion device. The small section (typically 100 μm) of the several cm long electron bunch has for a short time a slightly higher/lower energy and can be spatially separated in a dispersive section. The time and spatial structure of the electron bunch is then mimicked in a radiator into a X-ray pulse containing an ultrashort part in the wings³⁶. The flux achievable with these tunable sources is proportional to the fraction of "sliced" electrons.

Another approach for synchrotron based short pulses is a clever way to rotate the electron bunch by Zholents³⁷. In a time dependent field the horizontally stretched electron bunch is rotated, guided through an insertion device, and then rotated back. In the insertion device the temporal spread of the electron bunch is encoded in the divergence of the emitted X-ray beam. The X-ray beam is re-collimated and the resulting tilted wavefront is corrected in an asymmetric Bragg reflection. This device is currently implemented at the Advanced Photon Source (APS) in Argonne/USA³⁸ and a pulse duration as short as 1 ps at very high X-ray flux is expected.

Recently a new generation of X-ray facilities became available^{39–41}. Just as the optical laser could transfer energy to the electron bunch in an insertion device, the self generated radiative field can transfer energy into the electron bunch. The originally random emission of each electron in the bunch now becomes concentrated in these micro bunches (figure 2.8). The coherence condition of the emitted radiation is now met by a part of the electrons and very high emitted intensities can be reached⁴². For a perfectly compressed micro bunch the intensity would scale as $N_{\text{electrons}}^2$. Since the electron bunches vary slightly in phase the intensity scales:

$$I_{\text{undulator + modulated electron bunch}} \sim N_{\text{magnets}}^2 * N_{\text{electrons}}^{1 < x < 2}. \quad (2.10)$$

Self amplified spontaneous emission (SASE) electron bunches with typically 300 fs duration are guided into the undulator. The micro bunching effect is stronger with higher electron density. The compressing effect emphasizes therefore the central part of the bunch. The emitted pulse shows a central part as short as 50 fs on a broader background. The jitter between laser and X-ray pulse arrival is recorded for every shot. An overview over the available large scale facilities can be found in reference⁴³.

2.3 Pulsed lasers

A wave packet can be described as the sum of many modes with their wavevectors \mathbf{k} and the polarization σ whose phases overlap only during a short period of time:

$$\vec{E}(\vec{x}, t) = \sum_{\vec{k}\sigma} \hat{E}_{\vec{k}\sigma}(\vec{x}, t) e^{i(\vec{k}\vec{x} - \omega(\vec{k})t)}. \quad (2.11)$$

The summed electrical field has the fast oscillatory frequency of the center wavelength and with an overall envelop temporal and spectral shape. It is often assumed that the temporal envelope has the form of a Gaussian or hyperbolic secant (sech) function. The shortest possible temporal width τ of a pulse with these shapes is related to the bandwidth $\delta\omega$ by the time-bandwidth product (compare also figure 2.9):

$$\tau \cdot \Delta\omega \geq 2\pi c_B \quad \text{with } c_B \begin{cases} 0.441 & \text{for Gaussian shape} \\ 0.315 & \text{for Hyperbolic secant} \end{cases} \quad (2.12)$$

The electrical field for a linearly polarized, cylindrically symmetric pulse with temporal and spatial gaussian shape can be written:

$$E(t, r) = E_0 \cdot e^{-2\ln 2(t/\Delta t)^2} \cdot e^{-(r/\Delta r)^2} \cdot e^{i\omega t + iC(t)}. \quad (2.13)$$

Here Δt is the temporal width, Δr the cylindrical Gaussian width. $C(t)$ is generally called the chirp and represents the temporal distribution of the frequency components within the pulse. Many commercial laser systems designed for high power, short pulses use the very broad gain bandwidth of titanium doped sapphire (Ti:Saph) to amplify selected modes in a laser cavity. Double prism or dispersive mirror constructions allow a certain bandwidth to be amplified. An intensity dependent index of refraction changes the path in the cavity depending on the strength of the electric field and is used in our system to passively mode lock the cavity⁴⁴. The process of mode-locking is either started from noise or with help of "artificial noise" introduced by modulating optics^{45;46}. The output of these so called oscillators is a continuous train of pulses with relatively low energy (several nJ/pulse) and a repetition rate defined by twice the length of the cavity, usually on the order of 80 MHz.

The maximum power of pulsed laser systems increased dramatically when the chirped pulse amplification scheme was developed^{47;48}. The chirp in equation 2.13 is altered and the pulses are stretched in time (typically several hundred ps). The combination of a Pockels cell (see comment) and polarizing optics selects a few pulses from the pulsetrain into a second cavity.

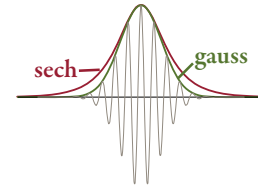


Figure 2.9. Fast oscillating electric field with Gaussian carrier function in comparison to hyperbolic-secant envelope

Q-switched or giant pulse lasers use a variable attenuator in the cavity that damps the spontaneous radiation below the lasing level. At one point in time the damping is removed and the built up population inversion can cause much stronger lasing than in a continuous wave laser with the same pump intensity

A *Pockels cell* is an electro optical module acting as a switchable half wave plate, which rotates a linear polarized laser pulse of the particular wavelength by 90 deg. For broadband pulses only a part of the pulse is rotated perfectly

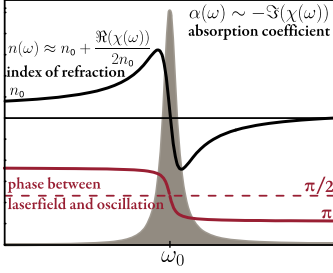


Figure 2.10. Principle behavior of the Lorentz oscillator model for the index of refraction (black), the phase between exciting wave and oscillator (red) and the absorption (grey)

Comment: indeed thin slices of light would be better since the bunches are typically 0.5 cm wide and only as thick a hair (30 μm for a 100 fs bunches)

The peak intensity of the stretched pulses is below the damage threshold of optics in the laser system, allowing optical amplification up to this point. Within the cavity each pulse is amplified over several round-trips in a second Ti:Saph crystal which is pumped by a Q-switched laser (see comment). After the pulse is coupled out by a second Pockels cell it is sometimes amplified further in multi-pass systems. In the last stage the introduced chirp is reversed to generate a short pulse of extreme intensity.

2.3.1 Oscillator model

A monochromatic light wave of angular frequency $\omega = 2\pi f$ transverses a material with the phase velocity $v_p = c/n(\omega)$, where n is the refractive index of the material and c the speed of light in vacuum. Each electron in the material acts as a forced resonator, oscillating in the external field (Lorentz oscillator model). In a non magnetic medium the index of refraction is $n(\omega) = \sqrt{1 + \chi(\omega)}$. The electric susceptibility χ combines the electrical field \mathbf{E} and the polarization density \mathbf{P} of an isotropic medium according to $\mathbf{P} = \epsilon_0 \chi \mathbf{E}$. Consider a dielectric medium where the oscillation of the electrons has its own resonance frequency ω_0 and is linearly damped by a factor σ . The susceptibility for this resonant system can be expressed as:

$$\chi(\omega) = \left(\frac{Ne^2}{\epsilon_0 m \omega_0} \right) \frac{\omega_0^2}{\omega_0^2 - \omega^2 + i\omega\sigma}. \quad (2.14)$$

N is the number of oscillators (dipoles), m the mass and e the elementary charge. In the vicinity of the resonance frequency the imaginary part of the susceptibility becomes large and with it the absorption. The width of the Lorentzian shaped absorption depends on the damping factor in the oscillatory system. The relative phase between the excitation and the polarization response shows a frequency dependent phase shift with a sharp step at the resonance. Already from this simple model (Figure 2.10) it is obvious that every material shows a dispersion ($dn/d\omega$). Short laser pulses have a spectral width around the center wavelength (e.g. $\Delta\lambda = 35 \text{ nm}$ for our pulses). The different components of the bunch travel with the group velocity:

$$v_g(\omega) = \frac{d\omega}{dk} = \left(\frac{n}{c} + \frac{2\pi}{\lambda_0} \frac{dn}{d\omega} \right)^{-1} \quad (2.15)$$

Dispersion in the group velocity will change the chirp in the pulse, meaning that the phases of different wavelength walk apart and the pulse can stretch non linearly. The typical method of calculating the linear dispersion in media is by use of the Sellmeier equations. The empirical relationship between wavelength

and refractive index is tabulated for most commonly used materials. Table 2.1 shows literature values for the materials relevant in the table top plasma source.

The effect is strong for the coherence length in non linear crystals like $\beta - BaB_2O_4$ (BBO). In the case of frequency doubling in BBO from 800 nm to 400 nm the walk off is in the order of 15 fs per 100 μm crystal and strongly limits the usable gain length. The efficiency of second harmonic generation in non linear crystals can be expressed $\eta_{SHG} = C^2 L^2 P / A$, where P is the power per area A , L is the crystal length, and C is a constant that depends on the active mode area. For higher intensities this linear model does not hold and non linear effects with an intensity dependent index of refraction $n(I)$ like the Kerr effect⁴⁶ and relativistic effects (see also section 2.5) have to be considered.

Table 2.1. Sellmeier equations for the materials relevant in this thesis

Material	Sellmeier equations wavelength [μm]	range [μm]
Fused Silica ⁴⁶	$n^2 = 1 + \frac{0.6962\lambda^2}{\lambda^2 - (0.06840)^2} + \frac{0.4079\lambda^2}{\lambda^2 - (0.1162)^2} + \frac{0.8975\lambda^2}{\lambda^2 - (9.8962)^2}$	0.21-3.71
BBO ⁴⁶	$n_o^2 = 2.7359 + \frac{0.01878}{\lambda^2 - 0.01822} - 0.01354\lambda^2$ $n_e^2 = 2.3753 + \frac{0.01224}{\lambda^2 - 0.01667} - 0.01516\lambda^2$	0.22-1.06
HPLC water at 20°C ⁴⁹	$n^2 = 1 + \frac{0.5684\lambda^2}{\lambda^2 - (0.005101)^2} + \frac{0.1726\lambda^2}{\lambda^2 - (0.01821)^2}$ $+ \frac{0.02086\lambda^2}{\lambda^2 - (0.02621)^2} + \frac{0.1131\lambda^2}{\lambda^2 - (10.697)^2}$	0.182-1.12

2.4 Lasers and optical setups used in experiments

The measurements presented in this thesis were performed using different laser systems.

2.4.1 High contrast, high power laser system

The development, calibrations and effects around the laser plasma source were done using a parasitic beam of the multi-terawatt laser of the Lund Laser Center (LLC)¹⁵. This system has an 80 MHz Ti-Sapphire mode-locked oscillator with preamplifier, spectral cleaning with an acoustic wave pulse shaper (Dazzler) and extra Pockels cells outside the regenerative amplifier for additional temporal contrast improvements. After the regenerative amplifier the pulse is guided through a multipass amplifier. At this stage the parasitic beam used by us was coupled out and compressed. The output to our setup was 800 nm, 40 fs, 80 mJ, 10 Hz and a very high contrast ratio $>10^6$: 1 towards the leaked amplified spontaneous emission (ASE) background and pre-pulses. The system has been described in greater detail elsewhere^{16;17;50-52}.

2.4.2 Laser used in the high repetition rate laser plasma source

The system built by "Spectra Physics" is based on a short pulse Kerr lens modelocked Ti:sapphire "Tsunami" oscillator. The "Tsunami" is pumped by 4 W CW 532 nm generated by a frequency doubled LiB_3O_3 (LBO), diode pumped $Nd : YVO_4$ (Neodymium doped yttrium vanadate) laser (market name "Millenia"). The oscillator output is 80 MHz, 500 mW, 55 nm wide and chirped to 500 fs. The amplifier system is sketched in figure 2.11. The Tsunami output is stretched to 200 ps and a 1 kHz sub multiple of the 80 MHz is coupled into the regenerative amplifier.

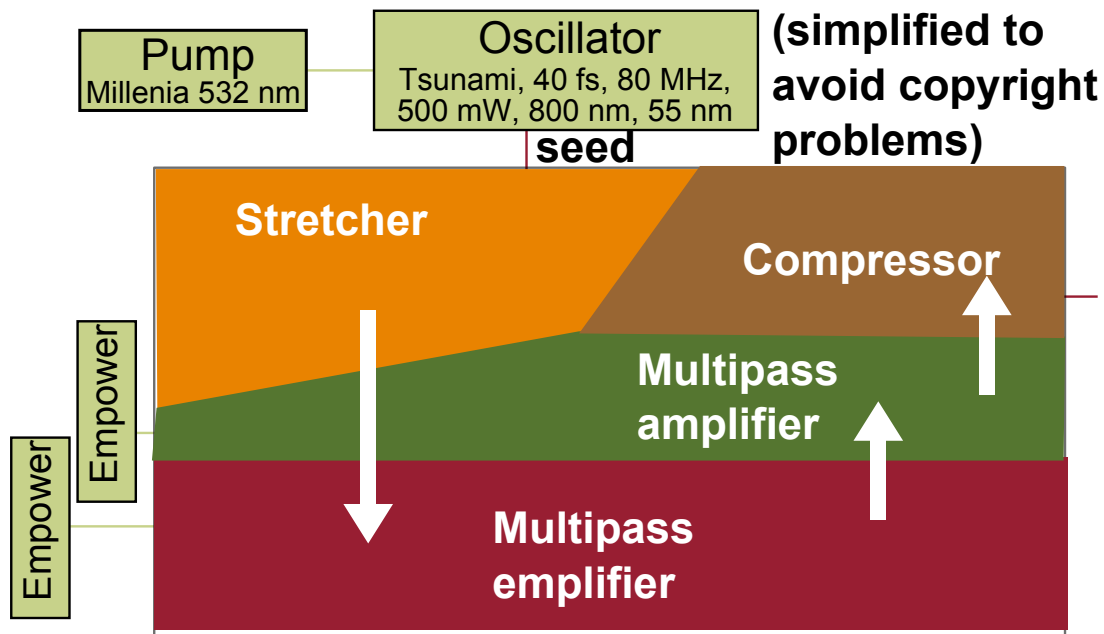


Figure 2.11. Amplified laser system used for the table top X-ray source. The regenerative amplifier (blue beampath) is built with a half wave plate (Pol) one Pockels cell (P2) and a half wave plate (HW). The amplifier is seeded by a Spectra Physics Tsunami Ti:Sapphire oscillator (red path) and pumped by two doubled Nd:YLF Empower diode lasers (green path). For more details see text.

The regenerative amplifier (blue beampath) is built with a polarizer (Pol), one Pockels cell (P2) and a half wave plate (HW). By switching the polarization within the Pockels cell (P2) the cavity can be closed and opened. The reflectivity of the polarizer, the effect that the a half wave plate is only optimal for the center wavelength and the quality and alignment of these elements define the temporal contrast ratio in this amplifier. The Ti:sapphire crystal is pumped by a frequency doubled Q-switched 1053 nm

Nd:YLF laser. During the time of the described experiments the crystal was pumped from two sides.

In an optimally aligned system we reach contrast ratios of $1:10^3$ towards ASE and prepulses (a damaged or missaligned Pockels cell can lead to a decreased contrast ratios of about 1:10). The pulse is further amplified in a separately pumped double pass amplification system to 6.8 mJ (before compression). The beam diameter is adjusted in the lens telescope T and the previously introduced chirp is reversed. The total output of the system is ≈ 6 mJ, 40 fs at 800 nm. The contrast ratio, quality of the beam and stability is of huge importance for the intended usage. Internal beam movements due to damaged optics and thermal instabilities introduced the misalignment of Pockels cells, astigmatism generated in the optics and crystals, power and beam pointing fluctuations. A big challenge and still work in progress was to stabilize this commercial system. Since the processes during the X-ray generation are highly non-linear all fluctuations are amplified and can lead to noise in the best, hazardous situations in the worst case (see section 2.5.4 and paper IV).

2.4.3 Optical setup for time resolved absorption experiments

The optical components after the amplifier are shown in figure 2.12. The polarization of the main 800 nm beam is adjusted in a rotatable quartz $\lambda_{1/2}$ waveplate and split by two Brewster type polarizers. The polarization separation is better than 1:100 for the transmitted beam (pump beam) and 1:500 for the reflected beam (X-ray generating beam). The pump beam is delayed on a 13 ns delay line with 5 fs step size and ± 40 fs hysteresis. The full size beam is frequency doubled in a 200 μm thick BBO crystal and cleaned with two dichroic mirrors (high reflector for 400 nm and very weak reflector for 800 nm) to less than 5% remaining IR radiation and focused on the sample. The transmitted infrared beam after the first dichroic mirror is used to record the presence of the pump beam.

The probe beam is expanded through a 1:2.5 telescope and focused by a 90° off axis parabolic mirror (made by Janos Inc.) onto the water jet target. The off axis parabolic mirror has two foci if not perfectly aligned or if the beam shows astigmatism¹³. Two close foci can generate conditions similar to temporal double pulse structures and can give rise to the generation of high energetic electron beams (see paper IV).

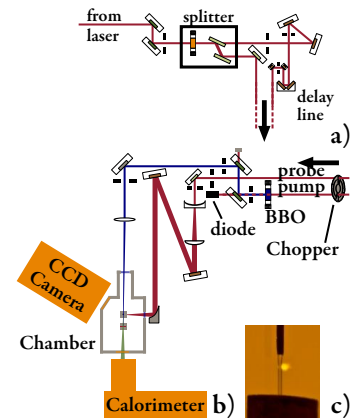


Figure 2.12. Optics setup for the table top XAS. a) The laser beam is split with a variable beam splitter. b) The repetition rate can be adjusted by a coupled chopper for pump and probe beam. The pump beam is converted into 400 nm, cleaned by two dichroic mirrors and focused into the chamber. The leakage from the first mirror is measured by a photodiode that will be fed into the detector to link pump and un-pumped datapoints. The X-ray generating beam is reflected over a 90° off axis parabolic mirror onto the water jet. c) The plasma is formed tangentially on a 160 μm water jet.

2.5 Laser-plasma X-ray source

Photon densities and electrical fields in the focal point of the pulsed laser reach intensities only found in extreme environments like lightning or centers of stars. At these intensities atoms and molecules are nearly instantaneously ionized. In this highly non linear regime particles are accelerated and can undergo a variety of processes including harmonic generation, the driving of plasma wakes, and different scattering processes. A number of recent textbooks⁵³⁻⁵⁸ and review articles^{8;59-62} cover the wide field of ultra fast laser-matter interaction and X-ray generation. I will focus on some interactions and aspects relevant for the work with a laser plasma X-ray source that is used for X-ray absorption spectroscopy. A quick and incomplete overview of laser driven X-ray sources would include the following:

Wake field acceleration A high intensity laser can generate collimated and mono energetic electron beams and particle beams^{61;63}. The accelerated electrons can be trapped in the plasma wake, wiggle in the driving laser field and generated table top synchrotron radiation⁶⁴. It was suggested and shown that these mono energetic electrons⁶⁵ and fast particles can be injected in small undulators^{66;67} or be used to drive Compton⁶⁸ or Thomson⁶⁹ sources.

Plasma source Intense laser fields interact with steep plasma density gradients to generate and heat plasma. The electrons in this plasma interact with matter to form bremsstrahlung or characteristic line radiation.

Laser driven X-ray diode A small bunch of electrons is generated by a short laser pulse from a photocathode. These are then accelerated by a strong electric field onto a classical anode^{70;71}.

High harmonic generation A strong laser field distorts the potential of an atom so that at a controlled point electrons lost by the atom are returned to the atom when the field reverses. The electrons gain energy in the laser field, fall back in their ground state and emit a photon having the energy of the ionization potential, plus the energy gained in the field. The process repeats itself with the emitted photon. With strong laser pulses photons well beyond 2000 times the fundamental wavelength have been observed⁷²⁻⁷⁵.

Compton scattering The inverse Compton effect can transfer energy to optical photons scattered on fast electrons generated at synchrotron or laser sources and high energy x- and gamma radiation can be emitted. The efficiency is low and very large photon densities are needed^{68;76-78}.

Thomson scattering This source works in the low energy limit of Compton scattering. The oscillatory field of a strong laser pulse interacts directly with an intense electron beam. The oscillating electrons emit radiation similar to a wiggler. The achievable flux is very small, but the reported emission is on the order of the laser pulse duration⁷⁹.

2.5.1 Ionization

The energy of an 800 nm photon is often not sufficient to ionize an atom or lift an electron from the valence (or highest occupied level) to the conduction band (lowest unoccupied level) in an isolator. Electrons in the conduction band or free electrons with sufficient energy can ionize molecules and excite further electrons into the conduction band. This collisional ionization can lead to an avalanche effect when the sum of field ionization rate and collision rate is larger than the recombination rate⁵⁴.

For the initial ionization the two main models are multi photon ionization and field ionization. Which of the two processes dominates is determined by how much energy the electron gains during its oscillation in the laser field (and is related to the resonance absorption discussed above in section 2.3.1). The average oscillatory energy (ponderomotive energy⁸¹) one electron has if its resonance frequency in the atom field is ω_e is:

$$U = e^2 E^2 / 4m_e^2 \omega_e^2. \quad (2.16)$$

To determine which process is dominating, one has to consider the ionization potential I_p of the atom. The dimensionless Keldysh parameter⁸² $\Gamma = \sqrt{I_p / 4U}$ is an estimate of the threshold between the two effects. For high frequencies and/or low electric field strength the ponderomotive energy is small and $\Gamma \gg 1$. Multiphoton ionization is the dominant absorption process in this regime. At high intensities many photons can simultaneously interact with the atom and the electric field can be understood as a distortion of the potential barrier (see figure 2.13 and the comment under to it). The electron can tunnel through the barrier or if the distortion is large enough and the barrier is suppressed go "over-the-barrier"^{54;83}.

Tunnel ionization is the basis for the coherent generation of high harmonics. The electrons tunneling through the barrier can gain energy from the laser field and be recaptured, and emit a photon of higher energy. The process inherits the coherence of the driving laser field. This is a very active area of research and the control of phase and ionization has enabled groups to generate harmonics in the hard X-ray range⁷².

Numerical example: A pulse of 30 fs with 3 mJ, focused to a waist diameter of 10 μm has $\approx 10^{17} \text{ W/cm}^2 = 10^{21} \text{ W/m}^2$ compared to 1 kW/m² of average sunlight and contains $\approx 10^{16}$ photons, assuming a wavelength of 800 nm or 1.5 eV photons energy. For linearly polarized light the electrical field is:

$$E = \sqrt{2I / \epsilon_0 c} \approx 1 \cdot 10^{12} \text{ V/m}$$

with c the speed of light and ϵ_0 the permittivity in vacuum. Compared to this the Coulomb field of the first Bohr radius of hydrogen⁸⁰ is

$$E_{\text{bohr}} = \frac{e}{a_0^2} \cdot \frac{1}{4\pi\epsilon_0} \approx 5 \cdot 10^{11} \text{ V/m}$$

where e is the elementary charge and a_0 the first Bohr radius

$$a_0 = 4\pi\epsilon_0(\hbar^2) / (me^2) = 5.3 \cdot 10^{-11} \text{ m}$$

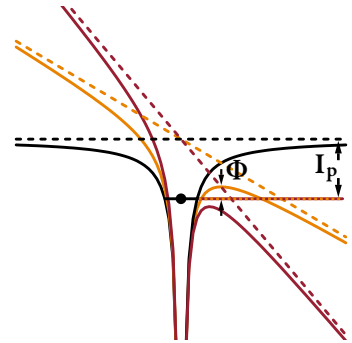


Figure 2.13. Schematic drawing of the tunnel ionization process. I_p is the ionization potential for the undistorted potential (black). Under the electrical field the potential distortion generates a potential well of height Φ through which the electron can tunnel (gold). For an even stronger electrical field the potential distortion might become large enough that no potential barrier remains and the electrons then can flow freely (red).

Comment figure 2.13 An estimate for the electric field can be made by a linear Coulomb potential:

$$V_{coul}(x) = (-Ze^2)/(4\pi\epsilon_0 x)$$

modified by a homogeneous electrical field to:

$$V_{total}(x, t) = V_{coul}(x) - eE(t)x$$

The barrier is the ionization potential (I_p) minus the maximum of this curve. Here one can define an apparent laser intensity for each bound state at which this barrier would be low enough for direct ionization⁵³:

$$Int_{app} = \frac{\pi^2 c \epsilon_0^3 I_p^4}{2Z^2 e^6}$$

, where Z is the charge of the generated ion, e the elementary charge and c the speed of light. For typical gases:

Ion generated	I_p [eV]	Int_{app} [Wcm^{-2}]
He ⁺	24.59	1.4×10^{15}
N ⁺	14.53	1.8×10^{14}
N ⁵⁺	97.9	1.5×10^{16}
O ⁺	13.6	1.3×10^{14}
O ⁶⁺	138.1	4.0×10^{16}

2.5.2 Plasma oscillation

In the laser focus of a plasma source the ionized particles form a strongly inhomogeneous plasma with a high degree of ionization. The strong electric fields locally disturb the condition of neutrality. The mobile and light electrons, once ionized, oscillate in the Coulomb potential of the heavier and less mobile ions with the (Langmuir) oscillation frequency⁵³:

$$\omega_p^2 = \frac{e^2 n_e}{m_e \epsilon_0}. \quad (2.17)$$

Here n_e is the free electron density, m_e the electron mass and e the elementary charge. The energy transfer from the driving electrical field to the oscillator is maximum at the resonance frequency (see oscillator model section 2.3.1) and due to the phase shift this layer acts as a perfect mirror. Assuming the existence of a density gradient, a laser can penetrate the plasma until the critical density, where $\omega_p(n_e) = \omega_{laser}$ is reached.

2.5.3 Propagation in under-dense plasma

Several other important effects can be understood from the Langmuir frequency. For the experiment the index of refraction is:

$$n \approx \sqrt{1 - \omega_0^2 / \omega_{laser}^2}. \quad (2.18)$$

By considering also equation 2.17 we see that with increasing ionization the index of refraction decreases in regions with higher intensity (higher degree of ionization). Assuming a spatial intensity variation like described in equation 2.13, the effective higher speed in the middle of the beam turns the wavefront and leads to de-focusing. Focusing optics with focal length f and an initial beam diameter of R normally have a minimal possible focal diameter of $D = 2f\lambda/\pi R$. Intensity de-focusing limits this focal parameter further if the ionization threshold is reached. This motivates the use of gases with lower ionization threshold, or evacuation leading to a reduction of the attainable electron density (see comment in section 2.5.1). This effect decreases the area of the confocal parameter $\sim (4\pi f/R)^2$ and with this the interaction length.

In the water plasma source presented here the vacuum pressure is limited by the water vapor pressure. The water is degassed and in some cases cooled below room temperature to be able to further reduce the pressure. During the experiments the chamber is constantly flushed with helium to obtain a higher ionization threshold. Plasma sources based on materials with lower vapor pressures can reach higher laser intensities in the focal area and generate higher electron temperatures (see section 2.5.4).

The quiver movement of electrons in a very strong electric field can require a relativistic correction of the electron mass if the laser field is intense enough. The effective resonance frequency becomes $\omega_{corr}(I) = \omega_0/\gamma$ and is higher in areas with larger field strength. Following a similar argument as before, this process may generate a self focusing effect⁸⁴. Balancing these and several other not previously mentioned effects like (Raman and Thomson light scattering¹²), light can be guided in a self generated plasma channel over long distances⁸⁵. Processes like white light generation^{55;86-88}, self compression⁸⁹, guiding of electrical discharges and lightning⁹⁰ and laser driven plasma waves in self guided channels or capillaries^{61;91;92} use these effects.

2.5.4 Plasma heating and generation of bremsstrahlung

The laser heating of a plasma has been studied for many years^{53;54;58}. In laser plasma sources the plasma is generated at the steep interface between a high density target and an area of lower density. A gradient of temperatures and densities is formed. The leading edge of the laser pulse hits an intact surface and starts the partial ionization. Nuclei in the plasma move roughly with the speed of sound in practical units⁵³

$$c_{ion} \simeq 0,31 \sqrt{(T_e/keV) \cdot (Z_{eff}/A)} \text{ } \mu\text{m ps}. \quad (2.19)$$

Here T_e is the electron temperature in keV and Z_{eff} the effective charge normalized by the atomic number. The expansion resulting from this speed is small during a single high contrast pulse of 50 fs. For optically impaired temporal contrast (see section 2.4) or deliberately generated pre-pulses with several picosecond delay (paper IV), the heavier particles in the plasma have time to expand and generate a plasma and temperature gradient spreading, over a much wider range (plasma scaling length)^{53;93-96}. At the intact plasma surface collisional absorption processes dominate the energy absorption at lower intensities of $\approx 10^{12} - 10^{14} \text{ W/cm}^2$ ^{53;58}. Several collisionless absorption mechanisms are suggested for higher laser intensities^{53;54;58;97-99}. One dominant process at the undisturbed density surface is the vacuum heating mechanism named after Brunel¹⁰⁰⁻¹⁰² which was extended to shorter pulses by Gibbon⁹⁹. In this mechanism the p-polarized field extracts electrons from areas with high electron density and accelerates them during the opposite electric cycle back into the area of high density. Complex collective events for p-polarized light have been calculated using particle in cell (PIC) codes that can generate a superheated fraction of electrons. The total intensity spectrum is often presented with a bi-Maxwellian distribution^{53;103}. A common feature for many theoretical findings is that the hot electron temperature scales as

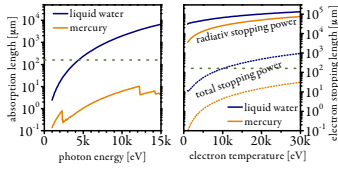


Figure 2.14. Left figure: Photon attenuation length in water and mercury¹⁰⁴. The green line indicates the jet thickness. Right figure: Electron stopping power of water and mercury, normalized to the density of the material and photon energy. The stopping power for radiative energy loss and total energy loss was transformed into a stopping length assuming the continuous slowing down approximation. The spectra were calculated using the ESTAR database¹⁰⁵ which does not consider shell correction. The corrections are necessary if the electron energy comes of the order of the inner shell binding energy.

$$T \sim c \cdot \left(\frac{I}{[10^{16} \text{ W/cm}^2]} \frac{\lambda^2}{[\mu\text{m}^2]} \right)^{2/9 < \alpha < 1}. \quad (2.20)$$

Details of the proposed theories for different intensity ranges, materials and angles of incidence can be found in a number of textbooks, recent articles and references therein (e.g.^{21;24;53;54;58;93;95;106–111}). Fast electrons are stopped in the material and release their energy as bremsstrahlung. Several studies have investigated the conversion efficiency for laser plasma generated fast electrons for different intensities, geometries and target materials^{23;24;93;112;113}. Target ablation at the high laser intensities requires replacement of the target material between shots with precision in the order of the focal dimension of a few micrometers. The ablated material has to be controlled to avoid coverage of optics. Different target/debris handling systems have been developed over the years for flat polished discs^{13;23;24;94;114–120}, wires^{121;122}, tapes^{123;124}, drums^{125;126}, cluster^{127–130}, droplets^{131;132}, pulsed gas nozzles¹³³ and liquid jets^{103;134–141}. Many of the early systems were developed to study laser plasma interactions. Later developments aimed at the application of the generated intense characteristic line emission to study structural changes in ordered systems. It was proposed and shown that a near edge spectrum (see chapter 3) can be extracted using the overlap of characteristic emission lines with specific absorption edges^{142;143}. Several groups showed steady state and time resolved X-ray absorption fine structures using laser plasma sources in the soft X-ray regime (e.g.^{120;126;144;145}). Sources for lab based time-resolved hard X-ray spectroscopy based on these constructions have been build and time resolved measurements been presented^{103;124;141;146–151}. All of those studies use flat or bent analyzer crystals with their low efficiency (see section 4.4.3) to disperse the X-ray probe radiation.

The choice of target material depends on many different aspects: while high-Z materials stop electrons more efficiently (figure 2.14) the reabsorption within the material is also much higher. The conversion efficiency into bremsstrahlung is higher the faster the electrons are. The electron speed depends on the electron density and the maximal achievable power density¹⁵².

The photon flux achieved in the range 5 – 10 keV (presented in papers I and II) is comparable with fluxes achieved from other sources^{103;151;152} and sufficient to limit the detection rate to the detector (see also section 2.5.6 and section 4.5.6). In future iterations X-ray optical elements might be introduced in the system (see section 2.5.7 and 4.4.3). This first version however was designed to run without any optical elements. This work developed the use of single X-ray photon measuring detectors in combination with a plasma source for X-ray absorption spectroscopy, in

particular with the view to enable ultrafast pump-probe and lab-based X-ray absorption studies. Without the possibility to spatially filter characteristic emission lines close to the area of interest (see also comment in section 4.4.3) thick metallic filters would have to be used to suppress the intense emission or the counted background radiation would substantially increase. Partly for this reason, the target material was selected for its lack of observable emission lines.

2.5.5 Sample chamber, water jet target, debris protection and sample jet

Simplicity and long term stability are among the advantages of micro-jet targets. Experiments in this work mostly used a jet apparatus based on a long stainless steel syringe orifice with sharpened edges and an inner diameter of 210 μm a self contracted¹⁵³ jet with 160 μm . The jet apparatus is operated under laminar flow conditions with ≈ 5 m/s. The focal spot is set ≈ 2 mm under the nozzle (see inset figure 2.12). The characteristic scaling length after the Rayleigh-theory predicts the earliest breakup of the jet after:

$$L \approx \cdot \sqrt{\frac{\rho * d^3}{\sigma}}. \quad (2.21)$$

c_{jet} is the jetspeed, ρ the density, d the real jet diameter and σ the surface tension. This length is however only an estimate¹⁵³ and with the carefully designed laminar flow conditions the scaling length does reach several cm. Deionized water is used for the jet and a mesh filter with 60 μm opening prevents clogging of the jet. The stable X-ray production and tests with synchronous stroboscopic illumination of the plasma focus area using the second arm of the laser at different relative arrival times similar to the work from Thoss¹¹³ confirm a stable surface at the interaction region. The fairly large jet diameter enables the control of the angle of incidence on the surface (see figure 2.12 c). If the sample chamber is operated under 1 atmosphere helium the jet is produced using a small centrifugal pump whose already very small pressure fluctuations are further damped by long, elastic tubing.

The rough vacuum in the evacuated setup was chosen to be limited to water vapor pressure to avoid boiling of the jet. A water aspirator pump (buffered over two water filled gas ballast containers) provides a simple and stable pumping system that is not sensitive to the humidity. An external water reservoir is filled with helium under atmospheric pressure and the pressure difference between the chamber and the reservoir drives the water jet.

Several sample chambers were used during the thesis work. The initial work for papers I, II and IV was done in a modular

lead chamber presented in paper I. To be able to automate and feedback the movement of the chamber and its contents with standard motorized linear optical delay stages a new, light weight, modular and compact chamber was developed. This most recent chamber was built from aluminium and designed to provide sufficient absorption to satisfy the safety regulations under stable X-ray emissions. Additional external lead shielding can be added in case of laser instabilities and hazards from high energy electron emissions discussed in paper IV. The chamber has two for antireflection coated 1 inch windows, one large observation window and two beryllium windows mounted on aluminium carriers. All windows are sealed with rubber gaskets and can be exchanged. The holder, wall and lid are separate units designed to be opened and modified.

Figure 2.15. Magnified sample chamber and photograph of the setup. Debris protection and outer chamber walls have been removed. A is the water nozzle producing the water jet. B is an alignment pinhole in the place where the sample jet is placed. C is the entrance window of the Detector. D is the off axis parabolic mirror focusing the laser.

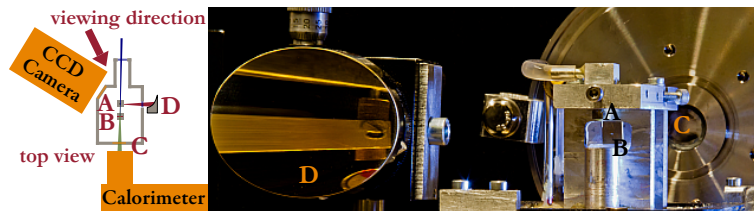


Figure 2.15 presents the sample chamber without the outer walls. The holder for the water jet A and the nozzle for the sample jet are aligned on flat surfaces and can be easily exchanged. The whole chamber is 8×10 cm with an extension for the entrance window of the pump beam. To commence an experiment the system is aligned for maximum X-rays (using the CCD camera, see chapter 4). The detector is aligned on the X-rays that pass through the alignment pinhole. The pump laser is aligned on the pinhole and the transmitted intensity measured. A first indication of the temporal overlap is measured by introducing a scattering element near the nozzle A and measuring the scattered light with a fast photodiode (the pump-beam traverses a fixed distance past the water jet, see also figure 2.19). Improved time-zero alignment might be found by measuring the pump beam scattering from the generated plasma plume (in which the critical density acts like a plasma mirror). The alignment pinhole is then replaced by the nozzle that replaces the sample jet.

During the operation under aspirator vacuum pressure, a small amount of helium can be constantly lead into the chamber and onto windows and other surfaces where condensation might cause problems. A small splatter protection with holes for the two laser beams is placed in the gap between the holder and the catch tube of the water jet to minimize the open area. The constant gas stream purges the chamber effectively from the

water splatter and steam generated by the plasma explosion. Water and sample outlets are tapped with screw threads and can house changeable stainless steel catch tubes. The chamber rests on three custom built adjustable legs with ball heads that each sit under tension in a v-shaped groove providing a stable 6 point kinematic design with very low slip¹⁵⁴⁻¹⁵⁶.

For pump probe measurements the sample is a free flowing jet with ≈ 0.6 m/s, produced by two conically wedged flat stainless steel plates with 6 mm length and adjustable gap beginning from a few micrometers. The pressure difference is generated by a small chemically resistant pumps (e.g. micro gear pump from MZR Inc. or small diaphragm pumps from Xavitech).

Future improvements on the jet system could include separation of the sample environment from the X-ray generation environment using thin membranes or break through nozzles¹⁵⁷. The sample environment could be decoupled from the X-ray chamber with broadband X-ray optics (see section 2.5.7), though this would introduce alignment difficulties, questions of X-ray temporal dispersion in the optics.

2.5.6 X-ray flux considerations

X-ray absorption spectroscopy measures the spectral variation of the absorption cross-section. The important task is to achieve a flux on the sample area that:

has known spectral composition This can be achieved by either using a monochromatic beam and normalizing on the incoming and outgoing intensity, or by using a beam of the full spectral width and analyzing its spectral components with and without the sample.

is as stable as possible For monochromatic beams with large fluctuations an effective normalization is needed which has a signal to noise ratio similar to the actual measurement. If spectral fluctuations do not include sharp features they can be normalized by a system with worse spectral resolution than would be needed to retrieve the spectrum.

is as high as possible to measure with the desired signal to noise and readout capabilities of the detector. Every photon in XAS carries information and the signal to noise statistics is often limited by the number of photons collected. In our single photon counting experiments this rate is limited by the number of microcalorimeter pixels and their individual countrate.

does not damage the sample In most ultra-fast time-resolved experiments the sample is replaced before each X-ray expo-

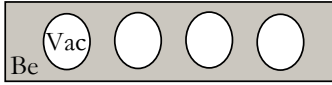


Figure 2.16. Beryllium lenses using the refractive index $n(Z) = 1 - \alpha Z$ typical focus length of several meters

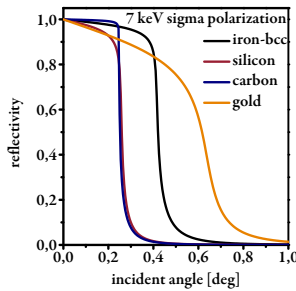


Figure 2.17. Relative reflectivity as function of incident angle measured from grazing incidence. Generated with the database¹⁵⁸

sure. The pump beam often causes as much sample damage as the X-ray probe.

must not produce radiation hazard In large scale facilities radiation safety for users is often excellent. In small experimental table top setups radiation hazards like the described electron beams need to be recognized, monitored and eliminated by the experimentalist.

2.5.7 X-ray optics with potential use in tabletop absorption spectroscopy with direct detection

The index of refraction for X-rays is calculated and experimentally proven to be less than unity in materials¹⁵⁹.

$$n = 1 - \left(\frac{e^2}{mc^2}\right) \frac{N\lambda^2 Z}{2\pi} \quad (2.22)$$

where N is the number of atoms per unit volume and Z the atomic number. This fact enables the interesting construction of beryllium lenses with vacuum/air as the material with higher index of refraction (figure 2.16)¹⁶⁰. The kinematic theory of reflection after Darwin/Prins describes the angular dependence of the total reflection in a Bragg peak with polarization perpendicular to the scattering plane and negligible absorption as:

$$|\theta - \theta_0| < \left(\frac{e^2}{mc^2}\right) \frac{N\lambda^2}{\pi \sin(2\theta)} f. \quad (2.23)$$

Here N is the number of atoms per unit volume and the angle θ_0 is the Bragg angle corrected for refraction derived for small n from

$$\lambda_{vacuo} = \lambda_f \left(1 - \frac{1-n}{\sin^2(\theta_0)}\right)$$

and the false uncorrected Bragg glancing angle for this order

$$\lambda_f = (2d \cdot \sin(\theta_0)).^{161}$$

If we neglect effects of absorption, material density and the dispersion corrections f' and f'' , the width of the total reflection scales as: $f^0 \sim \rho/q$ with the density ρ and momentum transfer Q ^{159;162}.

$$Q = |K_f - K_i| = \frac{4\pi \sin(\theta)}{\lambda}.$$

For heavier and less ordered materials the absorption in top layers can not be neglected and the initially perfect reflected intensity is attenuated faster (figure 2.17).

Regardless of these absorption effects, the very small acceptance angle associated with Bragg diffraction amounts to a very

narrow bandpass behavior when using crystal diffraction as the basis of an energy analyzer. There can be corresponding losses of flux. Reflection under very small angles has a similar angle dependence being in effect zero order diffraction. Nevertheless energy dependence for reflection can effectively cover a larger wavelength range. The emission of a point source like a plasma source is in principle isotropic in the full solid angle 4π (see also paper I), which is a problem when designing or considering X-ray optics.

Using a larger solid angle without smearing the time resolution requires a careful design of the experiment. Optics for broadband reflection suitable for tabletop XAS include:

toroidal mirrors figure 2.18 a) Elliptical design guides the reflected rays with one reflection into a good focal spot. The material is usually as heavy as possible or covered with a high Z material, or can consist of multilayers in which the d-spacing may be tapered^{160;163}.

poly capillary lens figure 2.18 b) Many small capillaries made e.g. from lead glass or silicon guide the beam over several internal total reflections. These optics can have stronger bends than optics based on single reflection and therefore capture a larger solid angle. With each reflection the penetration depth smears the time-resolution and the difference in the pathlength allows only the use of a small outer ring. There are many different designs using single or multiple diameters.^{164;165}

lobster eye lens figure 2.18 c) A multifoil optics with rectangular or axial symmetric cross section. The foils are covered with multilayers or high-Z materials like gold to give better performance at shorter wavelength. The design offer a large solid angle of capture (several 10s of mrad)¹⁶⁶.

bent mirror system figure 2.18 d) Bent gold or multi layer covered systems. Two bent mirrors coated with high Z material or wavelength adjusted multilayers are arranged at 90 degrees and have a two bounce focal path. The perfection of the surface can be made very high. Such Kirkpatrick-Baez systems are among the achromatic standard techniques used at synchrotron sources^{160;167;168}.

With each reflection the temporal broadening can be increased and pathlength differences have to be considered carefully for each design. Bargheer¹⁶⁹ presents some considerations for the use of optics in table top diffraction experiments which are valid for the broadband capable devices. The solid angle for a circular

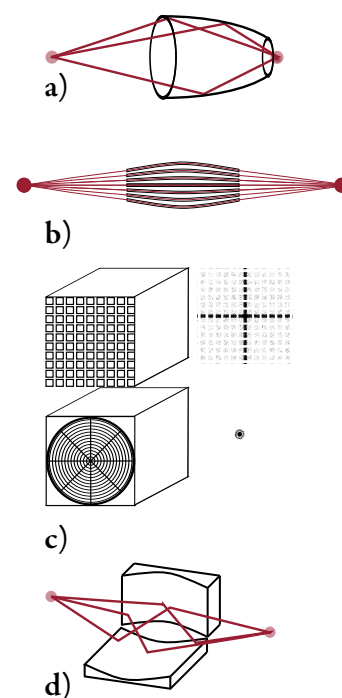


Figure 2.18. a: toroidal shaped single reflective optics, b: poly-capillary lenses, c: lobster eye multifoil optics, d: bend mirror systems

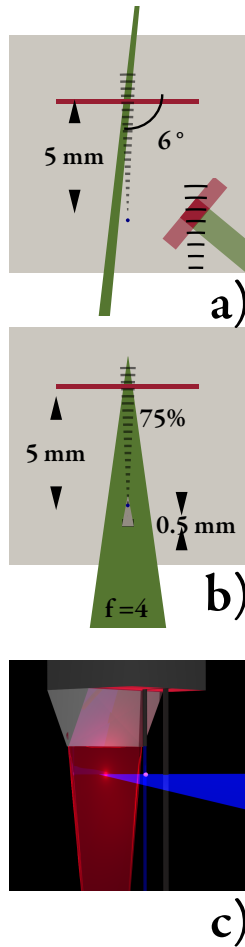


Figure 2.19. *a:* At reduced source-sample distances the temporal smearing is increased due to the different wavefront projection on thick samples. Differences in the speed of light in thick samples can be compensated by wavefront tilting. *b:* a different perpendicular nozzle design with a small beamblock in front of the water jet and strong focusing can simplify the use of small distances. *c:* 3d sketch of the design.

cross-section with the full opening angle ω is

$$\Omega = 4 * \pi \sin^2\left(\frac{\omega}{4}\right) \quad (2.24)$$

In the presented tabletop XAS setup the use of optics was avoided by bringing the sample close the source. This avoids the necessarily careful mechanical alignment, spectral filtering qualities, temporal dispersion considerations and expense of X-ray optics. In the currently implemented prototype the source-sample distance was chosen to be 2 cm = 1.7×10^{-4} sr (assuming a 300 μ m probed spot) for simple access and testing. Without major reconstruction a source sample distance of 0.5 cm = 2.8×10^{-3} sr (for a 300 μ m diameter probed spot) is possible by replacing the current nozzle with the design described in figure 2.19.

In this simple design the path differences for the bent wavefronts is ≈ 15 fs and only the walk off due to dispersion in the sample gives a strong contribution to the time smearing (≈ 1 fs per 1 μ m pumped sample in water). To reduce this walk-off one would either limit the sample thickness or could adjust the angle between X-ray beam and the exciting laser pulse (additionally wavefront adjustment and control might be needed). It should be borne in mind that the X-ray pulse duration is expected to be a few hundred fs with the current implementation of the source (see paper I).

The use of reflecting X-ray optics could increase the total X-ray flux on the sample (at the cost of additional temporal smearing)¹⁶⁹. It would however ease the access for excitation by enlarging the free distance before the sample and it would enable the possibility to separate the sample environment from the X-ray source. In combination with a stronger and especially harder source the detector development would enable us to measure time resolved table top emission spectra. This possibility to spectrally filter the emission would reduce the measurement time and might ease the use of high-Z target elements by suppression of emission lines (see also section 4.4.3 and 3.4).

INTERACTION

In this central chapter the working life of X-ray photons is presented, after their birth in a "hot" source (chapter 2) and before their demise in a "cold" detector (chapter 4). Compared to the source and detector, foreseeable chemical samples are "warm". X-ray absorption spectroscopy is a well established molecular structure approach applicable to disordered samples. Laboratory based ultra-fast stroboscopic pump-probe capability is a particular incentive in this work. To develop a new technique for transmission X-ray absorption spectroscopy at energies up to and exceeding 10 keV was a goal of this work. The physics of this technique is outlined. The "hot" source and "cold" detector were married for the first time in the closing months of this work. A few of its first resulting transmission X-ray absorption fine structure spectra are presented.

3.1 Main interactions

X-rays interact primarily with the electrons in a material. Electrons have a much higher charge-to-mass ratio than atomic nuclei. This makes them much more responsive to the oscillating electric field of photons. In addition, electrons are usually much more numerous than nuclei in materials.

X-rays that interact with matter can be absorbed, or have their energy altered, or their phase shifted. Absorption will be the focus of this chapter. Energy shifts are the symptom of inelastic processes, and include X-ray fluorescence, Compton scattering⁷⁶, and phonon interactions (which require extremely high X-ray energy resolution). Of these, X-ray fluorescence is an important and easily detectable consequence of absorption, requiring its brief discussion in this chapter. Phase shifts are the basis of the X-ray diffraction methods, of which crystallography and holography are just two well-known examples. It is worth mentioning that

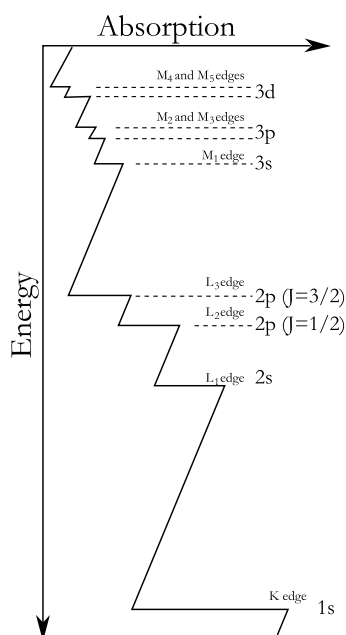


Figure 3.1. Absorption edges for most standard materials are tabulated^{34;104;171}.

Comment to equation 3.1: The integrated transmitted intensity is equivalent to the Beer - Lambert law in the visible range:

$$I(z) = I_0 e^{-\mu(E)z}$$

$$\mu = \ln(I_0/I_T)/z$$

phase shifts and absorption are intimately related. Their common ground has its roots in the Lorentz driven oscillator model that was presented in section 2.3.1, while the quantitative relationship is expressed by the so-called Kramers-Krönig equations⁴.

When absorption of an X-ray photon occurs, an electron is elevated to a higher energy state. The excited electron might still occupy a bound state of the atom or molecule. Alternatively, the electron might have sufficient energy to escape the atom or molecule altogether, and radiate as a photoelectron wave (with an energy-dependent de Broglie wavelength $\lambda = h/p$ ¹⁷⁰, and a symmetry depending on the parent orbital). These two situations correspond to different features in X-ray absorption spectra. In the first case, the available bound states give a spectroscopist's assessment of the atoms and geometry of the molecule. In the second case the free photoelectron wave can serve as a probe of neighboring atoms, by reflecting from and among them in a way that modulates the X-ray absorptivity. Either way, the absorption of X-rays can serve as a probe of the structure of molecules. This structure can be decoded from the X-ray absorbance if one understands the electron's behavior.

3.2 X-ray Absorption processes in spectroscopic methods

X-ray absorption spectroscopy (XAS) probes the absorption probability of photons as a function of their energy. The absorption in an infinitesimal thin sheet of material is given by^{172;173}:

$$-dI_{trans} = I_{trans}(z)\mu dz \quad (3.1)$$

with μ the linear absorption coefficient, I the intensity and z the pathlength in the material. Ignoring resonant absorption energies the absorption cross section for a free atom follows

$$\mu(E) \approx \frac{\rho Z^4}{AE^3} \quad (3.2)$$

with a strong dependency on the atomic number Z and the energy E ; ρ is the density and A the atomic mass⁸⁰. The strong Z dependence gives element specific contrast which can be further enhanced by using differential absorption above and below resonances¹³. The probability for a photon to be absorbed can be theoretically derived from the transition moment between the initial ψ_i and the final states ψ_f and the density of states ρ ^{168;174;175}.

$$\mu \propto \left| \langle \psi_f | H' | \psi_i \rangle \right|^2 \rho(E_f - E_i - \hbar\omega). \quad (3.3)$$

If the energy of the photon is sufficient to excite a filled electronic state into a continuum state the sudden rise in the absorption probability is called absorption edge (see figure 3.1). The excited atom/molecule undergoes different radiating and non radiating relaxation processes which are shown in figure 3.2. The two main deactivation channels are the fluorescence decay and the Auger decay. For hard X-rays (above 2 keV) the fluorescence decay process is more likely¹⁷⁶. During the fluorescence decay an electron at a higher energetic state fills the core hole and a photon of characteristic energy is emitted. The emitted photon energies are element specific and are used in X-ray emission spectroscopy (XES). The energy of the emitted photon can be analyzed for chemical shifts in both the final core hole state and the emitting originating state. The width of the absorption cross section is broadened by the uncertainty principle $\Delta E\tau \geq \hbar$ due to a very short lifetime τ of the core excitation. The lifetime broadening of the K-absorption edge of iron is 1.25 eV and 1.6 eV for the $K\alpha_1$ emission¹⁷⁷. Resonant scattering processes from core states over one or several bound intermediate states can overcome this limitation, but require highly tunable monochromatic excitations¹⁷⁸.

The theory of X-ray absorption^{168;176;179–182} and emission^{178;183–185} spectroscopy is well established and for details the reader is referred to these recent review articles and text books. The photon emission is related to the density of occupied states while absorption spectroscopy probes the density of unoccupied states. Both show strong chemical sensitivity and can be used to identify changes in chemical structure¹⁷⁸. The high quantum efficiency of the developed microcalorimeter detectors offer promising features for both X-ray absorption and emission techniques. Non resonant X-ray emission spectroscopy does not rely on monochromaticity of the exciting radiation and would be easily installed in a plasma source setup. Planned ultrafast facilities like the short pulse facility at MAX IV in Lund expect 1×10^7 photons/pulse at 100 Hz and would benefit from quantum efficient detectors with the features discussed in section 4.5.3. The current prototypical laser plasma arrangement and presented measurements are geared towards X-ray absorption fine structure (XAFS) spectroscopy, which and will be the focus of the following discussion.

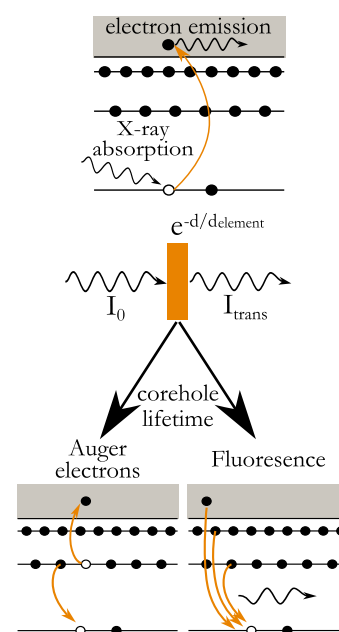


Figure 3.2. Cartoon with the main processes triggered by X-ray absorption.

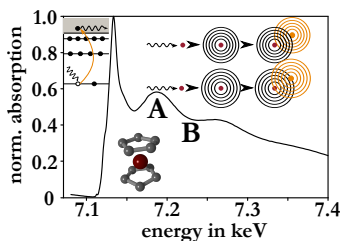


Figure 3.3. X-ray absorption measurement of a complex based on ferrocene. The oscillatory EXAFS patterns from equation 3.4 can be analyzed to retrieve the Fe-C bondlength. EXAFS offers a local molecular structure probe in a potentially complex or disordered molecular environment.

3.3 X-ray Absorption fine structure (XAFS) spectroscopy

It is common to differentiate between the X-ray Absorption near edge structure (XANES) and the extended X-ray absorption fine structure (EXAFS). The difference is how much the description of the transition probability (equation 3.3) can rely on semi classical scattering theory. The emitted electron can be scattered from the neighboring atoms and by a process of interference gives rise to modulations in the absorption pattern. In the EXAFS region approximations to single and multiple scattering path can be made and the absorption coefficient $\mu(E)$ can be expressed as $\mu(E) = \mu_0(E)(1 + \chi(E))$. The correction factor $\chi(E)$ is called EXAFS function and can be expressed¹⁶⁸:

$$\chi(k) = - \sum_j \underbrace{\frac{N_j}{kR_j^2}}_A \underbrace{|f_j(k)|}_{B} \underbrace{e^{-R_j/\lambda_e}}_C \underbrace{e^{-2k^2\sigma_j^2}}_D \cdot \underbrace{\sin(2kR_j + 2\delta_1 + \arg(f_j(k)))}_{E, F, G} \quad (3.4)$$

$$\text{with } k = \sqrt{2m(E - E_0)/\hbar^2}. \quad (3.5)$$

The sum goes over all possible scattering paths j with N_j multiplicity and the electron wave vector k . The prefactor A contains the scaling factor due to the expanding spherical surface at distance R_j of the scatterer and the return path. Terms B and G are the amplitude and phase shift from the atomic scattering factor $f_j(k)$. The variable λ_e in term C is the mean free electron path, and term D is a Debye-Waller factor that describes the average displacement of the scatterers. Term E originates from the wave nature of the emitted electron and can be understood as interference between the arriving and returning wave packet. It gives rise to the oscillatory part in figure 3.3 and F is a phase shift arising from the delocalized nature of the orbital of the emitting atom. For experiments in the EXAFS region the edge jump is normalized, the background subtracted and the modulations of $\chi(k)$ are analyzed. The main information of the EXAFS region is the extraction of interatomic distances. The number and type of ligand atom can be determined, and with improving data quality, multiple scattering paths and can be refined that reveal local structure. Low lying electronic states, the valence of the atom and multiple scattering events contribute to the signal in the XANES region. The analysis often requires complex model calculation and a variety of codes are available to perform such calculation. FEFF, FDMNES, GNXAS, EXCURV and MXAN are some of these codes which are implemented in a number of software packages with fitting routines like IFEFFIT, EXAFSPAK or

Viper^{168;180}. A qualitative approach to XANES involving comparison to reference spectra, can often satisfactory answer the basic chemical questions. One interesting example for this method is the following measurement.

3.3.1 Evolution of Ru-Pt and Ru-Pd catalysts upon optical excitation

In the context of photocatalytic splitting of water it was shown that the dinuclear ruthenium-palladium complex $[(tbbpy)_2Ru(tpphz)Pd(Cl)_2]^{2+}$ (RutpphzPd) with $tbbpy = 4,4'$ -di-tert.-butyl-2,2'-bipyridine and $tpphz = \text{tetrapyrido}[3,2-a:2'3'-c:3'',2''-h:2''',3''-j]\text{phenazine}$ forms hydrogen in the presence of an electron donor and is able to hydrogenate alkynes (see figure 3.4)¹⁸⁶. Hammarström¹⁸⁷ suggested that a similar ruthenium-palladium complex is destroyed during the reaction cycle and that the colloidal particles that result function as reaction centers for further hydrogen production. Sakai¹⁸⁸ showed that the related complex with platinum is stable during hydrogen formation. A manuscript under preparation¹⁸⁹ will present more experimental and theoretical details of the photophysical and poisoning processes.

The optical spectra show a significant absorption of the (RutpphzPd)^{186;190} between 350 nm and 400 nm which is lacking in the (RutpphzPt). The absorption in this area is dominated by $n-\pi^*$ and $\pi-\pi^*$ transitions which are centered on the (tpphz) ligand and might point to a coupling of electronic states of Pt to the ligand. Any photocatalysis in both RutpphzPd and RutpphzPt follows electron transfer from the light-absorbing Ru-center of the complex to the catalytically active metal species.

This experiment was performed at the XAS beamline at the ANKA Synchrotron Radiation facility. Both catalysts were dissolved in a mixture of acetonitrile, water and triethylamine and were irradiated for different times. Comparison of the absorption spectra with reference spectra in figure 3.5 suggests that RutpphzPd decomposes to colloidal metal upon irradiation like the similar complex. While RutpphzPt is not significantly changed upon irradiation. This suggest a different reaction mechanism for the hydrogen evolution in the two complexes. Monitoring the electron transfer during the metal to ligand charge transfer might illuminate this process. The characteristic timescales for the three stage excitation decay in RutpphzPd are 0.8 ps, 5 ps and 310 ps¹⁹⁰. The ruthenium L edges, the palladium L edges and the platinum M edges are reachable with the energies present in the plasma source and their spectrum could be accumulated simultaneously for each molecule. The field of biomimetic hydrogen producing compounds is of great scientific interest and some recent reviews can be found in these references^{191;192}.

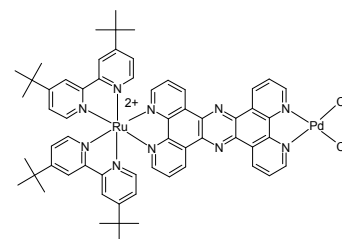


Figure 3.4. Chemical structure of: $[(tbbpy)_2Ru(tpphz)Pd(Cl)_2](PF_6)_2$. The structure of $RutpphzPt$ is similar.

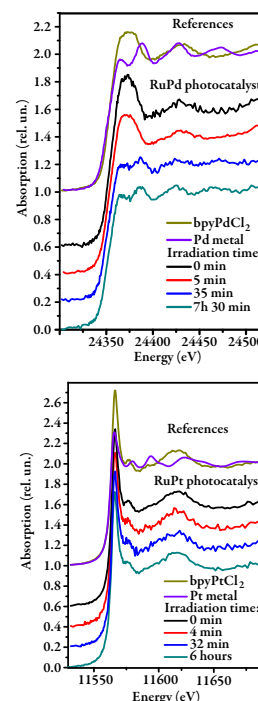


Figure 3.5. NEXAFS of $RutpphzPd$ and $RutpphzPt$ for different optical irradiation periods. Each compared to reference compounds. The $RutpphzPd$ complex shows decomposition and formation of metal like features.

3.4 Ultra fast experiments, filters and examples

In recent years a rapidly increasing number of ultrafast X-ray absorption experiments with sub picosecond time-resolution have been performed at the facilities discussed in the previous chapter. A number of reviews have been published describing their similarities and differences^{8;9;59;193;194}. This section will discuss the choice of filters for a laser plasma source and the performance of the system in relation to them. The transmitted X-ray intensity is the product of absorption in the solvent A_{solv} , sample A_{sample} , and filters A_{filt} , each with its own crosssection $\sigma(k)$ concentration n_i and thickness d . The integrated absorption for each is then according to equation 3.1 $A_i(E) = \exp(-n_i\sigma_i(E)d)$. The information we try to extract is the difference $\Delta\sigma(E)$ of the absorption crosssection in the sample of excited and ground state molecules. The signal scales with the excited fraction f , the concentration n and the sample thickness d .

Broadband transmission experiments based on direct detecting single photon measuring exploits the natural beam divergence to spatially separate X-ray photons in a given shot, which have different energies. The total number of photons that have to be collected depends on the exclusion from the detector of photons whose energies lies outside the spectral range of interest. This energy range might cover several absorption edges simultaneous (see section 3.3.1). The shot noise in single photon counting is Poisson distributed with width $\sqrt{N_s + N_b}$, with N_s being the signal and N_b the background. The square of the signal to noise ratio is also called number of effective counts:

$$N_{eff} = \frac{N_s}{1 + \frac{N_b}{N_s}} \quad (3.6)$$

The optimal filter solution would be a neutral bandpass filter limiting the transmitted photons to the area of interest. In principle, reflective grating like structures could function like this (see section 4.4.3). In the current experiment available transmission filters were used to reduce the number of photons outside the spectral region of interest. For the high energy range a thin material with a suitable absorption edge and a thick low Z filter using the E^{-3} dependence of the absorption (equation 3.2) for the energy range below the absorption edge.

Two or more low energy photons whose summed intensity results in the area of interest contribute to the background signal. The probability for two simultaneous events within the same laser pulse is reduced by suppressing low energy photons as aggressive as possible and sparse the distribution over a higher repetition rate to avoid this pileup. Indeed all photons outside the range of interest simply reduce the maximum attainable

count rate for useful photons. Bunker¹⁶⁸ derives a formula for the selection of the optimal filter thickness that allows tabulated values to be used for the optimization. He defines a filter quality $Q = \mu_{sample} / \mu_{back}$ where μ_i is the linear absorption coefficient in the sample or background energy area. A similar approach with a small difference can be taken here. In his formula the fluorescence of the filters is considered a negative effect. For the microcalorimeter it is indeed very useful for energy calibrating of the detector during operation and the placement of the filters can be used to enhance this aspect. A wider selection of filters is therefore also preferable over a single element filter. A computer routine based on the emission characteristic of the source, the rate at which photons can be accepted (see section 4.5.10), the filter materials tabulated data^{104;171} and the stopping function of the detector can be used to optimize the filter selection and positioning. Crosstalk between pixels at higher count rates and enhancing the prominence of certain features for detector corrections (see section 4.5.13) have to be considered.

The present state of the system and the path for future development can be best illustrated by an example. This example calculates the measurement times for the two spin states of iron-tris(bipyridine)Cl₂ dissolved in water using tabulated values¹⁰⁴ and loosely following the calculations of Gawelda¹⁹⁵. From the total absorption in the aqueous complex at 7.2 keV, every 545th X-ray photon in a 1 mM solution and every 23rd X-ray photon in a 25 mM solution is absorbed by the iron atom. Assuming a 300 μm thick sample jet, the total absorption I/I_0 is ≈ 0.36 for both solutions. The fine structure modulation χ is ≈ 0.55 and the maximum change in X-ray absorbance at full excitation $\Delta\chi$ is ≈ 0.12 normalized to the edge jump¹⁹⁵. Using 1 mJ/pulse of 800 nm excitation in BBO $\approx 200 \mu\text{J}$ of 400 nm can be generated for the excitation of the sample. Focused on 300 μm the fluence is 0.28 J cm^{-2} . With 3.1 eV per photon $\approx 6 \times 10^{14}$ photons are available for the excitation of $\approx 1 \times 10^{13}$ molecules in a solution with 1 mM concentration and 3×10^{14} molecules in a solution with 25 mM concentration. Using the optical cross sections given by Gawelda¹⁹⁵ $\approx 50\%$ of the molecules would be excited in 1 mM and 22% of the molecules in 25 mM. The maximum signal is therefore 2.6% of the edge jump and the background absorption 545:1 in the 1 mM solution and 23:1 in the 25 mM solution. N_{eff} of equation 3.6 is therefore 4.7×10^{-5} and 1.1×10^{-3} . The minimum number of measured photons necessary to reach $N/N_{eff}=1$ is 4.5×10^8 photons/bin and 8×10^5 photons/bin respectively.

The microcalorimeter offers at the moment $\approx 3 \text{ eV}$ energy resolution. Assuming a mild over sampling with 1 eV bin sizes in a 1 keV wide range, a total of 1000 bins would have to be filled. By using simple absorption filters 1/5 of the recorded

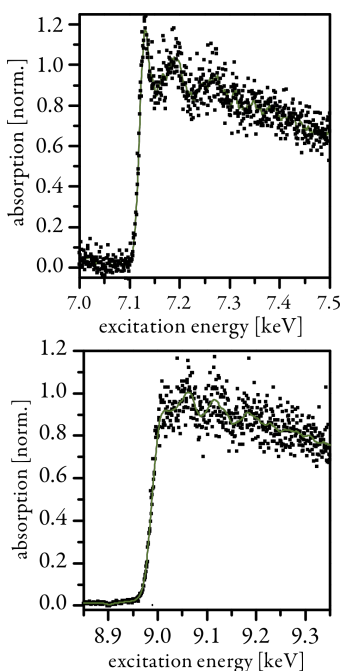


Figure 3.6. Transmission absorption fine structure spectrum of ferrocene. The transmission data was binned to 0.5 eV bins and a 20 points floating average added to guide the eye. As background for the normalization on the edge jump the smooth free atom fit discussed in the text and paper V was used. Both, the iron K-edge of the ferrocene sample (right frame) and the copper K-edge of the filter material show fine structure modulations and suggest the possibility for simultaneous observation of multiple absorbers in a wide range.

photons lay within the 1 keV area of interest. This rough estimate suggests that for each of the 5000 bins 0.45×10^9 photons would have to be collected and with the consideration from above a total of 2×10^{12} photons for a 1 mM solution and 4×10^9 photons for 25 mM to reach a signal to noise of one. A more aggressive clipping of the spectrum would be the most immediate practical approach to enhancing the experiment but could not improve matters by more than a factor of 5.

The following numbers are explained in chapter 4 but they offer a perspective on further short term developments. The detector has a optimum countrate of ~ 1 kHz at the moment. When the array is fully built it will offer ~ 4 kHz with the same record length (shaping time, time needed to measure one photons with the optimum energy resolution). A new room temperature component in the system that is currently tested at NIST and improvements of the temperature modeling in the pixel could allow for higher fluxes in each pixel that would improve the countrate by a factor of 2-4 without changing the detector setup. However, the detector development is a rapidly developing field as will be discussed in chapter 4 (see especially figure 4.11) and the straight forward scalability of this approach suggest interesting future possibilities beyond the capabilities of this prototype. Instabilities in the laser system together with the expected record times for this prototype prevented us from recording pump-probe spectra at this stage of development. But the following section shows some promising first results, that are the basis for paper V, which is still in preparation.

3.5 First results

The combination of source and detector has to date recorded a number of absorption spectra in transmission mode. The very first spectrum was of ferrocene powder and will be briefly presented here. Several other spectra including a spectrum of a free running jet with a 300 mmol iron-tris(bipyridine) Cl_2 solution in water and cobalt compounds were recorded. The ferrocene dataset with a total of $\approx 15 \times 10^6$ recorded events is the smallest of these data sets and was used to develop a semi automated code to analyze the recorded data. It was the "first light" for this source-detector combination. The steps necessary to extract the correct energy of every recorded pulse are discussed in section 4.5.13. The automated code and data extraction is still work in progress but is essential for analyzing large data sets.

This steady state experiment used a thin layer of powdered ferrocene between two layers of "Kapton" foil. The materials in the ~ 30 cm between the source and the detector array consisted of powdered ferrocene with approximately one absorption

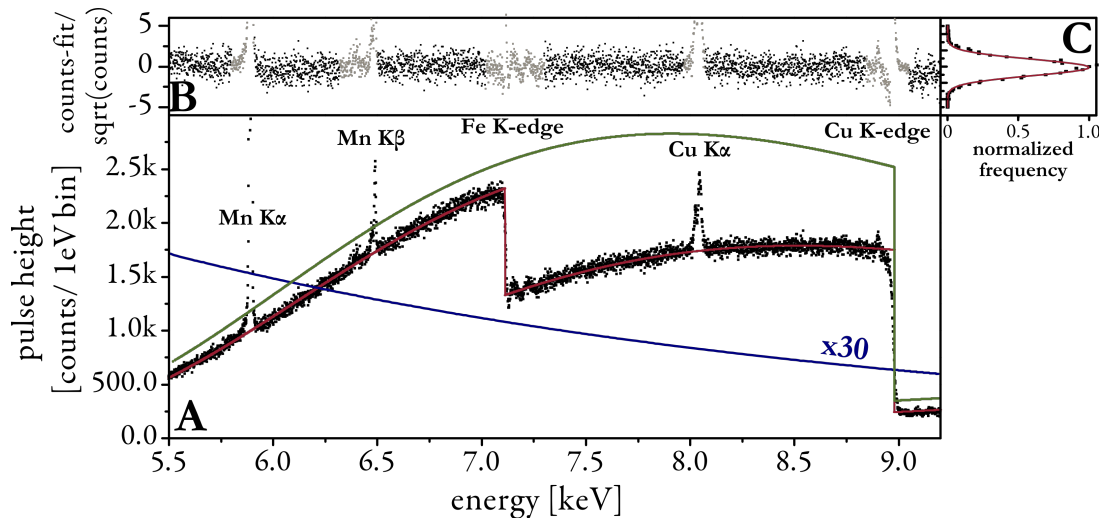


Figure 3.7. A) Laser plasma absorption spectrum in transmission mode of ferrocene. Including emission lines and absorption edges of metal filters and calibration sources (see text), B) baseline fit based on emitted spectrum and reference data of all involved materials. Areas of emission lines and fine structure modulation were excluded (grey). C) A histogram normalized to the poisson error of the total number of counts. A Gaussian curve with $\sigma=1$ is superimposed. The red line is a fit based on free atom reference data on the baseline of the spectrum. The green line is the same fit without the ferrocene absorption and is used as I_0 in the analysis. The blue line is the fitted emission of the plasma source. (see text)

length thickness, 50 μm "Kapton", 136 μm beryllium, $\sim 36 \mu\text{m}$ aluminium, $\sim 20 \text{ cm}$ air and $\sim 6 \mu\text{m}$ copper. The filters and the sample were placed approximately half way between source and detector. The spectrum was accumulated using the 22 pixels available at the time, and with an approximate total countrate of 330 Hz. More experimental details can be found in paper V.

The recorded absorption spectrum is shown in figure 3.7 A. The absorption coefficients for the transmitted materials were retrieved from available sources¹⁰⁴. The data set was fitted with these coefficients (assuming atoms) and under the assumptions that the source emission that can be modeled with a single electron temperature following an exponential emission characteristics (see paper I). The only variables in this fit were the total flux of the source and its effective temperature (blue line), the thickness of the transmitted filter materials, the thickness of the bismuth absorber and the ferrocene thickness. The residuals are plotted in figure 3.7 B. The grey areas were excluded from the fit due to sharp and known features in, or superimposed on, the absorption spectrum. The optimized fit free atom (red curve) shows excellent agreement between the measured spectrum the one one expected from the reference data. The histogram of the residuals

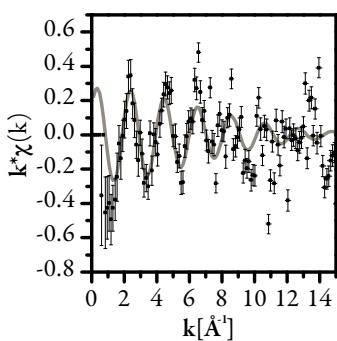


Figure 3.8. *Extracted fine structure modulation from the iron K-edge presented in figure 3.6. The data was binned in quadratically scaled energy bins and the free atom fit (see text) was chosen as background function. Without further data treatment a single path length EXAFS pattern after equation 3.4 was fitted on the data.¹⁹⁸*

was normalized by the expected Poisson error for the number of recorded events. Figure 3.7 C shows this normalized histogram overlaid with a Gaussian distribution function with $\sigma=1$. Their very close agreement indicates that shot noise is the dominant noise contribution in this measurement. From this measurement the region of the iron and the copper K-edge are presented in figure 3.6. The fine structure modulations are apparent. The two edges and their XAFS features visible in figure 3.6 in fact represent well known standards^{168;196;197} and could have been used to extract structural information. Figure 3.8 shows the extraction of the $\chi(k)$ function from this dataset. From the modulation it is possible to determine the Fe-C bondlength (see equation 3.4). As new and better data is obtained from more interesting compounds, and in pump-probe experiments, the measurement technique developed in this thesis is likely to become a powerful tool in chemistry.

X-RAY DETECTION

In this chapter the physics behind X-ray detection will be introduced with the focus on energy resolving detectors in the first part. The second part presents and discusses the detection schemes developed for lab-based direct detection X-ray absorption spectroscopy.

4.1 Introduction

The main difference between detectors built for photons in the visible range and the hard X-ray range is the energy carried by a single photon and combined with this the cross section for interactions. Especially in time resolved measurements the number of available photons is also rather small, so that every measured photon has a relatively large statistical significance. A large variety of interactions can be used to detect hard X-rays. Beside the possibility to disperse the energy of photons spatially before or after the interaction, some material excitations have suitable symptoms to serve as the basis of X-ray detection. This is because X-ray photon energies are much larger than most familiar electronic, translational and rotational transition energies in chemistry. Thus, in the course of thermalization by a cascade of different pathways, many different material and electronic excitations, with various longevity, can be produced by a single X-ray photon. The precision that can be obtained depends on the elimination of mechanistic channels that lead to energy trapping in high energy metastable states (which are the basis of many conventional X-ray detectors). Equally important, the precision depends on the energy of the final excitations being as small as possible. Together, these two considerations motivate ultracryogenic micro-calorimeter arrays.

4.2 Overview of X-ray detection schemes

Fluorescent screens and photographic film were the first detectors used by Becquerel and Röntgen. In these, and the much later image plate technology, the X-ray photon energy either drives a chemical reaction or leads to emission of an optical photon during the decay. These are still popular choices for large area detectors^{199–202}. However they use only a very small fraction of the photon energy (3 – 10 %) and their intrinsic energy resolution is poor compared to other techniques discussed below. Semiconductor, photocathode or gas based detectors are also based on the ionizing abilities of hard X-rays. Photons generate a charge cloud that is electrically read with or without prior amplification. Applied strong electric fields can transfer enough energy to the generated electrons that an avalanche kind of amplification can occur within the detection volume e.g. in Geiger tubes and spark chambers. A controlled electron multiplication after the same mechanism occurs in photomultiplier tubes and multichannel plates, avalanche photodiodes and electron multiplying charge coupled devices. The charge cloud and ionized molecules can act as condensation points in supersaturated environments like cloud chambers. Some techniques measure directly the energy of a generated photoelectron with different techniques like time of flight for soft X-rays, or by using the Cherenkov effect in the range of several MeV. X-ray streak cameras decode the time structure of the arriving photons into a spatial coordinate. The generated electron cloud is then manipulated with a changing strong electric field.

The very stable flux generated during most steady state experiments allows the use of integrating detectors in monochromatic experiments. The low repetition rates and large fluctuations present in most ultrafast time resolved experiments often require either the resolution of every single experiment (shot) and/or the recording of the whole spectral range simultaneously, depending on how stable the spectral distribution is.

Two different types of detector types which were used in the presented experiments shall be discussed further. The first are semiconductor detectors, whose detection principle is based on the generation of a charge cloud in a zone with no free charge carriers. The second are cryogenic single photon counting detectors (section 4.5). Both can be constructed as arrays that provide a very efficient photon energy to signal conversion at low noise levels, with the convenience of electronic data collection and management. In them, individual pixels can determine single X-ray photons with less or more energy resolving ability. And the array size is scalable.

4.3 Excitation cloud generation and energy resolution limit

As discussed in chapter 3 the main absorption mechanisms for photons between 1 keV and 15 keV is photo ionization. The Compton cross section also becomes important as the energy increases. In silicon it becomes dominant above ≈ 60 keV¹⁷¹, with the changeover moving to higher energies for higher-Z elements. With photoionization being the dominant interaction mechanism, the initial result of both mechanisms is the partial or complete energy transfer from the photon to one electron. This electron can have energy up to the initial X-ray photon energy, and/or leaves a highly excited ion. The ionized atom can generate further charge carriers via Auger or shake up processes if the electron was absorbed in deeper bound levels. The highly energetic electrons distribute their energy in several steps. The initial interactions are collisions with nuclei and (primarily) electrons, during which additional, lower energy electrons and some new, lower energy photons (bremsstrahlung) are generated^{171;203;204} (see also figure 2.14).

In metallic systems the free charge carriers absorb the energy and couple it efficiently to the lattice, which results in a fast thermalization of the excitation. In superconductors the barrier for free charge generation is the Cooper pair binding energy on the order of several meV (see equation 4.10 and 4.5.3). The principle energy breakdown process is similar to semiconducting/insulating materials that have a larger bandgap. The main energy loss mechanism for electrons with energies close to the bandgap is electron - hole generation. For silicon at room temperature this process substantially accounts for photoelectrons with energy greater than the bandgap (≈ 1.2 eV) and up to ≈ 10 eV²⁰⁵⁻²⁰⁸. Electrons with less energy excite primarily optical and acoustical phonons and in this way couple their energy to the lattice. Especially for superconducting absorbers the coupling processes and energy down conversion is under active discussion²⁰⁹⁻²¹³.

Non-equilibrium detectors (e.g. charge coupled devices, photodiodes or superconducting tunnel junctions) rely on generated excitations whose number fluctuate for a fixed X-ray photon energy²¹⁴. Phonons can also be generated during each ionization step in the cascade described above. At the end of the cascade the electrons have a thermally distributed energy below the X-ray photon energy and have a energy above the energy gap (roughly 1700 ionizations are generated for a single photon with 6 keV in silicon). Van Roosbroeck compared this randomized distribution to a simple model called crazy carpentry²¹⁵. The total number of generated excitations is much smaller than is expected from the excitation energy $N_{excitations} < E_{photon}/E_{Gap}$, which would apply

Numerical example: *Non equilibrium detectors rely on the fact that the thermal excitations are small compared to the signal. The thermal energy is with the Boltzmann constant $k_B T \approx 26 \text{ meV}$ for 300 K. To reach a energy resolution of 2 eV for 6 keV photons the gap energy would have to be $(E_{SI}/E_{gap})^{1/2} \approx 65$ and therefore $E_{gap} \approx 0.3 \text{ meV}$. Assuming the condition $E_{gap} > 10 \cdot k_B T$ the temperature of the device would have to be $T < 3.5 \text{ K}$, at a still significant dark current.*

if jumping the gap was the only channel for the redistribution of the X-ray photons energy.

The minimum energetic fraction needed to generate a single excitation is dependent on:

- the materials gap energy and type of excitation²⁰⁸
- the temperature, since it varies the gap energy and electron-phonon interactions²¹⁶
- the initial photon energy since it plays a role for the initial cross-sections and nonlinear effects due to high electron densities^{216;217}
- the kind of device, since some devices use high electric fields to extract the charge carriers which raises the device dependent possibility of avalanche gain processes.^{217;218}

If one assumes a Poisson distribution of the total number of generated electrons, and tries to measure the energy of a single absorbed photon by counting the N excitations generated for every energetic fraction ϵ , we would expect:

$$\langle \Delta E_{measured} \rangle = \epsilon \sqrt{N} = \sqrt{\epsilon E_{photon}} \quad (4.1)$$

Fano showed, that if the ionization events along the cascade could be treated as independent events, then fluctuation in the total number of charges partially average out. With the so called Fano-factor²¹⁴ $F < 1$ the fluctuations are smaller than a pure Poisson distribution would predict²¹⁹:

$$\langle \Delta E_{measured} \rangle = \sqrt{F \epsilon E_{photon}} \quad (4.2)$$

The Fano-factor and the energy fraction ϵ for the generation of one excitation can be simulated or measured. For a cooled silicon detector and 6 keV photons they are $F \approx 0.1$ and $\epsilon \approx 3.6 \text{ eV/electron}$ ^{208;216;217}. Neglecting other loss or gain processes in the device. The fundamental resolution limit for silicon, which is often called Fano-limit, with these values would be:

$$\langle \Delta E_{measured}^{silicon} \rangle = \sqrt{F \epsilon 6 \text{ keV}} < \sqrt{E_{Gap} 6 \text{ keV}} < \sqrt{\epsilon 6 \text{ keV}} \quad (4.3)$$

and assuming a Gaussian distribution

$$\Delta E_{FWHM} \approx 2.355 \cdot \langle \Delta E_{measured}^{silicon} \rangle \approx 109 \text{ eV and} \\ N_{excitations} \approx 1666 \text{ e-h pairs}$$

From equation 4.2 it is obvious that the energy resolution improves with smaller ϵ .

4.4 Semiconductor detectors

There are a large variety of semiconductors actively used for X-ray detection. The absorption length of silicon (figure 4.1) for photons above 5 keV is larger than the depletion length of most depleted areas in p-n junctions, so many X-ray detectors use scintillator screens to stop the X-rays and convert them to visible wavelength. The conversion and optical capture efficiency are poor and effectively scramble the observable energy of the original X-ray photon. However, the X-ray stopping efficiency of the scintillator can be made almost 100%. Devices with several hundred micrometer thick depleted areas have become available since. These direct detection devices alleviate the need for the separate scintillator (except at high X-ray energies), and the X-ray energy scrambling problem that it causes.

Common to most types of detectors is that the generated electron-hole cloud is separated by an applied or internal electric field and guided into a charge sensitive preamplifier where it is quantitatively amplified and ultimately digitized. In some cases an electric field chosen to transfer sufficient energy to the generated excitations to further ionize and generate an intrinsic gain by an avalanche process. Since this statistical process is often non-linear it amplifies existing noise and degrades the intrinsic energy resolution. It is however preferred for low energetic photons and when the application aims at speed and counting the number of photons but not resolving their energy²²⁰. Devices using this effect are e.g. electron multiplying charge coupled devices (EMCCD)²²¹, or avalanche photodiodes (APD)²²². Drift diodes offer excellent single photon resolution and have been built as multi element devices with resolutions close to the Fano limitation presented above²²³. When operated as drift diodes they can accept only one photon per element and pulse. In a different mode of operation they work as fully depleted charge coupled devices described below. The stopping power of common semiconductor materials requires thick depleted areas from which the charges can be collected. A variety of materials have found use in single pixel detectors^{224;225}. The majority of large scale semiconductor area detectors, however, are based on doped silicon.

4.4.1 Charge coupled devices (CCD)

X-ray energy resolution can be achieved with spatially dispersed Bragg diffraction (see section 4.4.3). The narrow band pass condition of the Bragg reflection however makes inefficient use of broadband radiation and experiments are time consuming. The use of the intrinsic energy resolution in direct detection devices improves the quantum efficiency dramatically. Charge coupled

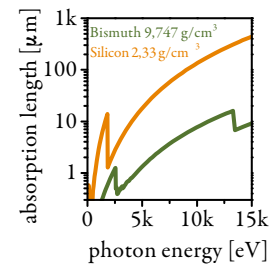


Figure 4.1. X-ray absorption length for silicon and bismuth.¹⁰⁴

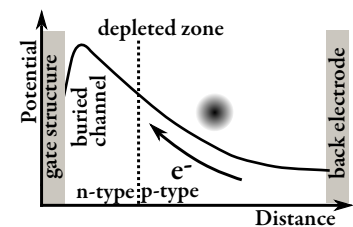


Figure 4.2. Schematic electric potential in the depleted zone of a PN-CCD. With buried transfer channel, symbolized gate structures and transport direction.

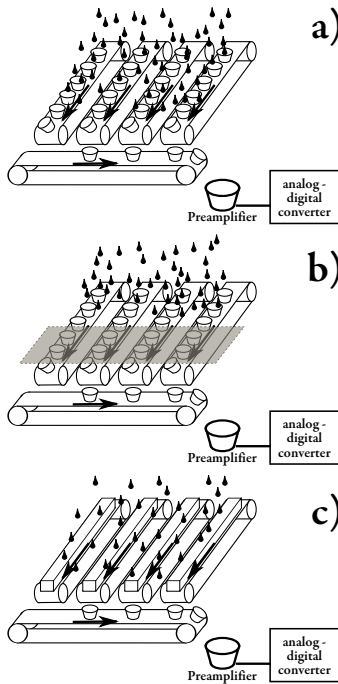


Figure 4.3. Conveyor belt analogy²²⁶ for the different modes of operation. *a:* in the standard operation mode the charges are shifted on row at a time with the vertical shift speed into the transfer channel and read out through a pre-amplified analog-digital converter. *b:* fast kinetic or frame transfer readout mode uses part of the CCD as physical information storage. *c:* fully vertically binned mode, a whole vertical column is coupled as a single pixel.

devices (CCD) have found widespread use in the scientific community and are frequently used for a large number of different purposes. The high demands for low defect densities and challenges concerning scalability and price has led to a silicon dominated technology. To obtain sufficient stopping power in the active area the dopant densities are arranged to extend the device depth that is totally depleted from charge carriers to several tens of microns²²⁷ (indeed scientific fully depleted devices with several hundred micron depletion depth have been produced²²⁸). Excitations generated in this area are separated and the electrons are transferred into a buried transport channel (figure 4.2). The buried channel close to the gate structure is generated by selective doping. It collects the charges and keeps them physically separate from surface imperfections, where recombination and trapping can occur.

The potential in the three or four step gate structure on one surface is sequentially reduced and raised to transport the cloud charge into the next pixel^{219;229}. From the variety of readout modes three are particularly useful in the context of pulsed plasma sources and shall be discussed a little bit further. During a full frame readout the pixels are shifted one row at a time with the vertical shift speed into the horizontal shift register (figure 4.3a). This register is read pixel by pixel with the horizontal clocking frequency through a charge sensitive preamplifier and an analog to digital converter. The typical full frame readout frequencies are on the order of a few Hertz depending on the array size and choice of clocking speed. Higher speeds reduce the separating voltages and lead to additional noise sources and potential loss of electrons due to recharging effects^{219;230}. The fast kinetic (or frame transfer) mode (figure 4.3b) uses a part of the CCD *hidden* behind a sufficiently thick block as physical storage. A reduced number of rows can be shifted very quickly behind a blocking layer, since nothing is read during the transfer time. The stored frames are read afterwards in the normal way. In this mode the camera can be operated at the repetition rate of the laser without the use of a shutter. A full frame is accumulated over several shots. All or part of the array can be hardware binned to columns and read out with kHz repetition rate to give a realtime feedback of moderate to fast repetition rate pulsed sources (figure 4.3c).

In front illuminated CCD the photons have to penetrate the thin gate structures. If the charge cloud is generated close to the gate structure it directly feels the strong confining electric field. Our commercially available CCD has a fully depleted depth of $\approx 40 \mu\text{m}$ ²³¹ (in silicon the absorption length is $\approx 30 \mu\text{m}$ at 6 keV) and can contain a maximum of 2.5×10^5 electrons/pixel²²⁷, which corresponds to ≈ 150 photons of 6 keV. This number is important if the device is operated in the fully vertical binned

mode, or while measuring energetic particles like the electron beams discussed in paper IV. These kind of chips are usually not fully depleted and have areas with no confining field deeper in the structure. Back illuminated, back thinned chips have a weaker confining field close to the back electrode and charges can more easily spread in this region. Special fully depleted chips with low conductance are available but are not usually included in commercial cameras^{219;228;231–234}. Paper II discusses various effects and consequences if the initial charge cloud distribution spreads over the borders of a single pixel or at different depth in the CCD and how such a device can be used to analyze laser plasma sources¹⁵². It was possible to evaluate the charge cloud radius as function of the X-ray photon energy by suitable analysis. At very low exposures which guarantee sparse enough event densities to separate each single absorption event spatially, CCDs have frequently been used as multi element single photon counters^{50;152;235}.

In figure 4.4 the emission of a ^{55}Fe source (see section 4.5.12) was recorded on a 256×1024 pixel, $40 \mu\text{m}$ deep depleted front illuminated CCD²²⁷ cooled to -65°C . 10000 frames with each ≈ 900 absorption events were recorded and analyzed. All pixels below a chosen threshold were set to zero and events spread over more than 2 pixels discarded. Figure 4.4 a shows the pulse height spectrum separated into absorption events contained within a single pixel and spread over two pixels. The deconvolution for single pixel events gave an energy resolution of 150 eV for 2.5 MHz pixel readout. If the readout is slowed down the optimal resolution is 138 eV. From charge clouds spread over two pixels spectral information can still be extracted. They need a separate background treatment (not applied in this figure) and with this correction broadened the observed spectral line by 40 eV. The threshold has to be chosen with care and optimized for every set of shift speed, exposure time, gain settings, chip temperature and total recorded flux. A threshold below the actual noise level rejects a large number of pulses and leads to poor counting statistics (figure 4.4 b). A high threshold neglects the spectral redistribution (figure 4.4 c). High level programming languages like Matlab, Pylab and Labview, which are often used to automate such analysis, are especially efficient and fast if their optimized matrix subroutines are used for such data analysis. In the appendix B a simple matrix algorithm, which was developed to reduce the processing time of such an analysis, is explained.

Figure 4.5 presents a single shot spectrum from a collimated X-ray beam generated by electron oscillations in a laser wakefield accelerator. The experiment was performed at the high power branch of the multi Tera-watt laser of the Lund Laser Centre and is described in references^{50;91}. The CCD was used to optimize and study the X-ray emission in more detail. For this measure-

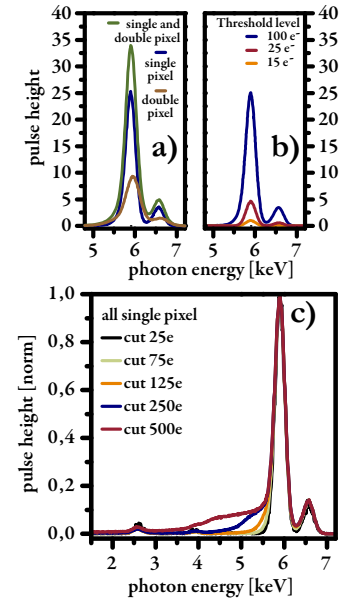


Figure 4.4. Pulse height spectrum of ^{55}Fe line emission. a: after a threshold of 100 electrons was applied, events were sorted into event located in a single pixel and events spread over two pixels b: suppression of events for too low threshold c: at a high threshold the spectral redistribution is not sufficiently suppressed

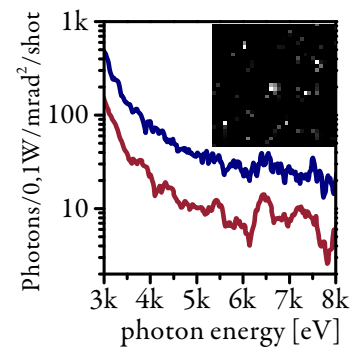


Figure 4.5. Histogram of a single shot from a collimated X-ray beam generated by electron oscillations in a laser wakefield accelerator. The red line shows absorption events spread over a single pixel, the blue line a histogram of all exposed pixels.

ment two 15 μm thick nickel sieves with $5 \times 5 \mu\text{m}$ openings were aligned and placed in front of the camera. The 25 μm pitch of the sieve matches the camera pitch. Even with this reduced intensity a larger than expected fraction of neighboring pixels show excitations above the chosen threshold level. The histogram is corrected for additional absorption in filter materials and the thickness of the active silicon.

In complementary metal oxide semiconductor (CMOS) detectors every pixel drives a small individual processing circuit. A parallel bus system enables the read-out of every single pixel separately^{229;230;236;237}. Hybrid sensors like the commercially available Pilatus²³⁸ are built to offer the possibility to gate pixels to bunches of high repetition rate sources²³⁹. An intrinsic threshold can be set to suppress readout noise. They are used as spatial detectors in scattering experiments or as detectors for Bragg type analyzers (see also section 4.4.3)²⁴⁰. A very interesting recent development in back illuminated back thinned CMOS with depleted zones of several microns, readout noise and very fast readout speeds shall be mentioned^{241;242}. The device has $10.8 \mu\text{m} \times 10.8 \mu\text{m}$ pixels with selectable areas readout and up to 2400 Hz readout for 128×128 pixels. The depletion thickness is 1.5 μm and the expected resolution for 10 ms exposure and at this readout speed is 250 eV.

For many specialized applications hybrid detectors based on CMOS or depleted P-channel field effect transistors (DEPFET) readout and other principles like avalanche photo detection are under development and it will be interesting to follow this rapidly growing field. I had the privilege to work with the XPAD (hybrid CMOS photon counting)²⁴³⁻²⁴⁵ at the linear accelerator in Stanford recording pump-probe liquid scattering. The high repetition rate and numbers of pixels will bring future challenges for on-line data processing. A small selection of other actual projects in this field: MEDIPIX (hybrid CMOS photon counting)²⁴⁶, AGIPD (hybrid CMOS integrating)^{247;248}, ASCI (APD-array)²⁴⁹, ATLAS (hybrid CMOS Photon counting)²⁵⁰. A recent summary was give in the resumé²⁵¹ to the PIXEL conference in 2010.

4.4.2 Application of CCDs in the laser-plasma setup

Figure 4.6 shows several ways that a CCD can be used with a laser plasma source, which have been applied at different times in this work. A more detailed description can be found in paper II. The main adjustment and feedback detector in the laser-plasma setup that was built during this work is an X-ray CCD camera in an Andor-Newton housing. The front illuminated deep depletion 30-11 CCD from the company e2v²²⁷ is mounted on a -60°C cold stage in an argon environment. The camera is operated

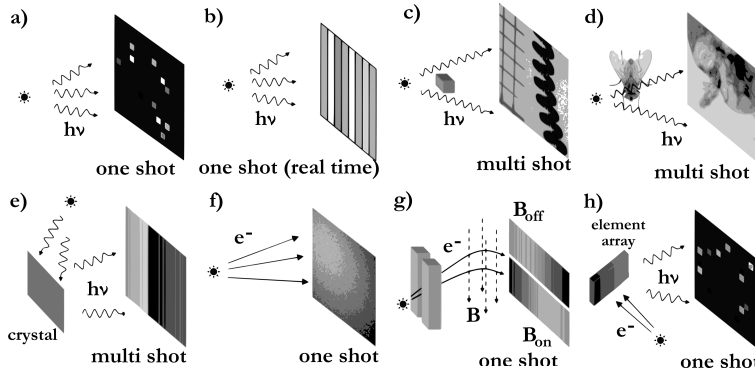


Figure 4.6. Frequent modes of CCD use: a) a parallel array of energy-dispersive point detectors for determination of source spectra; b) aggressive hardware binning allows realtime optimization; c) shadow edge from high contrast objects for source size determination; d) contrast imaging of suitable samples; e) crystal dispersed spectral X-ray measurements; f) direct observation of high energy electron beams; g) particle charge and energy measurements by deflection; h) indirect measurement of particle beams by observation of induced X-ray fluorescence from element arrays.²⁵²

either synchronously to the laser pulses for single shot operation, or in a free running internal triggered mode for multiple shot exposures. Figure 4.7 shows the emission histogram of our plasma source "as measured". The spectral redistribution and features from the protecting gas clearly show the need to apply the corrective calculations discussed above but also the smooth emission of our plasma source in the full spectral range. The black spectrum was generated from 200 single shots with an average of 900 absorbed events and 30 cm of air between camera and source. A detailed analysis and discussion the plasma source and the electron beams measured are presented in the papers I,II and IV.

4.4.3 Bragg optics

In this section we discuss briefly optical elements based on Bragg reflection which are used in the context of ultrafast spectroscopy. Probing the crystalline structures with X-rays has a long history²⁵³ and only a few basic relations shall be mentioned. The momentum \mathbf{Q} transferred from a elastically scattered quantum may be written $\mathbf{Q} = \mathbf{k} - \mathbf{k}'$. If this momentum transfer corresponds to a vector of the reciprocal lattice \mathbf{G} the scattered light will interfere constructively¹⁵⁹. The formulation of the Laue condition $\mathbf{Q} = \mathbf{G}$ is shown in figure 4.9 and is equivalent to the Bragg condition for crystalline layers $n\lambda = 2d \sin(\Theta)$. The accep-

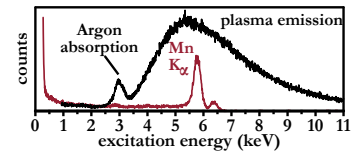


Figure 4.7. Spectra taken of the water jet laser plasma source at 3 mJ pulse energy (black) also ⁵⁵Fe emission spectrum (wine). The smooth plasma spectrum is shaped by the strong absorption from 250 μm Beryllium, 5 mm Argon, 30 cm air, as well as by its absorption in the silicon of the CCD.

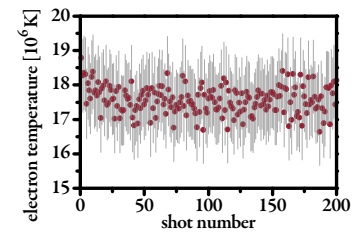


Figure 4.8. The electron temperature was retrieved from the emitted spectrum for 200 consecutive shots. The grey background shows the 95% confidence level of the temperature fit. The shot to shot variation shown here are clearly dominated by the uncertainty within the single shot measurement. The stability of the total flux and accumulated spectra suggest a more stable emission. However, the tracking of the spectrum does reveal alignment problems and the appearance of high energetic electron beams.

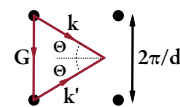


Figure 4.9. Laue condition for constructive interference. The dots represent points in the reciprocal lattice.

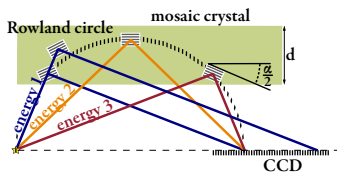


Figure 4.10. A thick polycrystalline layer with small angular distribution of the crystallites reflects.

tance angle for each reflex was stated in section 2.5.7. The very narrow bandpass nature of Bragg reflections makes experiment with flat analyzing crystals inefficient. The use of bent periodic structures increase the volume of the sampled Ewald sphere and is a standard technique used today. The stress introduced in bent single crystals limits the achievable bending radius to the order of meter. Many X-ray plasma sources emit pseudo isotropically in the full 4π solid angle. The solid angle which can be collected from single crystalline devices is therefore very limited if no further optical elements are used^{169;254} (see also section 2.5.6). Optics with polycrystalline or multilayered optics can be deposited on templates suited to the experiment and these collect larger solid angles. A spherically bent Johann type spectrometer uses a larger part of the Ewald sphere and focus photons emitted from a point source onto a point like detector. Each set of bent crystals are scanned in a small range to analyze the energy. High resolution X-ray emission spectrometers are often based on this concept^{178;240;255}. Cylindrical^{256;257}, conical^{258;259} and toroidal^{260–262} bent analyzer crystals focus a broad bandwidth source onto a line focus. They can be used for a wider energy range and have been tested in laser plasma sources. The line focus allows the use of a linear or low dimensional detector array with higher readout speed for recording the whole spectrum at once. A useful overview of the energy resolution and efficiency achievable with Johann type of analyzer optics can be found in references^{160;263}.

Poly-crystalline structures with low mosaicity have been proposed to increase the scattering efficiency²⁵⁷. Photons penetrate the small differently oriented crystallites until the Bragg condition is met or it is finally absorbed (figure 4.10). If the angular distribution (rocking curve, indicated in figure 4.10 by α) is slightly larger than the acceptance angle of each crystallite an increased diffraction can be observed under some condition. This is called mosaic focusing. The crystallite size and material has to be chosen so that the efficiency for reflection is much larger than for absorption in same crystallite and the angular distribution is just wide enough that a larger part of the Rowland circle contributes to the intensity²⁶⁴. The energy resolution is reduced compared to a single crystallite of the same material and thickness since several wavelengths are reflected into the same point in the detection plane. The spread of the energy can be estimated by simple geometric considerations²⁶⁴. Legall reached $E/\Delta E$ of 1800 for the (002) reflection and 2900 for the (004) reflection of a thin film of highly oriented pyrolytic graphite²⁶⁵. The surface and structural quality is essential for a high energy resolution.

Multilayered or grating optical elements could however be used as wide bandpass filters in the laser plasma source^{160;266}. In the soft X-ray region periodic structures for the energy analysis

can be artificially constructed^{126;267–269}. Structured optics for the interatomic wavelengths in the 5 – 10 keV energy range are very challenging for the precision needed in their construction²⁷⁰ at the same time that their cross section for interaction with very small structures becomes low.

4.5 Cryogenic photon detection

Chapter 3 motivated energy resolutions of $\Delta E \leq \sim 5 eV$ for time resolved X-ray absorption studies. This resolution needs to be accomplished for photon energies in the $\sim 5 - 10$ keV range. As presented in the numerical example below figure 4.15, cryogenic detectors with resolutions meeting and exceeding these criteria are becoming available. A core part of this thesis work was the development of a microcalorimeter detector in collaboration with the Quantum Device group at the National Institute of Standard and Technology in Boulder Colorado (USA). It was based on a design of Ullom²⁷¹, for use in an electronically noisy lab environment. Personal contributions included discussions and planning of the detector design, coordination of the construction, building parts of the detector and peripheral components, system assembly in Boulder and Lund, testing and installation of the electronics in Lund and development of the calibration, readout and measurement procedures in cooperation with the group in Boulder. In addition contributions were made to the development of the pulse analysis, supervision and guidance of a thesis study to develop a parallelized pulse analysis and development of major parts of the controlling software and routines in Lund.

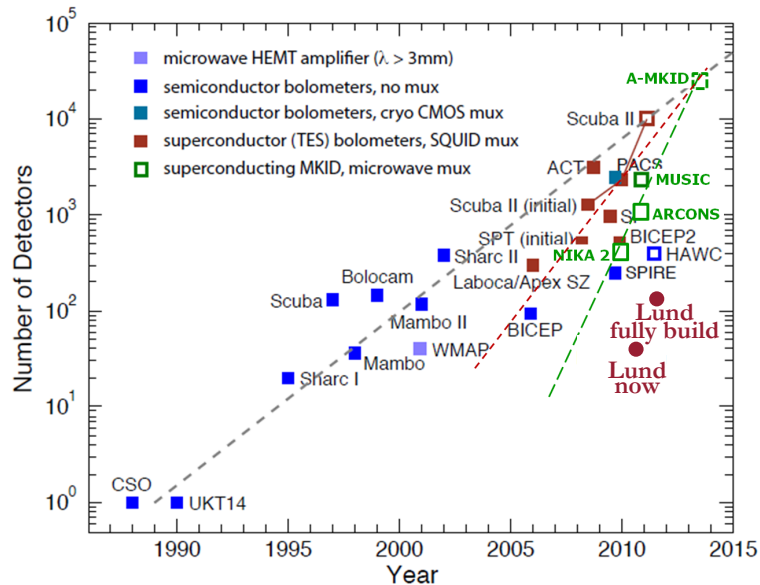
In this section the physics of cryogenic detectors are introduced. The system construction is presented and the features and challenges of these detectors are discussed. The section closes with a description of the analysis and corrections of the recorded data that was necessary to extract the spectra presented in paper V.

Several other types of cryogenic detectors using the thermal energy of the particle shower or charge cloud generated by the high energy photon will be mentioned in the next sections. The focus will be on the calorimetric photon detection. A short introduction to the physics of superconductivity and its role for this detector will also be given. As with the single particle CCD detectors described earlier the essential performance criteria are:

spectrum accumulation time For detectors based on pixels, the relevant attributes are how many pixels they have, how fast is each and whether they are read synchronously or each individually. Also, how good is the multi event suppression and how critical is this. Spectral filtering at the experiment level has of course a positive influence. One important

factor here is the dead time. Detector dead time may come after each event or only after events of a certain kind (see section 4.5.6). At the time of writing the maximum count rate in our detector array reaches ≈ 1000 counts/s. With successive upgrades planned and with ongoing developments, this will increase dramatically. During the "Low temperature detector conference" 2011 the numbers of pixels per device was presented to follow a "Moore's law"²⁷² (see figure 4.11). Devices with capabilities above 10^5 photons/second at slightly lower energy resolution at 6 keV are being developed²⁷³. As a comparison, the single channel readout of commercial scientific charge coupled devices with deep depleted chips offer up to $\approx 5 \times 10^6$ pixel/sec. In either case, data processing may become the eventual bottleneck if every pixel is analyzed.

Figure 4.11. Development of the number of detectors as function of time. The abbreviations in the plot are instrument names. HEMT - High electron mobility transistor, MKID - multiple kinetic inductance detector, mux - multiplexing, SQUID superconducting quantum interference device, TES - transition edge sensor.²⁷⁴



energy resolution Until the shaping time (build-up and decay of a signal) becomes less than the laser repetition interval, there is a trade off for the data acquisition speed. Longer readout per pixel increases the energy resolution performance but reduces the maximum readout speed²⁷⁵. The achievable energy resolution is often not only determined by the machine resolution itself but also by the computation afterwards. The estimated (see section 3.4) 2×10^{12} recorded events for realistic samples have to be corrected for additional fluctuations in the measurement conditions introduced in the detectors. Often spectra are combined

from many different detectors with different calibrations. Optimizing the automation and improving the computational data treatment was one major improvement achieved towards the end of this project.

flux and fill factor, partial registry Since single photon counting can only process a certain rate of counts the total source flux and detector fill factor are only of importance for later improvements involving increasingly accurate measurements. For the transmission based experiments pioneered in this work, more flux from a source only means a larger fraction of X-ray photons would be "wasted", since the bottleneck for the data collection is the detector. Finding more effective experiment-level approaches to X-ray filtering can very usefully reduce the number of photons not contributing to the spectrum. The demands on detectors built for the International X-ray Observatory²⁷⁶ aim to reach fill factors close to 100% with mushroom shaped absorbers for a similar energy range²⁷⁷. The fill factor during the experiment presented in paper V was 2%. As more pixels are commissioned the fill factor of the existing detector is increasing. Once this array is fully constructed it will offer a 20% fill factor. Considering also the $\approx 50\%$ quantum efficiency of the absorber at 6 keV, this might be considered as $\approx 10\%$ detection quantum efficiency for the solid angle subtended by the array.

4.5.1 Low temperature effects

Electrons in a metal scatter inelastically with each other, lattice imperfections, impurities and phonons. If the electrons are accelerated by a potential difference the originally random energy transfer will be changed into an energy flow from the electrons to the lattice. The scattering of the electrons is the origin of the resistivity. Electrons are Fermions and follow the Pauli exclusion principle, meaning that they will not occupy the same state. A consequence is that the number of particles \bar{n}_i in a single-particle state of energy ϵ_i is (with k_B the Boltzmann constant and T the temperature):

$$\bar{n}_i = \frac{1}{e^{(\epsilon_i - \epsilon_f)/k_B T} + 1} \quad (4.4)$$

The fraction of thermally excited electrons above the Fermi level ϵ_f is of the order of $k_B T / \epsilon_f$ and is the fraction of electrons contributing to heat and thermal conductivity. The electrical conductivity σ is linked to the thermal conductivity κ by the "Wiedemann-Franz Law":²⁷⁸

$$\kappa = (\pi^2 T / 3e^2) \sigma \quad (4.5)$$

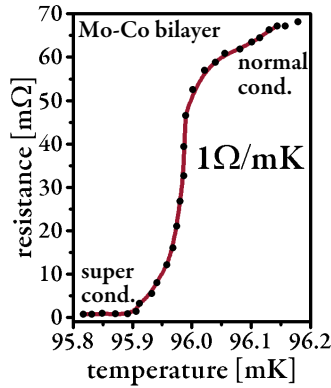


Figure 4.12. Electrical resistance as function of temperature. The very steep transition is the basis of the transition edge sensor as temperature sensor. The natural transition temperature T_c can be chosen to be close to the desired working point.

In pure metals the heat conduction is mainly carried by electrons since the electronic speed on the Fermi surface v_F is much larger than the speed of phonons (speed of sound u). An estimate²⁷⁸ for the speed ratio of v_F to u can be found with the Fermi energy ϵ_F , the effective electron mass m^* , the lattice constant d and the atom mass M :

$$\begin{aligned}\epsilon_F &\sim v_F p_F \sim \hbar^2 / m^* d^2 \\ u &\sim v_F \sqrt{m^* / M}.\end{aligned}\quad (4.6)$$

The effective mass m^* is the mass of an electron close to the band gap and can be derived from $1/m^* = \hbar^{-2}(d^2 E/dk^2)\epsilon_F$. While this is equivalent to the electron mass for a free atom it can vary strongly in crystals depending on the electric field. For metals one can assume the fraction of excited electrons to be $k_B T / \epsilon_F$. Let N be the total number of electrons with the approximate energy $k_B T$. The total (thermally) excited energy is then:

$$U_{el} = N \cdot (k_B T / \epsilon_F) k_B T \quad (4.7)$$

the heat conductivity dU/dT carried by the electrons is then,

$$c_{el} = (2k_B^2 / \epsilon_F) \cdot NT \quad (4.8)$$

With decreasing temperature the number of free electrons reduces and less phonon modes are excited. The remaining electrical resistance called rest resistance is dominated by lattice and impurity scattering. The total resistivity ρ is simply additive and could be written $\rho(T) = \rho_0 + \rho_{electron\ phonon}(T)$. The second temperature dependent part scales roughly linearly with temperature at room temperature and $\rho(T) \sim T^5$ for $T \ll \Theta_{Debye}$ (Bloch law). $\Theta_{debye} \sim \epsilon_F \sqrt{m^* / M}$ is the Debye temperature at which all possible phonon frequencies are occupied. The energy dissipation is a random process and the fluctuation dissipation theorem leads to a fundamental relationship between electrical noise and electrical resistance. The mean square of voltage fluctuation $\overline{V^2}$ is called Johnson noise and is related to the Ohmic resistance R , the temperature T and the Boltzmann constant k_B by^{278–281}:

$$\overline{V^2} = 4k_B TR \quad (4.9)$$

and is one of the fundamental noise terms in the detector.

4.5.2 Superconductivity

After the original discovery of superconductivity by Heike Kamerlingh Onnes in 1911²⁸² superconductivity was observed in a wide selection of materials including most metals^{283–287}. In the previous section it was noted that metals at cold temperature have a

finite rest resistance originating in the electron scattering from defects and impurities. Onnes however discovered that once a certain temperature is reached the specific resistivity of the material makes a very fast transition between a finite value and exactly 0Ω . This transition is one of the strongest temperature dependencies known and is used in our setup as a very sensitive temperature sensor. The second basic effect of superconductors is the perfect diamagnetic reaction of a superconductor called the Meissner Ochsensfeld effect²⁸⁸. A superconducting material of type I expels a magnetic field perfectly from its bulk material by inducing a shielding current. The macroscopic Ginzburg-Landau^{289;290} theory of superconductivity^{285;287} describes a penetration length λ_L of a magnetic field into a superconductor, according to $B(x) = B(x=0)\exp(-x/\lambda_L)$. If the magnetic field exceeds a critical field the superconductivity is suppressed. The critical magnetic field has a temperature dependence similar to figure 4.13 following $B(T) = B(T=0)(1 - (T/T_0)^2)$. Superconductors of type II reduce the free energy by allowing flux vortices into the bulk material²⁹¹ in the intermediary Shubnikov phase. The vortices are small normally conducting regions shielded by ring currents in the superconducting area. At high vortex density the superconductivity is suppressed. Since the magnetic field around a current is proportional to the electrical current a critical current j_c can be defined accordingly. This dependence is used in the superconducting transition edge sensor. In this thermometer the critical temperature at zero field and current is above the working point and the critical current is used to suppress the superconductivity and keep the sensor in the transition. In the theory of Bardeen, Cooper and Schrieffer (BCS)²⁹² the reduced lattice vibration and attraction from the nuclei can lead to a net attractive force between two electrons. The two electrons are called a Cooper pair and have either a spin of 0 or +1. They no longer obey the Fermionic law of exclusion, but have all the exactly same bosonic energy state. To break up a Cooper pair at $T=0$ and form a pair of free electrons (now called quasi particles) a minimum energy of

$$\Delta(T=0) = 1,76k_B T_c \quad (4.10)$$

is needed which is called the gap energy. The gap energy for the system shown in figure 4.12 would be $15\mu\text{eV}$ and for pure molybdenum $140\mu\text{eV}$. The gap energy decreases with increasing temperature. At T_c the Cooper pairs break up and form again a Fermi distribution. The assumption of an energy gap has many interesting effects. The energy portion ϵ needed to break up one cooper pair is small. The number of excitations is therefore large and the Fano resolution limit (equation 4.2) small. For pure molybdenum the thermal energy $k_B T$ is at 100 mK very small compared to the gap energy and the fraction of electrons

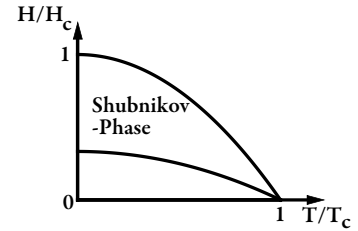


Figure 4.13. The critical magnetic field strength as function of the critical temperature.

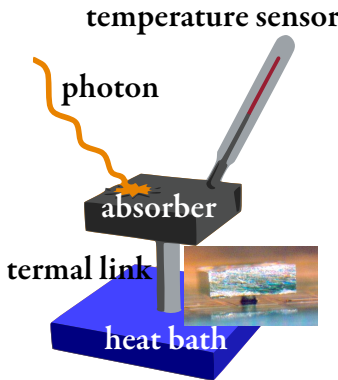


Figure 4.14. Sketch of basic bolometric/calorimetric principle. The small inset shows an actual absorber used in gamma ray spectroscopy (courtesy Dan Schmidt, NIST). A thick tin absorber is glued on a thin film structure similar to Figure 4.16.

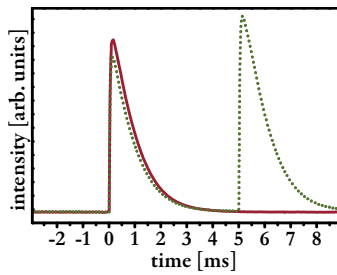


Figure 4.15. Measured pulses from the laser plasma source. A single pulse (red) with several decay times gives a response that returns to the baseline before the next photon arrives. If the density of arriving photons is too high, two photons can be absorbed in the same trigger event and the calculation of the integrated intensity becomes difficult.

Numerical example: For the microcalorimeter array used in the presented experiments (details in the sections below) the estimated $C \approx 1.8$ pJ/K and $G \approx 58$ pW/K. A 6 keV photon would raise the temperature of the absorber by 0.5 mK; the signal fall time τ_0 would be ≈ 0.03 s and with the bath temperature of 85 mK the ultimate energy resolution would be 2.6 eV. The electro thermal feedback generates a faster decay time (see section 4.5.5).

which are excited and could contribute to heat conduction or heat capacity is determined by a Boltzmann distribution with $-\Delta/k_B T \approx -16$ in the exponent. The heat capacity of the material is now dominated by the much smaller phonon heat capacity which in the Debye model at the low temperature limit is:

$$c_{ph} \approx \frac{12\pi^4 k_B}{5} N_{atom} (T/\Theta_{Debye})^3 \quad (4.11)$$

If a normal contacting material comes in contact with a superconducting material some quasi particles diffuse from the normal conductor into the superconductor and lower its critical temperature in the vicinity of the contact area. The thickness of this influenced area depends on the charge diffusion constant of the normal conducting material and the temperature²⁸⁷. Typically the thickness reaches from a few tens of nanometers up to several micrometers. Using thin film technology the critical temperature of the whole film can be adjusted to exploit this proximity effect.

4.5.3 Microcalorimeter array basic principle

In a simple model of a bolometric/calorimetric photon detector the arriving photon of energy E_0 generates a particle shower that is fully thermalized in the absorber with heat capacity C . The temperature changes by $\Delta T = E_0/C$ which is measured by a sensitive thermometer. The absorber is reset with a time constant C/G via a heat bridge with thermal conductivity G to the temperature of the "cold bath" T . A constant photon flux would generate the temperature difference $\Delta T = \text{Input power}/G$. Devices operating in this steady state regime are in general called bolometers and are widely used in applications with high photon fluxes like laser power meters. Calorimeters show a dynamic temperature response to a sudden input of energy. The X-ray photon energy is derived from the integral of the single photon thermal response plotted in red in Figure 4.15. All the following descriptions are based on this principle. Assuming an ideal behavior of the system, the ultimate sensitivity ΔE would be limited by the thermal fluctuations²⁹³:

$$\Delta E_{rms} = \sqrt{kT^2 C}. \quad (4.12)$$

The need for low temperatures and low heat capacity is clear from equation 4.12. Since we are measuring dynamic signals and shall assume a constant signal shape the energy resolution can be somewhat higher than this^{294,295}. Equation 4.12 shows one problem with these devices. To thermalize the particle shower generated by hard X-rays and the successive fast electrons, a high charge density is desirable without the rise in heat capacity shown in equation 4.8. Many absorbers are therefore chosen to be either superconducting or "poor" metals.

4.5.4 Types of thermometers

The absorber is coupled into a thermometer of different kinds. Some of the main kinds are outlined below:

- Semiconducting thermistors consist of a current biased high impedance thermistor and show a temperature dependence²⁹⁶ of $R(T) = R_0 \exp(\sqrt{T_0/T})$.
- Transition edge sensors (TES) will be covered in greater detail in section 4.5.5.
- Metallic magnetic calorimeters use the temperature dependence of the magnetic susceptibility of a material. Their advantage is a contact free readout and no energy dissipation into the absorber. A variation of this principle is the use of the flux change due to the Meissner effect in a superconducting absorber which is used in magnetic penetration detectors.

In non thermal cryogenic detection mechanisms that are suitable for array type detectors, X-ray photons generate a cloud of quasi-particles and their sensitivity is based on the low binding energy of the Cooper pairs (see also section 4.3).

- On one side of a superconducting/insulator/superconducting tunnel junction (STJ) a photon is absorbed and its energy is sufficient to split a large number of Cooper pairs. The gap energy is on the order of a few meV like in niobium with 1.47 meV or aluminium with 0.17 meV for $T=0$ ²⁹⁵. The excited electrons carry a quasi particle tunnel current through the insulator that can be measured. Since the original response from the material is close to 800 electrons per 1 eV of the original photon energy the energy resolution due to statistical fluctuations is high. These kind of detectors has been used successfully for XAS at low energies²⁹⁷⁻²⁹⁹(see comment below).
- Transition edge sensors can absorb photons in their active zone directly and act then as non thermal detectors. The total current transported through them is only partially carried by Cooper pairs. The absorbed X-ray photon reduces the number of available Cooper pairs and a larger fraction of the current is carried by quasi particles what produces a increased voltage drop over the material²⁹⁵.
- Kinetic inductance detectors could be called "pair breaking detectors". The (mainly inductive) impedance of a tuned electrical resonator is $Z_S = R + i\omega L$. Quasi particles generated by an absorbed photon alter the resistance and detune the high Q resonant circuit. An advantage of

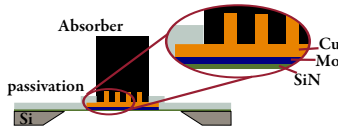


Figure 4.16. The transition edge sensor is a $2.5\mu\text{m}$ bismuth absorber on $0.2\mu\text{m}$ Copper and $0.1\mu\text{m}$ molybdenum bilayer. A meander structure of $0.5\mu\text{m}$ copper bars strengthens the proximity effect in the molybdenum locally. The structure is deposited on a thin freestanding silicon nitride membrane supported by deep etched silicon. The copper bars affect the excess noise and were extensively discussed in reference³⁰¹ and chapter 2.7 of reference²⁹⁵.

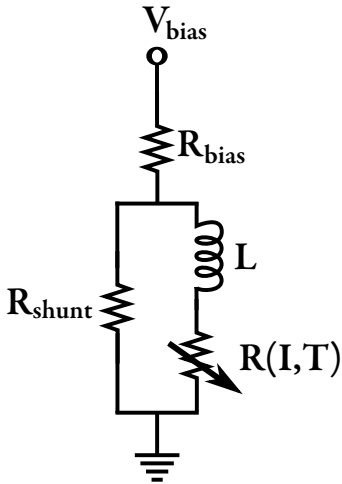


Figure 4.17. A typical readout circuit for a voltage biased transition edge sensor. The parameters for the system used are given in table 4.1. A shunt resistor R_{shunt} parallel to the out-coupling inductance L and the temperature and current dependent resistance of the TES builds the Loop. A large bias resistor (typically a few $\text{k}\Omega$) decouples the total current from the temperature variations in the TES.

these systems is the intrinsic possibility for frequency domain multiplexing of many pixels. Since this detector uses the same efficient pair breaking mechanism the number of electrons generated is high³⁰⁰.

Thermal detectors are slower in their response time compared to detectors based on "quasi" particle generation. But since the radiation loss is very small they do not show charge losses due to recombination. Non thermal detectors using the small binding energy of Cooper pairs suffer from the possibility to use thick absorbers or the high voltages used in CCDs to extract the charge carriers. At the recent Low Temperature Detector conference in Heidelberg LTD-14 (proceedings are not yet published but will appear as a special issue in the "Journal of Low Temperature Physics" shortly after the print of this thesis) sensors built with most of these principles and energy resolutions better than 5eV for the MnK_α emission lines were presented.

Which detector principle is optimal depends on the specific application. Readout speed, multiplexing, resolution, scalability, the energy range and many more factors will make one or other principle appear optimal. A good overview is given in reference²⁹⁵, and in the tutorial section of the proceedings of the series of conferences named above.

4.5.5 Transition edge sensor (TES)

The temperature sensor for the detector used in the experiment of this thesis is a transition edge sensor built using thin film technology (figure 4.16). The copper-molybdenum bilayer is adjusted to have a T_C well above the desired working point (summarized in table 4.1). The thin layer is then brought into the transition phase by applying a bias current (in form of a bias voltage V_{bias} over a high resistance, see figure 4.17). The transition is very steep and offers a very sensitive temperature sensor. The simplified thermal differential power equation for the sensor can be written as (ignoring noise terms):

$$C(T) \frac{dT}{dt} = -P_{\text{bath}}(\Delta T) + P_{\text{joule}}(T, I) + P_{\text{photon}} \quad (4.13)$$

The heat flow from the detector to the bath $P_{\text{bath}}(\Delta T)$ is dependent on the temperature difference and is defined in a linear model by the G in the numerical example in section 4.5.3. The joule heating $P_{\text{joule}}(T, I)$ by the detector bias is for a static model $\sim R(I, T) \cdot I^2$. The temperature changes generated in TES exceed the small signal limit and their extensive theoretical treatment is beyond the scope of this work. The solution of the differential equations including some nonlinear contributions

can be found in the thesis from Lindeman³⁰², in^{295;303} and citations therein. The TES is used in a voltage biased scheme ($R_{bias} \gg R_{loop} = 1/(1/R_{shunt} + 1/R_{TES})$) and the Joule heating becomes:

$$P_{joule}(T, I) \sim RI^2 \sim V^2/R_{TES}. \quad (4.14)$$

This effect gives a stabilizing negative electro-thermal feedback since with increasing temperature the resistance in the sensor increases³⁰³ (figure 4.12). The feedback reduces the Joule heating and with this reduces the total "fall" time of the signal. This is the reason why the estimated excitation decay time in the numerical example differed from the observed time (figure 4.15). A crude approximation for the correction factor can be made by assuming small and slow signals. The effective fall time would then be on the order of^{295;303}:

$$\tau_{eff} \approx \frac{\tau_0}{1 + LG}. \quad (4.15)$$

LG is the "loop gain" and is locally defined (for a constant total current) as:

$$LG = \frac{P_{joule} \cdot \alpha}{G T_0}. \quad (4.16)$$

Here α is a dimensionless parameter describing the resistance change of the TES as a function of the temperature at the working point with current I_0 , $\alpha_{I_0} = \partial \log(R)/\partial \log(T)$, G is the thermal conductance and T_0 the critical temperature (see table 4.1 and the numerical example in section 4.5.3). The loop gain can be understood as the gain of the readout circuit.

Irwin³⁰⁴ found for the energy resolution of a TES the simplified expression:

$$\Delta E_{FWHM} = 2\sqrt{2 \ln 2} \sqrt{4k_B T_0^2 \frac{C}{\alpha} \sqrt{n/2}}. \quad (4.17)$$

A high α parameter would therefore be desirable for fast and accurate photon detection. Restrictions in fabrication and the multiplexed readout, however, limit the possible values. The factor n in this formula is derived from considerations including coupling constants and excess noise and are discussed in this reference²⁹⁵. More on this topic in the discussion at the end of section 4.5.13.

Table 4.1. The estimated parameters for the TES used (at a bias point of 20% R_{normal})

G	58 pW/K
C	1.8 pJ/K
$\alpha_{I_0} = \frac{\partial \log(R)}{\partial \log(T)}$	400
$\beta_{T_0} = \frac{\partial \log(R)}{\partial \log(I)}$	2
R_{shunt}	240 $\mu\Omega$
R_{normal}	10.7 m Ω
n	3.2
T_c	117 mK
T_{bath}	85 mK

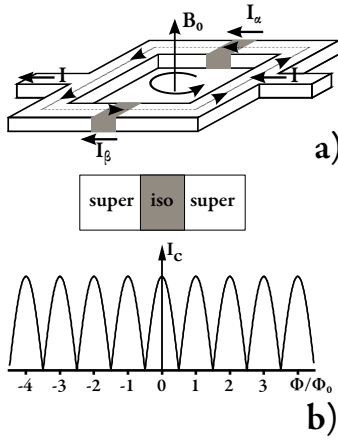


Figure 4.18. a) Schematic of a SQUID including both partial currents I_α and I_β and the induced ring shielding current. b) Modulation of the maximum current that can flow through the SQUID as function of the flux through the loop.

4.5.6 TES readout

The current going through the transition edge sensor (TES) is coupled inductively into the readout system. Each coil used in this sensitive step is wound in a complex gradiometer structure to suppress stray field with up to octapole symmetry and is shielded by superconducting layers. The current readout is done in a superconducting quantum interference device (SQUID) which consists of a superconducting loop with two interruptions in each arm called weak links (figure 4.18). Each of these weak links is a Josephson contact and can be modeled like a superconductor-isolator-superconductor tunneling contact. The maximum tunnel current through this contact which can be carried losslessly by the Cooper pairs depends strongly on the phase difference of the wave functions on both sides of the contact²⁸⁵. A field Φ_{extern} within the loop will generate a shielding ring current (dotted line) which in the simplest model generates a phase difference in each contact (D.C. Josephson effect). Let $i_n = I_C \sin \varphi_n$ be the current through each of the contacts then the total current through both contacts is:

$$i = i_1 + i_2 = 2 I_C \cos((\varphi_1 - \varphi_2)/2) \sin((\varphi_1 + \varphi_2)/2) \quad (4.18)$$

Only considering the ring current with the inductance L and a symmetric driving current the total flux in the loop would be

$$\Phi = \Phi_{extern} + L I_{circular} = \Phi_{extern} + L(i_1 - i_2)/2.$$

The phase difference $\varphi_2 - \varphi_1$ can often be assumed to be

$$n \cdot 2\pi + 2\pi\Phi/\Phi_0,$$

for integer n the total current through the contacts is then

$$i = 2 I_C \cos(\pi\Phi/\Phi_0) \sin(\varphi_1 + \pi\Phi/\Phi_0).$$

Without any self inductance the maximum current flowing through the loop corresponds to $di/d\varphi_i = 0$, giving

$$i_{max} = 2 I_C |\cos(\pi\Phi_{ext}/\Phi_0)| \quad (4.19)$$

like shown in figure 4.18b. Since the loop is a macroscopic structure, field variations below the magnetic flux quantum Φ_0 can be measured. Minute current changes in an inducing loop can induce multiple flux quanta, so techniques based on such SQUID measurements can enjoy exquisite sensitivity. SQUIDS are frequently used as sensitive current sensors, especially in systems which already provide low temperatures^{285,305,306}. In the present work SQUIDS function as current comparators. The current of two opposite wound coils is fed into one arm of the loop and the difference of the induced flux is measured³⁰⁵.

4.5.7 Multiplexing

Multiplexing is employed to read large arrays of detectors. Three types of multiplexing for low temperature detectors are commonly employed³⁰⁷. In frequency-division multiplexing (FDM) all pixels within one channel are sampled with a different frequency simultaneously. In time domain multiplexing (TDM) every pixel within one channel is switched on sequentially. In code division multiplexing (CDM) every pixel is sampled constantly but the sign of the bias modulates with a unique code. The readout electronic for the presented array was designed and fabricated in the facilities of the Quantum Devices Group at the National Institute of Standard and Technology (NIST) Boulder, Colorado US in close collaboration with their personnel. The room temperature components are presented elsewhere³⁰⁸. The cold stage multiplexed readout system has several channels of microcalorimeters (columns). Within each column, several pixels (rows) are time division multiplexed. In figure 4.19 a two pixel multiplexing system is sketched. The basic idea for the multiplexing is to couple the TES (A) inductively into a current comparator (SQUID) for each pixel (B), which may be switched on or off for the purpose of multiplexing. The outputs are summed and after some amplification and impedance matching brought to an output amplifier at room temperature (C). The signal is digitized, analyzed in a digital proportional integral derivative (PID) controller which provides the feedback voltage (E) of the close loop amplifier.

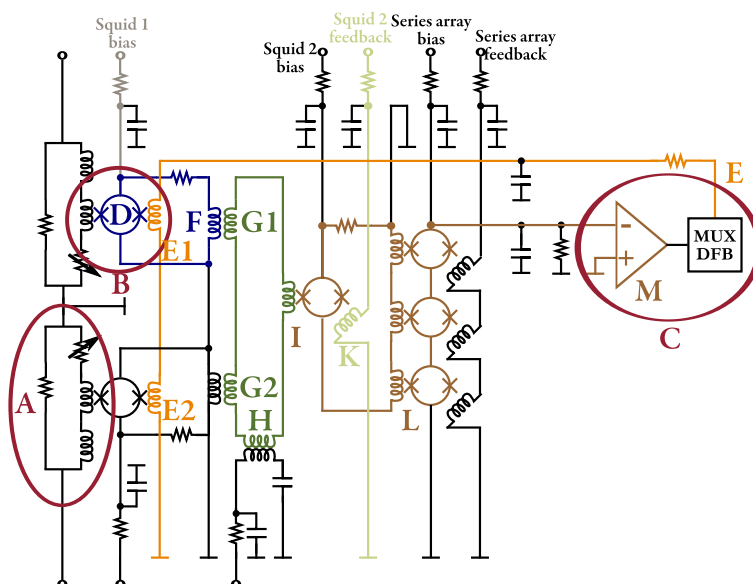


Figure 4.19. Schematic of the readout for a two pixel multiplexed system. Red rings A:TES readout loop B:SQUID current comparator C:Room temperature electronics with preamplifier and digitizer. Blue, Green, Brown amplification circuit reading the change of current through the first SQUID which is the error signal Gold:feedback current for current comparison in B, for a detailed description see text

Some further itemization of the circuit components follows:

TES readout loop (red ring A) The current through the transition edge sensor (TES) is coupled inductively to the readout loop as described in figure 4.17. The sketched primary readout loop has an additional series inductance to slow down the rising current edge of the pulse and enable the feedback loop to follow the signal development and stay locked on the working point of the SQUID (see discussion at the end of this section).

Tuned current comparison (red ring B) As described in the previous sections the current through the TES is inductively coupled into the first superconducting quantum interference device (SQUID) (blue D) over a gradiometer loop structure designed to suppress stray fields with up to octupole symmetry. Into the same coupling loop, but with opposite polarization and different inductance, a feedback channel (Gold E1) is coupled.

Current feedback (gold line) The feedback line couples into each SQUID of this column and is synchronously switched to the value that was calculated in the previous cycle to compensate for the flux induced by the TES readout loop. The signals in the SQUID (Blue D) are kept close to the working point if the feedback is fast enough. Fast rising error currents (which are then uncompensated) can induce a flux that rises a full magnetic flux quantum in the SQUID which then jumps through one full current period (equation 4.19). The feedback then stabilizes on the new current. To avoid this effect the earlier mentioned additional inductance was introduced. (see also discussion at the end of this section)

Multiplexing Each first stage SQUID is voltage biased (grey line). The bias is switched on for one SQUID at a time and the current of only one SQUID is coupled over a coupling coil (Blue F -> Green G1) into the superconducting summing loop (green loop). The summing loop is damped by a pickup coil (green H).

Amplification The summing coil is fed into a tuned current comparator (Brown I). Since the system is tuned to compensate the flux in the first stage SQUID (red ring B) the induced signal is the error signal. The tuning provided by the light green line K is setting the working point and is not changed during the multiplexing. The whole system has two SQUID-based amplification stages. In the first stage SQUID, and the second is in the readout of the summing

coil (brown I). The relative inductance in each SQUID's coupling coils determines the amplification.

Impedance matching SQUIDS are low impedance devices. A tuned multi stage serial SQUID array is used to match the impedance of the circuit to the room temperature electronics (red circle C).

Error preamplification The error signal is amplified and digitized in the room temperature electronics.

Feedback and mux The digitized error signal is converted into a feedback signal in a digital proportional-integral-derivative (PID) controller^{309–311}. The acquired feedback signal is stored and used the next time this pixel is measured. The previous feedback signal together with the measured error signal and several flags to assure synchronous data transfer are sent digitally over an optical fiber to the PC.

One readout cycle for a single pixel in the current configuration takes 640 ns. The sequence is outlined in figure 4.21:

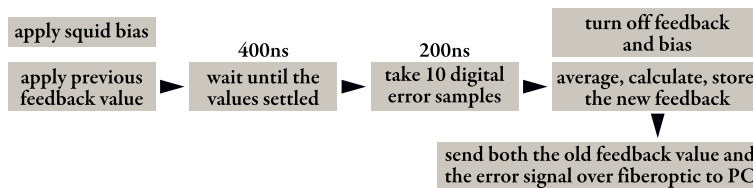


Figure 4.21. Step diagram for a single pixel. A single pixel readout cycle takes in the current configuration 640 ns (including 40 ns delay for signal transport).

In the current configuration ten pixels (rows) are multiplexed in four of the possible eight channels (columns), so that each of the pixels is sampled every 6.4 μ s. The excising array has 160 pixels and is shown in figure 4.20. During the steep signal rise after the photon absorption the feedback has to be able to follow the signal (figure fig:photonarrival). The sampling frequency limits the number of pixels that can be multiplexed. The additional inductance introduced in the TES readout loop slows down the signal transients, enabling this multiplexing scheme. If the SQUID switches over one Φ_0 into the next current oscillation the feedback follows new current at the same error value, the gain factor is different, dynamic range is lost and the energy calibration is wrong (more on this in section 4.5.13). A program is testing the current values constantly and sets the loop back to its calibration values in regular intervals. However, to not interfere with the system readout this check can only

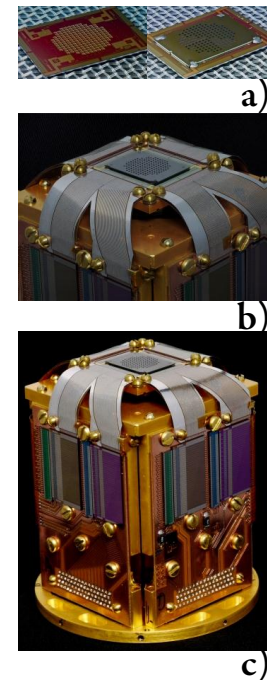


Figure 4.20. Figure A shows the installed array without (left) and with the collimator (right) in a transfer pad (courtesy Dan Schmidt NIST). The pixels are arranged in a square grid with an even 665 μ m pitch but cover a circular crosssection, to optimize the overlap with the round X-ray window. A 275 μ m thick deep etched silicon collimator (right figure) with 320 μ m by 305 μ m openings is aligned 20 μ m distant from the pixels and minimizes the photons being absorbed in the bulk silicon near the superconducting leads. Figure B shows the mounted array with flexible bent aluminium leads. The shunt resistor, inductive loads and first and second stage squids are mounted at the sides of the three dimensional structure (figure C). All four sides of the structure are connected via a flexible circuit board. The base of the structure is made of copper and covered with gold to ensure good heat contact and minimize radiative emission.

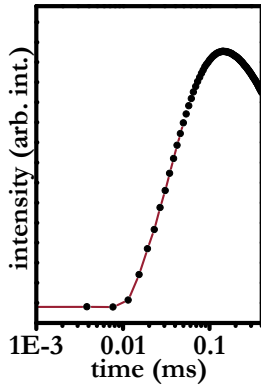


Figure 4.22. The signal change between two sampling points can be several percent for rapid changes and sparse sampling in large systems. This demands fast dynamic response for the amplifying system and induces errors in measured photon arrival time (which is an important parameter in the discrete data treatment).

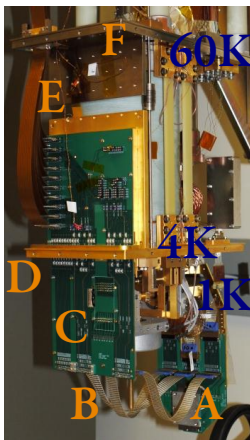


Figure 4.23. After the first two amplifications on the low temperature stage in figure 4.20 c the signal is filtered and amplified in an intermediate stage at 1 K (board A), transported over superconducting cables B to the transfer board C which is thermally located on the 4 K stage D. From where it is guided out with flexible copper leads E into the 60 K area of the cryostat F.

happen in long intervals and the time after each unlocking event is lost for data collection. The next generation room temperature readout electronics is in the final testing state and will offer a $\approx 10\times$ higher clocking speed, which will enable a larger number of multiplexed pixels. The heat capacity of the absorber and the other parameters (see table 4.1) were adjusted for a maximum photon energy of 10 keV. Above this limit the relative sensitivity of the sensor is reduced and often the feedback can not follow the signal changes (see section 4.5.13).

4.5.8 Signal transport and amplification

The eight separate columns are arranged in the physical array as 45 degree pie sections. Four of those columns, each with 10 multiplexed pixels (rows) are wire bound to a flexible superconducting connector (aluminium at 80 mK). The construction is mounted on a gold covered three dimensional copper construct with the readout and multiplexing electronics glued and wire bonded on a foldable circuit board on the four sides. The whole complex is held at the base temperature of 85 mK. The signal is transferred over long superconducting wires (see figure 4.27 G2) to a circuit board at the intermediate 1 K level (figure 4.23 A). The long superconducting wires ensure good thermal isolation at the same time as a near lossless signal transport. At the 1 K level a set of low power filters and the series array are located. Again a set of long superconducting cables transports the signal and bias currents to a transfer circuit board at the 4 K stage (figure 4.23 C). This board contains the main isolation and noise filter into the upper part of the vacuum vessel with less shielding. Flexible copper wires (figure 4.23 E) transport the signals and bias currents through the 60 K shields (figure 4.23 F) and the vacuum feedthrough into a small rack mounted on top of the cryostat. The circuits providing the bias voltages are battery driven. The amplified data is transferred via high quality coaxial cables to the readout system. The power for the readout electronics is galvanically separated from the 240 VAC power and cleaned in several band pass filters. The whole system is heavily grounded and all possible strong radio frequency noise sources in the lab have extra shielding or are disabled during the measurement. The communication with the PC is carried solely via optical cables to a custom built PCI card.

4.5.9 Temperature and noise shielding

A blackened aluminium shield mounted on the 4 K and 60 K stage together with the vacuum shield isolates the bulk of the cryostat from electro-magnetic fields present in the laser laboratory and reduces the radiation load from all but the next

cold stage. The detector package is shielded in four layers (see figure 4.24). The innermost aluminium shielding is mounted directly on the 85 mK detector package. The second and third layers (one at 4 K and another at 60 K) are made from annealed "Amumetal 4K" from the company "Amuneal". This material is designed to yield a high magnetic permeability. The outermost layer is a modified ISO 100KF vacuum flange with a standard KF port to enable the coupling to standard vacuum systems and a 25 μm Duraberyllium window. The three inner shields are closed with an exchangeable windows. Without this shielding the detector would be saturated with IR photons. In the current configuration two layers of 1 μm aluminium are mounted on each of the successive three windows on the three inner levels. For better transmission at very soft X-ray energies other radiation filter materials such as aluminium covered polymers (e.g. from companies like "Lebow Company" or Lexan) can be chosen.

4.5.10 Data recording and synchronization

The data stream in the PC is separated into the different channels belonging to each pixel. Software constantly analyzes this stream and writes a fixed data section onto the disk in a case a chosen trigger condition corresponding to photon arrival is met. This approach is based on prior developments and has some advantages over simply streaming the data to disk. During the data analysis each pulse can be treated separately and statistical exclusion criteria can be used to minimizing the processing time. Real time processing capabilities are under development and will allow flexible record length for each pulse^{312;313} (see also section 4.5.13 for more details). The length of the recorded pulse is optimized according to the expected signal decay time²⁷⁵. A longer recording is beneficial for the energy resolution since the pulse can be fitted over a longer period of time and the absorber can cool down to its base temperature (figure 4.25) but it also limits the possible maximum count rate and with this increases the measurement time. For the current setup a minimum record length of ~ 12 ms has been chosen, corresponding to a maximum pixel count rate of ≈ 80 Hz. In the initial (and still applicable) algorithm, records are discarded if they contain two or more distinguishable events. The probability for exactly one photon to be absorbed within one record length is follows a Poisson distribution⁸⁰. With 80 Hz maximal trigger rate the optimal event "survival" rate v_{opt} for exactly one photon per record length is:

$$f_{poisson}(k; \lambda) = \frac{\lambda^k e^{-\lambda}}{k!} \Rightarrow \lambda_{k=1}^{max} = 1 \quad (4.20)$$

$$f(1; \lambda_{max}) = 1/e \quad v_{opt}^{80Hz} = 29,4Hz \quad (4.21)$$

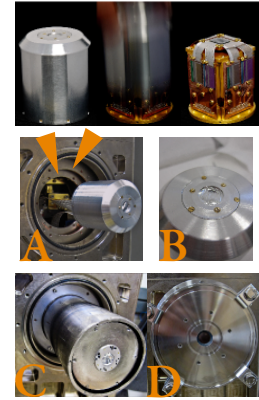


Figure 4.24. The detector package is shielded with a superconducting 1 mm aluminium cover which is mounted directly on the 85 mK copper construct and suspended outside the cryostat body (A). The arrows mark the inner 4 K and 60 K aluminium shielding. (B) Depending on the application different window materials can be chosen (see text). Annealed magnetic shielding (A4K material produced by Amuneal) is mounted on the two inner shields and extends over the detector package. Each shield is closed with a small exchangeable window. The outer vacuum shield has a removable ISO 100 KF flange. For freestanding operation a 25 μm Duraberyllium window is glued behind the 10.2 mm diameter opening in a modified ISO 100 flange and offers a ISO KF 40 connection to standard vacuum systems.

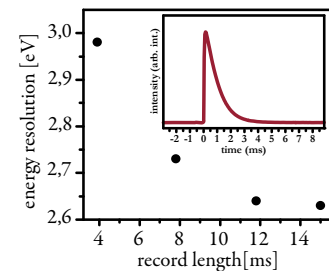


Figure 4.25. The energy resolution in dependence of the recorded pulse-length for a typical pixel. The inset shows the typical detector response on a 6 keV photon.

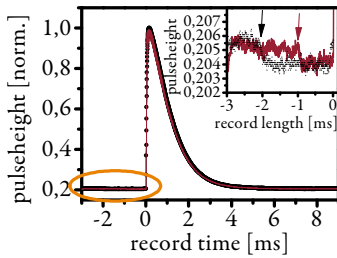


Figure 4.26. Simultaneous arrival of photons induces crosstalk between different pixels. The direction of the signal could point to an inductive origin of this signal.

The signal between two different pixels does show crosstalk features if a photon is simultaneously absorbed in a second pixel which is thermally or electrically close. An increased total flux adds to this problem and a sparse excitation with only slightly less effective counts is beneficial for the energy resolution. In the current detector module pixels with minimal crosstalk among those available were chosen. Nevertheless, it does contribute to the total noise level and needs to be addressed in the next generation of detectors. The crosstalk is best visible in the recorded calmer region just before the rise of the signal (figure 4.26).

The two biggest uncertainties left in the measurement are baseline/gain shifts due to variations of the base temperature (see section 4.5.11) and the asynchronous arrival of the photos as measured by the discrete sampling points. The large intensity change between two of the sparse points especially for large areas on the rising edge has a significant influence on the integrated signal. In future iterations of the electronics this could be addressed by recording the laser arrival time.

This prototype version of the detector operates as a free running machine. Laser on - laser off information can currently be included by modulating the total incoming X-ray flux to signal a change in experimental conditions (blocking the X-ray generation process by e.g. blocking the laser beam) in later iteration this information might be written into the data stream.

4.5.11 Temperature control system

The cryostat is based on a design from NIST and was built by High Precision Devices Inc. in Boulder, Colorado. Driving and control electronics were purchased separately or built as part of this thesis work. The controlling software was also partly written in the course of this work. The detector operating at the bath temperature of 85 mK is mechanically supported in several stages from the casing of the room temperature cryostat. Each stage has its own cooling and the weight is carried by materials with low heat conductivity. The cryostat is evacuated to pressures below 4×10^{-7} mbar before cooling. The large cold areas of the shielding materials described in the previous chapter act as a cryopump¹⁵⁴ and further reduce the pressure. The first two stages are carried by glass fiber constructs and are cooled by a two stage pulse tube cooler. The cooling concept is sketched in figure 4.27. An external water cooled compressor generates a pressure difference between two long pressurized gas lines. An external rotating valve converts this pressure difference into a 1 Hz pulsating pressure (A). The separation of valve and pulse tube reduces the mechanical vibration transmitted into the cryostat. The pulsating pressure wave drives a two stage pulsation cooler based on a Stirling process inside the vacuum

vessel. The cooling medium used is 99.9995% pure helium. The whole cryostat is supported by a highly adjustable table separated from the optical laser and X-ray table. Part B and C of figure

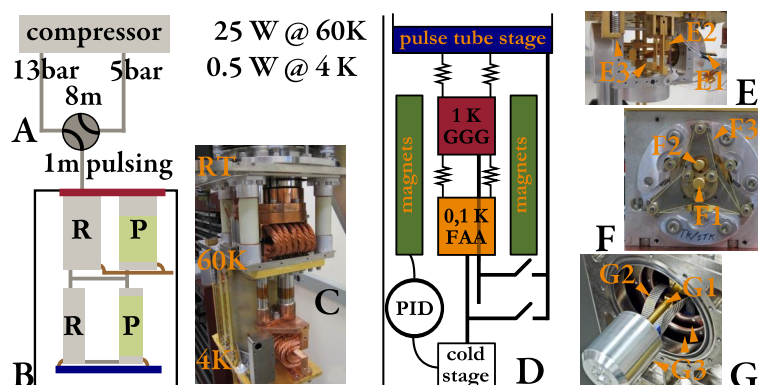


Figure 4.27. Cryostat cooling system A) an external compressor and motor driven valve generates a pulsating pressure difference that drives a two stage pulse tube cooler in the cryostat B) in which each tube is split in two parts, consisting of a regenerator R and the pulse tube P. The cold stages are thermally attached to the respective pulsetube stage. C) Photograph of the system with indicated temperature stages. D) Sketch of the adiabatic demagnetization refrigerator with the indicated pulse tube end stage at 4 K and two heat switches, superconducting magnets and paramagnetic salt pills. E) Close up of the heat switches. F) Close up of the suspended attachment of the copper rods carrying the detector package. G) Close up of the protruding detector package with indicated superconducting connections G2 and the thermal and electric shields G3 (see text)

4.27 show a simplified sketch of the pulse tube and a photograph of the system. The gas pulsation drives a heat transfer between the cold section of the regenerator R and both ends of the tube. The principle was described by Gifford³¹⁴ and has the advantage of removing all moving parts but the gas from the cryostat. An overview and comprehensive description of the cooling principle can be found in references^{315;316}.

The first pulse tube cold stage is at ≈ 60 K and the second stage slightly below 4 K. To minimize the transmitted vibrations and allow for thermal expansion the intermediate cryostat stages are coupled to the pulse tube via annealed flexible copper wires.

The second cooling stage is an adiabatic demagnetization refrigerator^{317–319} based on the magneto-caloric effect. The system is sketched in figure 4.27 D. The two active materials gadolinium gallium garnet (GGG) and ferric ammonium alum (FAA) are strongly coupled to their respective cold stages on the detector side, but only weakly coupled to the 4 K cold stage. An externally controllable heat switch (E2 and E3) can generate a good thermal connection to the pulse tube end stage. The magnetic field used in the magnetization process is generated by a superconducting solenoid with ≈ 4.2 T at 9.3 A driving current. The driving current of the magnet is close to the critical current of the coil. This and the thermal/physical stress generated during the magnetization cycle limits the possible rate of magnetization and demagnetization. At the end of the cooling cycle a residual (weak) magnetic field is used to control the cooling power of the

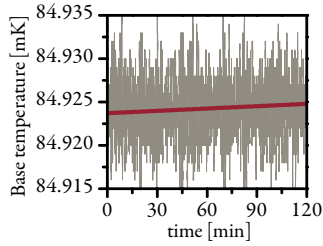


Figure 4.28. Base temperature fluctuation vs time. The oscillations are with 15 μ K smaller than the long term temperature drift over 14 h operation time.

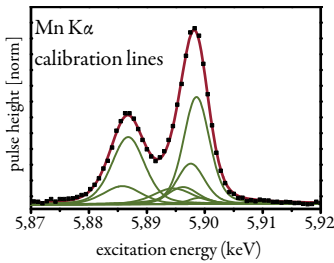


Figure 4.29. Fitted calorimetric spectrum of a single pixel. This spectral quality was obtained after compensating for the artificially introduced temperature fluctuations as described in section 4.5.13. The fit uses the parameters given in table 4.2 with the total intensity, a linear shift and a gaussian broadening function as free parameters.

Table 4.2. Fit parameters for the manganese $K\alpha$ fine structure assuming a gaussian line shape after Hölzer³²⁰ modified by Porter³²¹.

Int[rel]	E[eV]	FWHM[eV]
1.000	5898.853	1.715
0.649	5887.743	2.361
0.399	5897.867	2.043
0.312	5886.495	4.216
0.224	5894.829	4.499
0.187	5896.532	2.663
0.0510	5899.417	0.969
0.0113	5902.712	1.5528

cryostat and adjust the temperature. Temperatures above 1 K are measured with silicon diodes. The low temperature 85 mK sensor is a ruthenium oxide thermistor read with a resistor bridge. The output of the resistor bridge is the input to an analogue proportional-integral-derivative (PID)^{309–311} controller (Stanford research system). Its output is amplified by a voltage controlled high current analogue amplifier that is used to drive the magnet.

Vibrations caused by the pulse tube also the slow and non-linear thermal response of the system and the limited available cooling power make the tuning of the feedback loop challenging. Standard tuning techniques like the Ziegler Nichols tuning method^{309;311} led to system instabilities. The temperature stabilization achieved is nevertheless sufficient to run the system with some additional correction in the data analysis. Figure 4.28 shows the fluctuations and long time temperature drifts in the system which need to be considered in the data analysis (see section 4.5.13).

The detector package is mounted on a gold coated copper rod (E1, F1 and G1) at 85 mK protruding horizontally from the cryostat axis (figure 4.27 G). The rod is suspended by fine Kevlar fibers (F3) that are attached to the second rod at 1 K (E2 and F2). This second rod is in turn suspended by similar fibers that are attached to the copper structure at 4 K. All electrical connections to the cold stages are superconducting and therefore have a low heat conductivity. This isolated construction enables a total standing time of up to 16 h without any bias currents in the detector and 12 – 14 h under operating conditions. After this time the adiabatic demagnetisation refrigeration process must be performed again.

4.5.12 Calibration lines

Two radioactive materials were used for energy calibration of both the CCD and the microcalorimeter detectors. The decay from $^{241}_{95}\text{Am}$ and $^{55}_{26}\text{Fe}$ are given in the database from Chechev³²² and listed in table 4.3. During the experiment fluorescence lines of the sample and filter materials are excited which appear at known energies throughout the whole spectrum (see section 4.5.13).

Table 4.3. The decay from ${}_{95}^{241}\text{Am}$ and ${}_{26}^{55}\text{Fe}$ with the energy in keV and the probability for the particular transition after a disintegration event in percent.

${}_{95}^{241}\text{Am} \xrightarrow{\alpha} {}_{93}^{237}\text{Np}$			${}_{26}^{55}\text{Fe} \rightarrow {}_{25}^{54}\text{Mn}^*$		
	E keV	prob. %		E keV	prob. %
Np L1	11.89	0.848	Mn K α_2	5.8877	8.45
Np L α	13.9	13.03	Mn K α_1	5.8988	16.56
Np L η	15.86	0.31	Mn K β	6.4905	3.4
Np L β	17.81	18.55			
Np L γ	20.82	4.81			
γ	26.3446	2.4			
γ	59.54	35.78			

4.5.13 Data extraction, energy calibration and drift correction

The principle behind the data extraction was discussed in a paper by Doriese et al.²⁷⁵. The recorded signal for each event is composed of the sum from feedback signal and error signal, since the response is faster than the feedback can follow. The signal is sampled at discrete intervals and shows a complicated decaying function. The extraction and noise reduction of every event is based on the optimal filter²⁹⁴ algorithm. The assumption is that every pulse (close to the calibrated energy) is of the same shape, discrete and homogeneously sampled. Some pulses that are assumed to be perfect are selected, averaged and analyzed in the Fourier space according to their power spectrum. A filter template is generated using the optimal frequency cutoff which is then transformed back into the time domain. The product between the filter template and the original pulse in the time domain was shown to be proportional to the energy of the event³⁰².

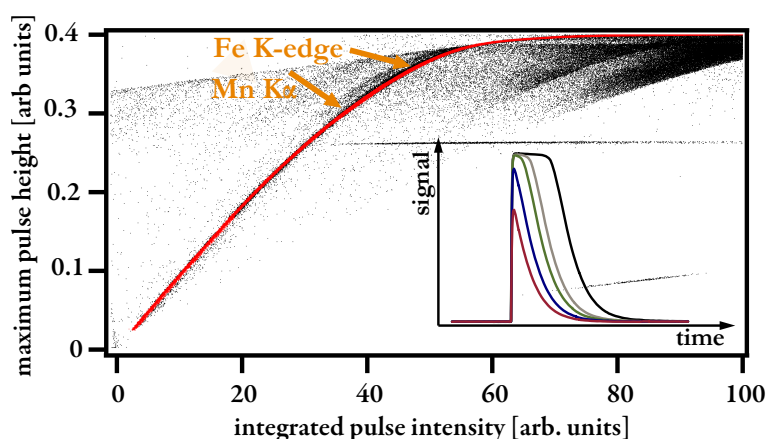


Figure 4.30. The maximum signal deviation vs integrated peak intensity for all recorded events of a single pixel during the collection of the ferrocene X-ray absorption spectrum. Statistical selection processes rejected those recorded events containing more than one photon or other additional noise contributions. The remaining events are marked in red. The orange arrows show the approximate position of the manganese K α radiation and the iron K-edge. At large deposited energies (ordinate) the sensor becomes normally conducting and loses its sensitivity. The lost sensitivity of the detector results in a flattening of the pulse shape for increasing photon energies as shown in the inset.

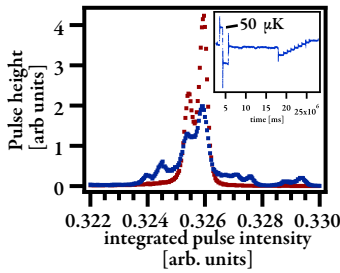


Figure 4.31. Pulse height spectrum of ^{55}Fe emission data using artificially introduced temperature fluctuations of up to $\pm 50\ \mu\text{K}$ shown in the inset before (blue line) and after correction red (red line).

A bachelor project was supervised during this work to develop a parallelized implementation of this code for graphical processing units. A spectrum for time resolved measurements contains more than 1×10^{10} absorption events. The filter template is specially generated for each detector but assumed to be constant for all events recorded with the same detector. Graphical processing units offer a large number of parallel nodes (processing units) that have to access a constant stream of adjacent data storage. The results of this project will be published separately³²³ and showed a significant acceleration in the application of this filter step. The this project will contribute to the development of realtime data processing.

The bias settings of the SQUID amplification and the PID settings controlling the signal feedback are tuned after every cooling cycle. The magnetic flux trapped in the superconducting elements and variations in the laboratory conditions make these adjustments necessary. The detector response function is linear only in small regions. The phonon transport conditions inside the absorber, between the contact layers and into the thermometer and heat bath are the object of very active research³²⁴ and difficult to model. Figure 4.30 shows the peak value of the response of a single pixel as function of the integrated value, where the latter is assumed to be closely related to the deposited energy. The compromise of speed and energy resolution that had to be taken operates this detector in a regime where the maximum pulse height is no longer strictly proportional to the integrated intensity. In practice this requires is a calibration for every run on every pixel using radiation of known and discrete spectral distribution.

Temperature fluctuations and drift induced by the cryostat or the heating of electrical elements, laboratory conditions and the photon flux do change local temperature off each pixel during one day of operation. The nonlinear temperature response generates a temperature dependence of the detector gain. Fluctuations as low as $20\ \mu\text{K}$ result in a significant reduction of the energy resolution. Since the TES is in principle a very sensitive thermometer we can use its recorded baseline level before every pulse to track the temperature fluctuations and generate, using artificially induced temperature fluctuations during each measurement cycle, a correction function for every pixel (figure 4.31).

Figure 4.32 contains the filtered pulse-height spectrum of the ferrocene sample recorded with the micro-calorimeter detector array and the laser-plasma source including the ^{55}Fe calibration data. Several prominent features originating from material in or close to the beam-path like the copper, aluminium and silicon $K\alpha$ emission (fluorescence from filters and detector mask) or the strongest absorption edges. Each of those features is added to a separate spline generated for each pixel. The splines are then

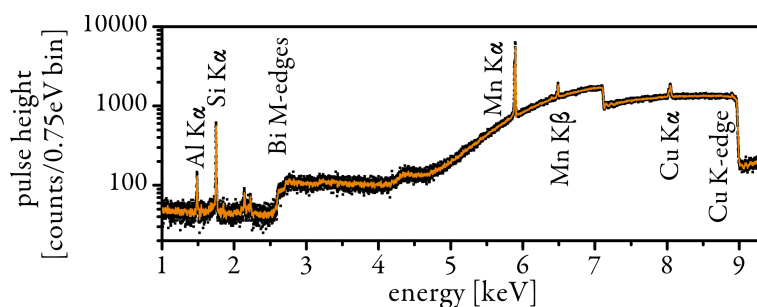


Figure 4.32. Pulse-height dataset containing the X-ray transmission spectrum of ferrocene powder on Kapton tape spectra recorded with the micro-calorimeter array and the laser plasma source. The main spectral features used for calibrating are outlined.

used to calibrate the filtered and integrated arrays response to a corresponding energy. Events can then be binned in whatever way is deemed suitable. For example, presentations on an energy scale would typically use a constant energy interval binning scheme whose interval accommodates the average energy resolution of the pixels. Alternatively for EXAFS analysis one seeks a constant binning interval in the photoelectron's k (momentum) space. This amounts to binning in intervals that increase quadratically in energy above the absorption edge (equation 3.5). The possibility of arbitrarily binning multiple, simultaneously acquired spectral features either during or after the data collection is a particular strength of this technique.

It can be surmised that in time, and with ongoing developments, it will be possible to fit molecular structures during collection, terminating the data collection when the desired structural accuracy has been attained.

ABBREVIATIONS

AES	Auger electron spectroscopy
APD	avalanche photodiodes
APS	Advanced Photon Source
BBO	$\beta - BaB_2O_4$
BCS	Bardeen, Cooper and Schrieffer
CCD	charge coupled devices
CMOS	complementary metal oxide semiconductor
eV	electron volt
EXAFS	extended X-ray absorption fine structure
KID	kinetic inductance detector
NIST	National Institute of Standard and Technology
RIXS	resonant inelastic X-ray scattering
SASE	self amplified spontaneous emission
SQUID	superconducting quantum interference device
TDM	time domain multiplexing
TES	transition edge sensors
Ti:Saph	titanium doped sapphire
XAFS	X-ray absorption fine structure
XANES	X-ray absorption near edge structure
XAS	X-ray absorption spectroscopy
XPS	X-ray photoelectron spectroscopy

APPENDIX

Vectorized single pixel analysis method

Most advanced codes for particle tracking and analysis are very expensive in computing power. In high level programming languages codes become fast if the optimized and built in matrix routines are used. The code described here accelerated the processing on a 2 GHz double core processor from 500 ms/frame to 20 ms/frame. Which was limited by the data transfer from the storage medium and might be accelerated further. The algorithm

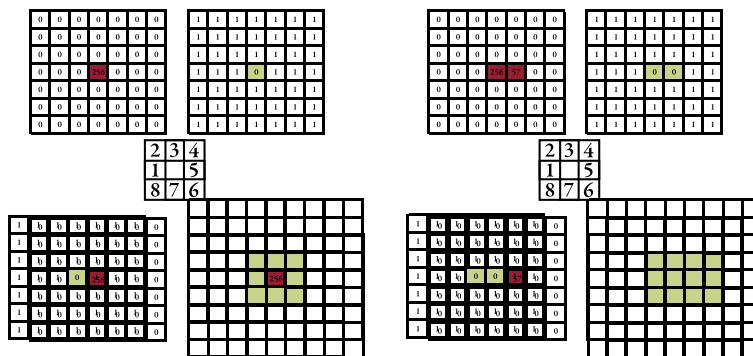


Figure 1. Fast matrix based single pixel analysis method. The left hand side shows the structure if only a single pixel has a non zero entry. On the right hand side two neighboring cells are filled. The algorithm is described in the text.

is: Take the original data matrix, apply the desired threshold and generate two matrices. The first matrix contains the data, and zeros where the data is below the threshold. The second matrix has a zero in pixels above the threshold, and 1s elsewhere. Now the contents of this second matrix is successively multiplied with the thresholded matrix containing the data with a shift of one step in all 8 directions. If two adjacent pixels were exposed above threshold both will be multiplied by zero in this procedure and erased. The new matrix contains only the necessary amount of data and can be stored space optimized or further processed.

Laser alignment procedure by Jens Uhlig January 2012

Since this is a commercial system which was designed to be "hands off" no alignment instructions are available. During the course of this work the optimization of the contrast ratio and the minimization of aberrations introduced into the beam played a crucial role. This procedure is designed to give a brief account of the every day alignment procedures necessary to operate the laser plasma source.

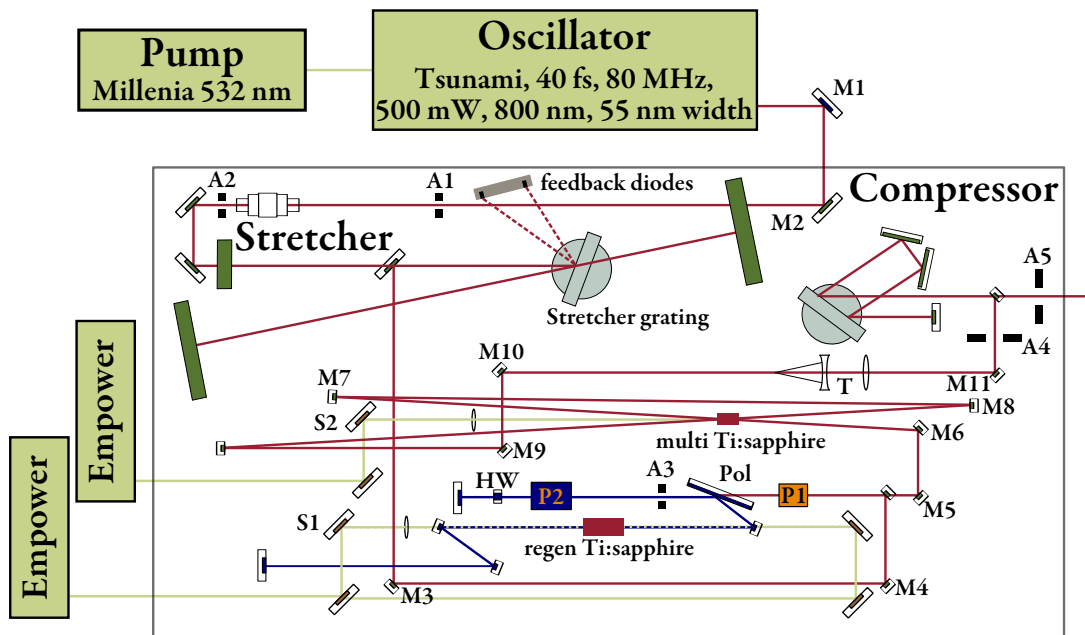


Figure 2. Laser amplifier used in the Chemical Physics Millennia laser lab, 2011 (see text for details)

- (i) Match the spectrum and the power with prism only, if possible. For this shine the Tsunami output on the power meter and use the fiber optics and the saved spectrum as reference. Note that the spectrum differs from different reflective surfaces. From time to time check with a single shot auto-correlator for the variations in the timing and wavefront tilt (rotate auto-correlator by 90 deg). They are an indication for damages in the crystal.
- (ii) If there is a problem to reproduce the spectrum or if the total power suddenly drops play with the alignment slits to check if the beampath has changed and iterate with the

prim. (560 mW output is normal, with time and dirt above 400 mW is fine). Below 150 mW is not enough to seed the regenerative amplifier.

- (iii) If the spectrum is still not matching the reference or the mode-locking is lost easily, carefully adjust the end mirrors (one at a time and as little as possible) If you continue to have problems to mode-lock at a chosen position you may play with the acoustic modulator. If in doubt, start in the middle of its range.
- (iv) align with M1 and M2 on A1 and A2 (Stretcher alignment) If everything is fine the two feedback diodes should see the second order reflection from the stretcher grating. If not, repeat the alignment and use the milled green alignment tool to check the whole path. Measure the spectrum after the stretcher at this point. It should not be clipped. The grating is a bit too narrow (there is a small clip on both sides) but we should get 55 – 60 nm bandwidth through the system.
- (v) In the spectra control software open Pockels cell P1 (channel 1) to admit the seed beam and close the cavity (open channel 2 but keep channel 3 off!)
- (vi) Use M3 and M4 to get the earliest build up.
- (vii) Align the Pockels cell P2 to get a symmetric "Isogyre" picture with 4 poles centered on A4. The beam passes the polarizer several times and should be isolated in the center part (dark with blocked Pockels cell). This alignment is one of the crucial steps if everything else is fine.
- (viii) Check the power and contrast with the multipass amplifier off and on. With the pump laser for the regenerative amplifier pump at 17 A and for the multipass at 16 A the out coupled pulse should have 3 mJ with the regenerative amplifier only and 5.8 mJ with both amplifiers. The averaged leak power should be below 200 μ J. If these conditions are not met continue try the instructions below this section.
- (ix) Check that the Isogyre picture is centered on A4 (flip up with blocked beam) and A5, if this was still fine nothing did move and the laser should be aligned. If this is not aligned adjust M9 and M10 to go centered through the telescope (use the back reflection of the lens surfaces and bring it through A4 then use M11 to go through A5.
- (x) Fine tune the two gratings start by adjusting only one of them. It is better to tune the compressor grating at the beginning, assuming that the everything else didn't

move. During adjustments, keep the previous settings. Turn a quarter turn, re-compress and check the output on the auto-correlator again. If the pulse cannot be made briefer than 50 fs with this method check the spectrum inside the laser to get an indication for where the limitation is originated.

- (xi) Check with the Pulsecout autocorrelator for side peaks which might point to damaged optics.(there is a internal reflection at 2.16 ps)
- (xii) check the full output on a photodiode for the achieved contrast ratio
 - The contrast to leaked peaks (other round trips) should be at least $1:10^3$
 - The timing of the Pockels cells P2 channel 3 is the first point to check for leaks. Then channel 2 and the alignment.
- If the output of the regenerative amplifier with 17.0 A gives < 2.8 mJ play with the seed pulse again and optimize the buildup
- iterate with S1 if necessary
- If the output is still not sufficient one roundtrip of 10 ns The added dispersion will change the compression needed (the cavity should only be touched by experts who do not need this manual)
- With a pump beam of 16 A in the regenerative amplifier the output should be at least 5.8 mJ.
- Check with S2 the overlap of the pump laser. If this was not sufficient the multipass will need a new alignment with the milled alignment tool. (marked positions inside the laser) check if you get the beam with M6 only aligned before and after the crystal. if not you will have to use M5 too but this means the 3mJ option is lost and needs to be realigned later. M7 should be hit a little bit to the lower left side. M7 and M8 bring you through the second pass. You have to bring the beam again centered trough the telescope and the compressor.
- The power before the compressor should be 4.2 mJ without the multipass amplification at 17 A and above 6.8 mJ with Multipass pump laser at 17 A and you should have a nice spectrum there. Check the upper right corner of the Stretcher grating for damage (that is the last point the

compressed pulse is hitting and the one getting damaged first)

REFERENCES

1. NORRISH, R. G. W. ; PORTER, G.: Chemical Reactions Produced by Very High Light Intensities. in: *Nature* 164 (1949), October, nr. 4172, p. 658–658
2. partly taken from Wikipedia, idea based on NASA *The electromagnetic Spectrum*. http://en.wikipedia.org/wiki/File:EM_Spectrum_Properties_edit.svg, last checked: 2011-11-24
3. SHANNON, Claude ; WEAVER, Warren: *The mathematical theory of communication*. Urbana : University of Illinois Press, 1998. – ISBN 9780252725463
4. ALS-NIELSEN, J. ; MCMORROW, Des: *Elements of modern X-ray physics*. Wiley Chichester, 2001. – ISBN 9780471498582
5. ZEWAİL, Ahmed H.: Femtochemistry. Past, present, and future. in: *Pure and Applied Chemistry* 72 (2000), nr. 12, p. 2219–2231
6. ROUSSE, Antoine ; RISCHEL, Christian ; GAUTHIER, Jean-Claude: Femtosecond x-ray crystallography. in: *Reviews of Modern Physics* 73 (2001), January, nr. 1, p. 17–31
7. CHERGUI, Majed ; ZEWAİL, Ahmed H.: Electron and X-ray methods of ultrafast structural dynamics: advances and applications. in: *Chemphyschem : a European journal of chemical physics and physical chemistry* 10 (2009), January, nr. 1, p. 28–43
8. BRESSLER, C ; CHERGUI, Majed: Ultrafast X-ray absorption spectroscopy. in: *Chemical Reviews* 104 (2004), nr. 4, p. 1781–1812
9. BRESSLER, Christian ; CHERGUI, Majed: Molecular structural dynamics probed by ultrafast X-ray absorption spectroscopy. in: *Annual review of physical chemistry* 61 (2010), March, p. 263–82
10. BARGHEER, Matias ; ZHAVORONKOV, N ; WOERNER, M ; ELSAESSER, Thomas: Recent progress in ultrafast X-ray diffraction. in: *Chemphyschem : a European journal of chemical physics and physical chemistry* 7 (2006), April, nr. 4, p. 783–92
11. GRÄTZ, Matthias: *Characterisation and Application of a Laser-Based Hard X-Ray Source*. Lund, Lund University, PhD Thesis, 1998
12. SJÖGREN, Anders: *Laser-Matter Interactions at Extreme Irradiance: X-ray Generation and Relativistic Channelling*, Lund University, PhD Thesis, 2002
13. TILLMAN, Carl: *Development and Characterisation of a Laser-Based Hard X-ray Source*, Lund University, PhD Thesis, 1996

14. HARBST, Michael: *Generation and Applications of Short-Pulse X-ray Radiation*. Lund, Lund University, PhD, 2005
15. *Lund Laser Center (LLC)*. <http://www-llc.fysik.lth.se/>, last checked: 2011-12-03
16. LUNDH, Olle: *Laser-driven beams of fast ions, relativistic electrons and coherent x-ray photons*, Lund University, PhD Thesis, 2008. – Lund Reports on Atomic Physics LRAP-391
17. LINDAU, Filip: *Laser-driven particle acceleration: Experimental investigations*, Lund University, Doctoral Thesis, 2007. – 211 S. – Lund Reports on Atomic Physics LRAP-378
18. RÖNTGEN, Wilhelm C.: Über eine neue Art von Strahlen: vorläufige Mitteilung. (1895)
19. KOCH, H. ; MOTZ, J.: Bremsstrahlung Cross-Section Formulas and Related Data. in: *Reviews of Modern Physics* 31 (1959), October, nr. 4, p. 920–955
20. PRATT, R H.: Bremsstrahlung energy spectra from electrons of kinetic energy $1 \text{ keV} < T_1 < 2000 \text{ keV}$ incident on neutral atoms $2 < Z < 92^*$. in: *Atomic Data and Nuclear Data Tables* 20 (1977), August, nr. 2, p. 175–209
21. MCCALL, G H.: Calculation of X-ray Bremsstrahlung and characteristic line emission produced by a maxwellian electron-distribution. in: *Journal of Physics D-Applied Physics* 15 (1982), nr. 5, p. 823–831
22. SELTZER, S ; BERGER, M: Bremsstrahlung spectra from electron interactions with screened atomic nuclei and orbital electrons. in: *Nuclear Instruments and Methods in Physics Research Section B: Beam Interactions with Materials and Atoms* 12 (1985), August, nr. 1, p. 95–134
23. LAMOUREUX, M ; WALLER, P ; CHARLES, P ; AVDONINA, N B.: Bremsstrahlung from thick targets and a diagnostic for electron energy distributions. in: *Physical Review E* 62 (2000), nr. 3, p. 4091–4095
24. CHEN, Z L. ; ZHANG, J ; LIANG, T J. ; TENG, H ; DONG, Q L. ; LI, Y T. ; SHENG, Z M. ; ZHAO, L Z. ; TANG, X W.: Z-dependence of hot electron generation in femtosecond laser interaction with solid targets. in: *Journal of Physics B-Atomic Molecular and Optical Physics* 37 (2004), nr. 3, p. 539–546
25. GALY, J ; MAUČEC, M ; HAMILTON, D J. ; EDWARDS, R ; MAGILL, J: Bremsstrahlung production with high-intensity laser matter interactions and applications. in: *New Journal of Physics* 9 (2007), February, nr. 2, p. 23–23
26. HEMBERG, O ; OTENDAL, M ; HERTZ, Hans M.: Liquid-metal-jet anode X-ray tube. in: *Optical Engineering* 43 (2004), nr. 7, p. 1682–1688
27. TUOHIMAA, Tomi: *Spontaneous and stimulated X-ray Raman scattering*. Stockholm, KTH Stockholm, PhD Thesis, 2011
28. WIEDEMANN, Helmut: *Synchrotron Radiation (Advanced Texts in Physics)*. Springer, 2010. – 274 S. – ISBN 3642077773
29. DUKE, Philip: *Synchrotron Radiation: Production and Properties (Oxford Series on Synchrotron Radiation)*. Oxford University Press, USA, 2009. – 251 S. – ISBN 0199559090
30. WERIN, Sverker ; THORIN, Sara ; ERIKSSON, Mikael ; LARSSON, Jörgen: Short pulse facility for MAX-lab. in: *Nuclear Instruments and Methods in Physics Research Section A: Accelerators, Spectrometers, Detectors and Associated Equipment* 601 (2009), nr. 1-2, p. 98–107

31. KHAN, Shaukat: *Collective Phenomena in Synchrotron Radiation Sources: Prediction, Diagnostics, Countermeasures (Particle Acceleration and Detection)*. Springer, 2011. – 203 S. – ISBN 364207068X
32. JONES, R.Clark: On The Relativistic Doppler Effect. in: *Journal of the Optical Society of America* 29 (1939), August, nr. 8, p. 337
33. TANAKA, Takashi ; KITAMURA, Hideo: *Spectra - a synchrotron radiation calculation code*. <http://radiant.spring8.or.jp/spectra/>. Version: 2011, last checked: 2011-12-03
34. THOMPSON, A. C. (Publ.) ; VAUGHAN, D. (Publ.): *X-ray Data Booklet*. Second. Lawrence Berkeley National Laboratory, University of California, 2001
35. CLARKE, James A.: *The Science and Technology of Undulators and Wigglers*. vol. 1. Oxford, England : Oxford University Press, 2004. – ISBN 9780198508557
36. SCHOENLEIN, R. W.: Generation of Femtosecond Pulses of Synchrotron Radiation. in: *Science* 287 (2000), March, nr. 5461, p. 2237–2240
37. ZHOLENTS, A. ; HEIMANN, P. ; ZOLOTOREV, M. ; BYRD, J.: Generation of subpicosecond x-ray pulses using RF orbit deflection. in: *Nuclear Instruments and Methods in Physics Research Section A: Accelerators, Spectrometers, Detectors and Associated Equipment* 425 (1999), nr. 1-2, p. 385–389
38. WALDSCHMIDT, Geoff J. ; BORLAND, Michael ; CHAE, Yong-Chul ; HARKAY, KKatherine C. ; HORAN, Douglas ; NASSIRI, Alireza: Status of RF Deflecting Cavity Design for the Generation of Short X-ray Pulses in the Advanced Photon Source Storage Ring. in: *Proc of the 10th European Particle Accelerator Conference*. Edinburgh, 2006, 3460
39. *Free electron laser FLASH*. <http://flash.desy.de/>, last checked: 2011-12-03
40. *Free electron laser SACLA*. <http://xfel.riken.jp/eng/index.html>, last checked: 2011-12-03
41. *Free electron laser SLAC*. https://slacportal.slac.stanford.edu/sites/lcls_public/Pages/Default.aspx, last checked: 2011-12-03
42. GALAYDA, John N. ; ARTHUR, John ; RATNER, Daniel F. ; WHITE, William E.: X-ray free-electron lasers present and future capabilities [Invited]. in: *Journal of the Optical Society of America B* 27 (2010), October, nr. 11, p. B106
43. *Lightsources.org*. www.lightsources.org, last checked: 2011-12-03
44. SPENCE, D. E. ; EVANS, J. M. ; SLEAT, W. E. ; SIBBETT, W.: Regeneratively initiated self-mode-locked Ti:sapphire laser. in: *Optics Letters* 16 (1991), November, nr. 22, p. 1762
45. HILBORN, Robert C.: Einstein coefficients, cross sections, f values, dipole moments, and all that. in: *American Journal of Physics* 50 (1982), nr. 11, p. 982
46. SALEH, Bahaa E. A. ; TEICH, Malvin C.: *Fundamentals of Photonics*. 2nd. New York, USA : John Wiley & Sons, Inc., 2007 (Wiley Series in Pure and Applied Optics). – ISBN 0471839655
47. STRICKLAND, Donna ; MOUROU, Gerard: Compression of amplified chirped optical pulses. in: *Optics Communications* 55 (1985), October, nr. 6, p. 447–449

48. BACKUS, Sterling ; DURFEE, Charles G. ; MURNANE, Margaret M. ; KAPTEYN, Henry C.: High power ultrafast lasers. in: *Review of Scientific Instruments* 69 (1998), nr. 3, p. 1207
49. DAIMON, Masahiko ; MASUMURA, Akira: Measurement of the refractive index of distilled water from the near-infrared region to the ultraviolet region. in: *Applied Optics* 46 (2007), nr. 18, p. 3811
50. GENOUD, Guillaume: *Laser-Driven Plasma Waves for Particle Acceleration and X-ray Production*, Lund University, PhD Thesis, 2011. – 214 S. – Lund Reports on Atomic Physics LRAP-443
51. SVANBERG, S ; LARSSON, J ; PERSSON, A ; WAHLSTRÖM, Claes-Göran: Lund high-power laser facility-systems and first results. in: *Physica Scripta* 49 (1994), February, nr. 2, p. 187–197
52. GENOUD, Guillaume ; WOJDA, F ; BURZA, M ; PERSSON, A ; WAHLSTRÖM, Claes-Göran: Active control of the pointing of a multi-terawatt laser. in: *The Review of scientific instruments* 82 (2011), March, nr. 3, p. 033102
53. GIBBON, P.: *Short Pulse Laser Interactions with Matter: An Introduction*. World Scientific Publishing Company, 2005. – ISBN 1860941354
54. MULSER, Peter ; BAUER, Dieter: *Springer Tracts in Modern Physics*. vol. 238: *High Power Laser-Matter Interaction*. Berlin, Heidelberg : Springer Berlin Heidelberg, 2010. – 424 S. – ISBN 978-3-540-50669-0
55. MENZEL, Ralf: *Photonics: linear and nonlinear interactions of laser light and matter*. vol. 24. 1st. Springer Verlag, 2001. – ISBN 3540670742
56. ELIEZER, Shalom: *Interaction of High Power Lasers with Plasmas (Series in Plasma Physics)*. Taylor and Francis, 2001. – 304 S. – ISBN 0750307471
57. JAROSZYNSKI, Dino A. ; BINGHAM, R. ; CAIRNS, R A. ; JAROSZYNSKI, Dino A. (Publ.): *Laser-Plasma Interactions*. Taylor and Francis Group, 2009. – ISBN 1584887788
58. KRUEER, William: *The Physics Of Laser Plasma Interactions (Frontiers in Physics)*. Westview Press, 2003. – 202 S. – ISBN 0813340837
59. GUO, T.: More power to X-rays: New developments in X-ray spectroscopy. in: *Laser & Photonics Review* 3 (2009), November, nr. 6, p. 591–622
60. MOUROU, Gerard ; TAJIMA, Toshiki ; BULANOV, Sergei: Optics in the relativistic regime. in: *Reviews of Modern Physics* 78 (2006), April, nr. 2, p. 309–371
61. ESAREY, E. ; SCHROEDER, C. ; LEEMANS, W.: Physics of laser-driven plasma-based electron accelerators. in: *Reviews of Modern Physics* 81 (2009), August, nr. 3, p. 1229–1285
62. TEUBNER, U. ; GIBBON, P.: High-order harmonics from laser-irradiated plasma surfaces. in: *Reviews of Modern Physics* 81 (2009), nr. 2, p. 445–479. – ISSN 0034–6861
63. TAJIMA, T. ; DAWSON, J.: Laser Electron Accelerator. in: *Physical Review Letters* 43 (1979), July, nr. 4, p. 267–270
64. ROUSSE, Antoine ; PHUOC, Kim ; SHAH, Rahul ; PUKHOV, Alexander ; LEFEBVRE, Eric ; MALKA, Victor ; KISELEV, Sergey ; BURG, Frédéric ; ROUSSEAU, Jean-Philippe ; UMSTADTER, Donald ; HULIN, Danièle: Production of a keV X-Ray Beam from Synchrotron Radiation in Relativistic Laser-Plasma Interaction. in: *Physical Review Letters* 93 (2004), September, nr. 13

65. FAURE, J ; GLINEC, Y ; PUKHOV, A ; KISELEV, S ; GORDIENKO, S ; LEFEBVRE, E ; ROUSSEAU, J-P ; BURGY, F ; MALKA, V: A laser-plasma accelerator producing monoenergetic electron beams. in: *Nature* 431 (2004), September, nr. 7008, p. 541–4
66. SCHLENVOIGT, H.-P. ; HAUPT, K. ; DEBUS, A. ; BUDDE, F. ; JÄCKEL, O. ; PFOTENHAUER, S. ; SCHWOERER, H. ; ROHWER, E. ; GALLACHER, J. G. ; BRUNETTI, E. ; SHANKS, R. P. ; WIGGINS, S. M. ; JAROSZYNSKI, D. A.: A compact synchrotron radiation source driven by a laser-plasma wakefield accelerator. in: *Nature Physics* 4 (2007), December, nr. 2, p. 130–133
67. MALKA, Victor ; FAURE, Jérôme ; GAUDUEL, Yann A. ; LEFEBVRE, Erik ; ROUSSE, Antoine ; PHUOC, Kim T.: Principles and applications of compact laser-plasma accelerators. in: *Nature Physics* 4 (2008), nr. 6, p. 447–453
68. HARTEMANN, FV ; GIBSON, DJ ; BROWN, WJ ; ROUSSE, Antoine ; PHUOC, K. ; MALLKA, V. ; FAURE, J. ; PUKHOV, A.: Compton scattering x-ray sources driven by laser wakefield acceleration. in: *Physical Review Special Topics - Accelerators and Beams* 10 (2007), January, nr. 1
69. SCHWOERER, H. ; LIESFELD, B. ; SCHLENVOIGT, H.-P. ; AMTHOR, K.-U. ; SAUERBREY, R.: Thomson-Backscattered X Rays From Laser-Accelerated Electrons. in: *Physical Review Letters* 96 (2006), nr. 1
70. SCHULZE, K. S. ; KAÄMPFER, T. ; USCHMANN, I. ; HÖFER, S. ; LOETZSCH, R. ; FÖRSTER, E.: Laser-excited acoustical phonons probed by ultrashort pulses from a laser-driven x-ray diode. in: *Applied Physics Letters* 98 (2011), nr. 14, p. 141109
71. EGBERT, A ; CHICHKOV, B. N. ; OSTENDORF, A: Ultrashort X-ray source driven by femtosecond laser pulses. in: *Europhysics Letters (EPL)* 56 (2001), October, nr. 2, p. 228–233
72. SERES, E ; SERES, J ; SPIELMANN, C: Time resolved spectroscopy with femtosecond soft-x-ray pulses. in: *Applied Physics a-Materials Science & Processing* 96 (2009), nr. 1, p. 43–50
73. BRABEC, Thomas ; KRAUSZ, Ferenc: Intense few-cycle laser fields: Frontiers of nonlinear optics. in: *Reviews of Modern Physics* 72 (2000), nr. 2, p. 545–591
74. KRAUSZ, Ferenc ; IVANOV, Misha: Attosecond physics. in: *Reviews of Modern Physics* 81 (2009), nr. 1, p. 163
75. SWOBODA, Marko: *Attosecond Wave Packet Metrology*, Lund University, PhD Thesis, 2010. – Lund Reports on Atomic Physics LRAP-443
76. COMPTON, Arthur: The Spectrum of Scattered X-Rays. in: *Physical Review* 22 (1923), November, nr. 5, p. 409–413
77. GUNST, S B. ; PAGE, L A.: Compton scattering of 2.62-MeV gamma-rays by polarized electrons. in: *Physical Review* 92 (1953), nr. 4, p. 970–973
78. PRIEBE, G. ; LAUNDY, D. ; MACDONALD, M.A. ; DIAKUN, G.P. ; JAMISON, S.P. ; JONES, L.B. ; HOLDER, D.J. ; SMITH, S.L. ; PHILLIPS, P.J. ; FELL, B.D. ; SHEEHY, B. ; NAUMOVA, N. ; SOKOLOV, I.V. ; TER-AVETISYAN, S. ; SPOHR, K. ; KRAFFT, G.A. ; ROSENZWEIG, J.B. ; SCHRAMM, U. ; GRÜNER, F. ; HIRST, G.J. ; COLLIER, J. ; CHATTOPADHYAY, S. ; SEDDON, E.A.: Inverse Compton backscattering source driven by the multi-10 TW laser installed at Daresbury. in: *Laser and Particle Beams* 26 (2008), November, nr. 04, p. 649

79. SCHOENLEIN, R. W. ; LEMMANS, W. P. ; CHIN, A. H. ; VOLFBEYN, P. ; GLOVER, T. E. ; BALLING, P. ; ZOLOTOROV, M. ; KIM, K.-J. ; CHATTOPADHYAY, S. ; SHANK, C. V.: Femtosecond X-ray Pulses at 0.4 Å Generated by 90 Thomson Scattering: A Tool for Probing the Structural Dynamics of Materials. in: *Science* 274 (1996), October, nr. 5285, p. 236–238
80. VOGEL, Helmut ; GERTHSEN, Christian ; MESCHEDE, Dieter (Publ.): *Gerthsen Physik*. Berlin/Heidelberg : Springer-Verlag, 1999 (Springer-Lehrbuch). – ISBN 3–540–25421–8
81. BUCKSBAUM, P. H. ; FREEMAN, R. R. ; BASHKANSKY, M. ; McILRATH, T. J.: Role of the ponderomotive potential in above-threshold ionization. in: *Journal of the Optical Society of America B* 4 (1987), May, nr. 5, p. 760
82. KELDYSH, LV: Ionization in the field of a strong electromagnetic wave. in: *Soviet Physics JETP* 20 (1965), nr. 5, p. 1307–1314
83. MÉZEL, C. ; BOURGEADE, A. ; HALLO, L.: Surface structuring by ultrashort laser pulses: A review of photoionization models. in: *Physics of Plasmas* 17 (2010), nr. 11, p. 113504
84. BOYD, Robert W. (Publ.) ; LUKISHOVA, Svetlana G. (Publ.) ; SHEN, Y.R. (Publ.): *Topics in Applied Physics*. vol. 114: *Self-focusing: Past and Present*. New York, NY : Springer New York, 2009. – ISBN 978–0–387–32147–9
85. DELFIN, C. ; LOKHNYGIN, V. ; MAURITSSON, J. ; SJOEGREN, A. ; WAHLSTROEM, C.-G. ; PUKHOV, A. ; TSAKIRIS, G. D.: Influence of laser pulse duration on relativistic channels. in: *Physics of Plasmas* 9 (2002), nr. 3, p. 937
86. SCHMIDT, Bruno E.: *White Light Filamentation: Tailoring & Application for Charge Reversal of Ag³⁺*, Freie Universitaet Berlin, PhD Thesis, 2008
87. DHARMADHIKARI, Aditya K. ; MATHUR, Deepak ; YAMANOUCHI, Kaoru (Publ.) ; GIULIETTI, Antonio (Publ.) ; LEDINGHAM, Kenneth (Publ.): *Springer Series in Chemical Physics*. vol. 98: *Progress in Ultrafast Intense Laser Science-White light generation and filamentation*. Berlin, Heidelberg : Springer Berlin Heidelberg, 2010. – 81–108 S. – ISBN 978–3–642–03824–2
88. XI, Ting-Ting ; LU, Xin ; ZHANG, Jie: Interaction of Light Filaments Generated by Femtosecond Laser Pulses in Air. in: *Physical Review Letters* 96 (2006), nr. 2, p. 25003
89. WAGNER, N L. ; GIBSON, E A. ; POPMINTCHEV, T ; CHRISTOV, I P. ; MURNANE, M M. ; KAPTEYN, H C.: Self-compression of ultrashort pulses through ionization-induced spatiotemporal reshaping. in: *Physical Review Letters* 93 (2004), nr. 17. ISBN 0031–9007
90. ZHANG, Zhe ; LU, Xin ; LIANG, Wen-Xi ; HAO, Zuo-Qiang ; ZHOU, Mu-Lin ; WANG, Zhao-Hua ; LIU, Xun ; ZHANG, Jie: Triggering and guiding HV discharge in air by filamentation of single and dual fs pulses. in: *Optics Express* 17 (2009), nr. 5, p. 3461–3468
91. GENOUD, Guillaume ; CASSOU, K. ; WOJDA, F. ; FERRARI, H. E. ; KAMPERIDIS, C. ; BURZA, M. ; PERSSON, A. ; UHLIG, J. ; KNEIP, S. ; MANGLES, S. P. D. ; LIFSCHITZ, A. ; CROS, B. ; WAHLSTRÖM, Claes-Göran: Laser-plasma electron acceleration in dielectric capillary tubes. in: *Applied Physics B* (2011)
92. EHRLICH, Y. ; COHEN, C. ; ZIGLER, A. ; KRALL, J. ; SPRANGLE, P. ; ESAREY, E.: Guiding of High Intensity Laser Pulses in Straight and Curved Plasma Channel Experiments. in: *Physical Review Letters* 77 (1996), November, nr. 20, p. 4186–4189

93. COURTOIS, C ; LA FONTAINE, A C. ; LANDOAS, O ; LIDOVE, G ; MEOT, V ; MOREL, P ; NUTER, R ; LEFEBVRE, E ; BOSCHERON, A ; GRENIER, J ; ALEONARD, M M. ; GERBAUX, M ; GOBET, F ; HANNACHI, F ; MALKA, G ; SCHEURER, J N. ; TARISIEN, M: Effect of plasma density scale length on the properties of bremsstrahlung x-ray sources created by picosecond laser pulses. in: *Physics of Plasmas* 16 (2009), nr. 1, p. 13105–13112
94. ANDIEL, U ; EIDMANN, K ; WITTE, K: Time-resolved x-ray K-shell spectra from high density plasmas generated by ultrashort laser pulses. in: *Physical Review E* 63 (2001), January, nr. 2, p. 0–26407
95. ROUSSE, Antoine ; AUDEBERT, P. ; GEINDRE, J. ; FALLIÈS, F. ; GAUTHIER, J. ; MYSYROWICZ, A. ; GRILLON, G. ; ANTONETTI, A.: Efficient $K\alpha$ x-ray source from femtosecond laser-produced plasmas. in: *Physical Review E* 50 (1994), nr. 3, p. 2200–2207
96. STEINGRUBER, J ; BORGSTROM, S ; STARCZEWSKI, T ; LITZEN, U: Prepulse dependence of X-ray emission from plasmas created by IR femtosecond laser pulses on solids. in: *Journal of Physics B-Atomic Molecular and Optical Physics* 29 (1996), nr. 2, p. 0
97. ESTABROOK, Kent ; KRUER, William L.: Properties of Resonantly Heated Electron Distributions. in: *Physical Review Letters* 40 (1978), January, nr. 1, p. 42–45
98. FORSLUND, D. D. ; KINDEL, JM ; LEE, K: Theory of Hot-Electron Spectra at High Laser Intensity. in: *Physical Review Letters* 39 (1977), August, nr. 5, p. 284–288
99. GIBBON, P. ; BELL, A.: Collisionless absorption in sharp-edged plasmas. in: *Physical Review Letters* 68 (1992), March, nr. 10, p. 1535–1538
100. BRUNEL, F: Not-so-resonant, resonant absorption. in: *Physical Review Letters* 59 (1987), July, nr. 1, p. 52–55
101. BRUNEL, F: Anomalous absorption of high intensity subpicosecond laser pulses. in: *Physics of Fluids* 31 (1988), nr. 9, p. 2714
102. GRIMES, M. ; RUNDQUIST, A. ; LEE, Y.-S. ; DOWNER, M.: Experimental Identification of Vacuum Heating at Femtosecond-Laser-Irradiated Metal Surfaces. in: *Physical Review Letters* 82 (1999), May, nr. 20, p. 4010–4013
103. JIANG, Y ; LEE, T ; ROSE-PETRUCK, Christoph G.: Generation of ultrashort hard-x-ray pulses with tabletop laser systems at a 2-kHz repetition rate. in: *Journal of the Optical Society of America B-Optical Physics* 20 (2003), nr. 1, p. 229–237
104. HENKE, B: X-Ray Interactions: Photoabsorption, Scattering, Transmission, and Reflection at $E = 50\text{--}30,000$ eV, $Z = 1\text{--}92$. in: *Atomic Data and Nuclear Data Tables* 54 (1993), July, nr. 2, p. 181–342
105. BERGER, M J. ; COURSEY, J S. ; ZUCKER, M A. ; CHANG, J: *ESTAR: Electron Stopping-Power and Ranges*. <http://physics.nist.gov/PhysRefData/Star/Text/ESTAR.html>. Version: 2005, last checked: 2011-12-02
106. GIBBON, P. ; MAŠEK, M. ; TEUBNER, U. ; LU, W. ; NICOUL, M. ; SHYMANOVICH, U. ; TARASEVITCH, A. ; ZHOU, P. ; SOKOLOWSKI-TINTEN, K. ; LINDE, D.: Modelling and optimisation of fs laser-produced $K\alpha$ sources. in: *Applied Physics A* 96 (2009), March, nr. 1, p. 23–31

107. ZASTRAU, U. ; AUDEBERT, P. ; BERNSTAM, V. ; BRAMBRINK, E. ; KÄMPFER, T. ; KROUPP, E. ; LOETZSCH, R. ; MARON, Y. ; RALCHENKO, Yu. ; REINHOLZ, H. ; RÖPKE, G. ; SENGEBUSCH, A. ; STAMBULCHIK, E. ; USCHMANN, I. ; WEINGARTEN, L. ; FÖRSTER, E.: Temperature and $K\alpha$ -yield radial distributions in laser-produced solid-density plasmas imaged with ultrahigh-resolution x-ray spectroscopy. in: *Physical Review E* 81 (2010), February, nr. 2
108. CHEN, H ; WILKS, Scott C. ; KRUER, William L. ; PATEL, P K. ; SHEPHERD, R: Hot electron energy distributions from ultraintense laser solid interactions. in: *Physics of Plasmas* 16 (2009), nr. 2, p. 020705
109. ANAND, M ; GIBBON, P. ; KRISHNAMURTHY, M: Hot electrons produced from long scale-length laser-produced droplet plasmas. in: *Laser Physics* 17 (2007), nr. 4, p. 408–414
110. GIULIETTI, Antonio ; GAMUCCI, Andrea ; YAMANOUCHI, Kaoru (Publ.) ; GIULIETTI, Antonio (Publ.) ; LEDINGHAM, Kenneth (Publ.): *Springer Series in Chemical Physics*. vol. 98: *Progress in Ultrafast Intense Laser Science-Propagation of high intensity laser pulses in plasma*. Berlin, Heidelberg : Springer Berlin Heidelberg, 2010. – 139–163 S. – ISBN 978–3–642–03824–2
111. WILKS, Scott C. ; KRUER, William L.: Absorption of ultrashort, ultra-intense laser light by solids and overdense plasmas. in: *Ieee Journal of Quantum Electronics* 33 (1997), nr. 11, p. 1954–1968
112. RETTIG, C. L. ; ROQUEMORE, W. M. ; GORD, J. R.: Efficiency and scaling of an ultrashort-pulse high-repetition-rate laser-driven X-ray source. in: *Applied Physics B* 93 (2008), August, nr. 2-3, p. 365–372
113. THOSS, Andreas: *X-ray Emission and Particle Acceleration from a Liquid Jet Target Using a 1-kHz Ultrafast Laser System*, PhD Thesis, 2003.
<http://www.diss.fu-berlin.de/2003/240/thoss.pdf>
114. MURNANE, M M. ; KAPTEYN, H C. ; ROSEN, M D. ; FALCONE, R W.: Ultrafast X-ray Pulses from Laser-Produced Plasmas. in: *Science (New York, N.Y.)* 251 (1991), February, nr. 4993, p. 531–6
115. TEUBNER, U ; GIBBON, P. ; ALTENBERND, D ; OBERSCHMIDT, D ; FORSTER, E ; MYSYROWICZ, A ; AUDEBERT, P ; GEINDRE, J P. ; GAUTHIER, J C.: Plasma frequency and harmonic emission from fs-laser plasmas. in: *Laser and Particle Beams* 17 (1999), nr. 4, p. 613–619
116. ZIENER, C ; USCHMANN, I ; STOBRAWA, G ; REICH, C ; GIBBON, P ; FEURER, T ; MORAK, A ; DUSTERER, S ; SCHWOERER, H ; FORSTER, E ; SAUERBREY, R: Optimization of K alpha bursts for photon energies between 1.7 and 7 keV produced by femtosecond-laser-produced plasmas of different scale length. in: *Physical Review E* 65 (2002), nr. 6
117. SJÖGREN, Anders ; HARBST, M ; WAHLSTRÖM, C.-G. ; SVANBERG, S ; OLSSON, C: High-repetition-rate, hard x-ray radiation from a laser-produced plasma: Photon yield and application considerations. in: *Review of Scientific Instruments* 74 (2003), nr. 4, p. 2300
118. HAGEDORN, M. ; KUTZNER, J. ; TSILIMIS, G. ; ZACHARIAS, H.: High-repetition-rate hard X-ray generation with sub-millijoule femtosecond laser pulses. in: *Applied Physics B: Lasers and Optics* 77 (2003), August, nr. 1, p. 49–57
119. HOU, B. ; NEES, J. ; MORDOVANAKIS, A. ; WILCOX, M. ; MOUROU, G. ; CHEN, L.M. ; KIEFFER, J.-C. ; CHAMBERLAIN, C.C. ; KROL, A.: Hard X-ray generation from solids driven by relativistic intensity in the lambda-cubed regime. in: *Applied Physics B* 83 (2006), January, nr. 1, p. 81–85

120. DORCHIES, F. ; HARMAND, M. ; DESCAMPS, D. ; FOURMENT, C. ; HULIN, S. ; PETIT, S. ; PEYRUSSE, O. ; SANTOS, J. J.: High-power 1 kHz laser-plasma x-ray source for ultrafast x-ray absorption near-edge spectroscopy in the keV range. in: *Applied Physics Letters* 93 (2008), nr. 12, p. 121113
121. ZHAVORONKOV, Nickolai ; GRITSAI, Yuri ; BARGHEER, Matias ; WOERNER, Michael ; ELSAESSER, Thomas ; ZAMPONI, Flavio ; USCHMANN, Ingo ; FÖRSTER, Eckhart: Microfocus Cu K α source for femtosecond x-ray science. in: *Optics Letters* 30 (2005), nr. 13, p. 1737
122. ZAMPONI, F. ; ANSARI, Z. ; WOERNER, M. ; ELSAESSER, Thomas: Femtosecond powder diffraction with a laser-driven hard X-ray source. in: *Optics Express* 18 (2010), January, nr. 2, p. 947
123. ROSE-PETRUCK, Christoph ; JIMENEZ, Ralph ; GUO, Ting ; CAVALLERI, Andrea ; SIDERS, Craig W. ; RKSÍ, Ferenc ; SQUIER, Jeff A. ; WALKER, Barry C. ; WILSON, Kent R. ; BARTY, Christopher P. J.: Picosecond-milliångström lattice dynamics measured by ultrafast X-ray diffraction. in: *Nature* 398 (1999), March, nr. 6725, p. 310–312
124. CHEN, J ; ZHANG, H ; TOMOV, I V. ; WOLFSHERG, M ; DING, X L. ; RENTZEPIS, P.M.: Transient structures and kinetics of the ferrioxalate redox reaction studied by time-resolved EXAFS, optical spectroscopy, and DFT. in: *Journal of Physical Chemistry A* 111 (2007), nr. 38, p. 9326–9335
125. BECK, Michael: *Characterisation of an XUV laser driven plasma source and its application to NEXAFS-spectroscopy of organic molecules*, Technische Uni Berlin, PhD Thesis, 2002.
<http://opus.kobv.de/tuberlin/volltexte/2002/396/>
126. VOGT, Ulrich ; WILHEIN, Thomas ; STIEL, Holger ; LEGALL, Herbert: High resolution x-ray absorption spectroscopy using a laser plasma radiation source. in: *Review of Scientific Instruments* 75 (2004), nr. 11, p. 4606
127. LARSSON, J ; SJÖGREN, Anders: Evaluation of laser-irradiated Ar clusters as a source for time-resolved x-ray studies. in: *Review of Scientific Instruments* 70 (1999), nr. 5, p. 2253
128. ISSAC, R. ; WIRTHIG, J. ; BRUNETTI, E. ; VIEUX, G. ; ERSFELD, B. ; JAMISON, S.P. ; JONES, D. ; BINGHAM, R. ; CLARK, D. ; JAROSZYNSKI, D.A.: Bright source of K[math>\alpha] and continuum X rays by heating Kr clusters using a femtosecond laser. in: *Laser and Particle Beams* 21 (2004), March, nr. 04
129. DORCHIES, F: *Ultra short x-ray source from laser-clusters interaction*. vol. 5975. SPIE, 2006. – 597501–597501–6 S. – ISBN 0277–786X
130. CHAKRAVARTY, U. ; NAIK, P.A. ; KUMBHARE, S.R. ; GUPTA, P.D.: Efficient keV X-ray Generation from Irradiation of in-situ Produced Silver Clusters by Ti:sapphire Laser Pulses. in: *Journal of the Optical Society of Korea* 13 (2009), March, nr. 1, p. 80–85
131. RYMELL, L ; HERTZ, H: Droplet target for low-debris laser-plasma soft X-ray generation. in: *Optics Communications* 103 (1993), November, nr. 1-2, p. 105–110
132. ANAND, M ; SAFVAN, C P. ; KRISHNAMURTHY, M: Hard X-ray generation from microdroplets in intense laser fields. in: *Applied Physics B-Lasers and Optics* 81 (2005), nr. 4, p. 469–477
133. KUGLAND, N. L. ; CONSTANTIN, C. G. ; NEUMAYER, P. ; CHUNG, H.-K. ; COLLETTE, A. ; DEWALD, E. L. ; FROULA, D. H. ; GLENZER, S. H. ; KEMP, A. ; KRITCHER, A. L. ; ROSS, J. S. ; NIEMANN, C.: High K α x-ray conversion efficiency from extended source gas jet targets irradiated by ultra short laser pulses. in: *Applied Physics Letters* 92 (2008), nr. 24, p. 241504

134. THOSS, Andreas ; RICHARDSON, M ; KORN, G ; FAUBEL, M ; STIEL, H ; VOGT, U ; ELSAESSER, Thomas: KiloHertz sources of hard x rays and fast ions with femtosecond laser plasmas. in: *Journal of the Optical Society of America B* 20 (2003), nr. 1, p. 224–228
135. TOMPKINS, R J. ; MERCER, I P. ; FETTWEIS, M ; BARNETT, C J. ; KLUG, D R. ; PORTER, L G. ; CLARK, I ; JACKSON, S ; MATOUSEK, P ; PARKER, A W. ; TOWRIE, M: 5-20 keV laser-induced x-ray generation at 1 kHz from a liquid-jet target. in: *Review of Scientific Instruments* 69 (1998), nr. 9, p. 3113–3117
136. VOGT, Ulrich: Scaling-up a liquid water jet laser plasma source to high average power for extreme-ultraviolet lithography. in: *Proceedings of SPIE* vol. 4343, SPIE, 2001, p. 535–542
137. KORN, Georg ; THOSS, Andreas ; STIEL, Holger ; VOGT, Ullrich ; RICHARDSON, Martin ; FAUBEL, Manfred ; ELSAESSER, *Thomas: Ultrashort 1-kHz laser plasma hard x-ray source. in: *Optics Letters* 27 (2002), May, nr. 10, p. 866
138. LI, Y. ; ZHANG, J. ; SHENG, Z. ; TENG, H. ; LIANG, T. ; PENG, X. ; LU, X. ; TANG, X.: Spatial Distribution of High-Energy Electron Emission from Water Plasmas Produced by Femtosecond Laser Pulses. in: *Physical Review Letters* 90 (2003), April, nr. 16
139. HANSSON, B A M. ; BERGLUND, M ; HEMBERG, O ; HERTZ, Hans M.: Stabilization of liquified-inert-gas jets for laser-plasma generation. in: *Journal of Applied Physics* 95 (2004), nr. 8, p. 4432–4437
140. HATANAKA, K ; MIURA, T ; FUKUMURA, H: White X-ray pulse emission of alkali halide aqueous solutions irradiated by focused femtosecond laser pulses: a spectroscopic study on electron temperatures as functions of laser intensity, solute concentration, and solute atomic number. in: *Chemical Physics* 299 (2004), April, nr. 2-3, p. 265–270. ISBN 0301-0104
141. REICH, Christian ; LAPERLE, Christopher M. ; LI, Xiaodi ; AHR, Brian ; BENESCH, Frank ; ROSE-PETRUCK, Christoph G.: Ultrafast x-ray pulses emitted from a liquid mercury laser target. in: *Optics Letters* 32 (2007), nr. 4, p. 427
142. SHAN, Fang ; GUO, Ting: Ultrafast selected energy x-ray absorption spectroscopy investigations of Ni and Zn species. in: *The Journal of chemical physics* 122 (2005), June, nr. 24, p. 244710
143. CHENG, Guangjun ; SHAN, Fang ; FREYER, A ; GUO, Ting: Ultrafast x-ray absorption spectroscopy using laser-driven electron x-ray sources (LEXS). in: *Proceedings of SPIE* vol. 4504, SPIE, 2001, p. 1–7
144. FOURMAUX, S ; LECHERBOURG, L ; HARMAND, M ; SERVOL, M ; KIEFFER, J C.: High repetition rate laser produced soft x-ray source for ultrafast x-ray absorption near edge structure measurements. in: *The Review of scientific instruments* 78 (2007), November, nr. 11, p. 113104
145. EASON, R W. ; BRADLEY, D K. ; KILKENNY, J D. ; GREAVES, G N.: Improved laser-EXAFS studies of aluminium foil. in: *Journal of Physics C: Solid State Physics* 17 (1984), October, nr. 28
146. TOMOV, I: Ultrafast X-ray determination of transient structures in solids and liquids. in: *Chemical Physics* 299 (2004), April, nr. 2-3, p. 203–213
147. TOMOV, Ivan V. ; RENTZEPIS, Peter M.: Ultrafast time-resolved transient structures of solids and liquids by means of extended X-ray absorption fine structure. in: *Chemphyschem : a European journal of chemical physics and physical chemistry* 5 (2004), January, nr. 1, p. 27–35

148. RÁKSI, Ferenc ; WILSON, Kent R. ; JIANG, Zhiming ; IKHLEF, Abdelaziz ; CÔTÉ, Christian Y. ; KIEFFER, Jean-Claude: Ultrafast x-ray absorption probing of a chemical reaction. in: *The Journal of Chemical Physics* 104 (1996), nr. 15, p. 6066
149. OULIANOV, D A.: Structures of bromoalkanes' photodissociation in solution by means of ultrafast extended x-ray absorption fine-structure spectroscopy. in: *Proceedings of the National Academy of Sciences* 99 (2002), September, nr. 20, p. 12556–12561
150. LEE, T ; JIANG, Y ; ROSE-PETRUCK, C G. ; BENESCH, F: Ultrafast tabletop laser-pump-x-ray probe measurement of solvated Fe(CN)(6)(4-). in: *Journal of Chemical Physics* 122 (2005), nr. 8, p. 084506
151. BENESCH, Frank ; LEE, Taewoo ; JIANG, Yan ; ROSE-PETRUCK, Christoph G.: Ultrafast laser-driven x-ray spectrometer for x-ray absorption spectroscopy of transition metal complexes. in: *Optics Letters* 29 (2004), nr. 9, p. 1028
152. FOURMENT, C ; ARAZAM, N ; BONTE, C ; CAILLAUD, T ; DESCAMPS, D ; DORCHIES, F ; HARMAND, M ; HULIN, S ; PETIT, S ; SANTOS, J J.: Broadband, high dynamics and high resolution charge coupled device-based spectrometer in dynamic mode for multi-keV repetitive x-ray sources. in: *The Review of scientific instruments* 80 (2009), nr. 8, p. 083505
153. EGGERS, J ; VILLERMAUX, E: Physics of liquid jets. in: *Reports on Progress in Physics* 71 (2008), nr. 3, p. 036601
154. STRONG, John: *Procedures in Experimental Physics*. Lindsay Pubns, 1986. – 642 S. – ISBN 0917914562
155. POLLARD, Alan Faraday C.: *The kinematical design of couplings in instrument mechanisms*. Hilger Division, Hilger & Watts, 1951
156. FURSE, J E.: Kinematic design of fine mechanisms in instruments. in: *Journal of Physics E: Scientific Instruments* 14 (1981), March, nr. 3, p. 264–272
157. VIG, Asger L.: *Pinched Flow Fractionation - Technology and Application*, Technical University of Denmark, PhD Thesis, 2010
158. SERGEY, Stephanov: *TER_sl online tool from Stephanovs X-ray server*. http://sergey.gmca.aps.anl.gov/TER_sl.html#TER_sl, last checked: 2011.10.14
159. WARREN, B E.: *X-Ray Diffraction*. Dover Publications, 1990. – ISBN 0-486-66317-5
160. ERKO, A ; IDIR, M ; KRIST, T ; MICHETTE, AG: *Springer Series in optical science*. vol. 137: *Modern Developments in X-Ray and Neutron Optics*. Berlin, Heidelberg : Springer Berlin Heidelberg, 2008. – ISBN 978-3-540-74560-0
161. EWALD, P. P.: The so-called correction of Bragg's law. in: *Acta Crystallographica Section A Foundations of Crystallography* 42 (1986), November, nr. 6, p. 411–413
162. CHANTLER, C.T ; OLSEN, K. ; DRAGOSET, R.A. ; KISHORE, A.R. ; KOTOCHIGOVA, S.A. ; ZUCKER, D.S.: *X-Ray Form Factor, Attenuation and Scattering Tables*. <http://www.nist.gov/pml/data/ffast/index.cfm>, last checked: 2011-12-12
163. UHLIG, Jens ; FULLAGAR, Wilfred K. ; SVENSSON, C. ; CERENIUS, Y: Microfocus Tube Source Recommissioning. in: *Maxlab Activity Report*, 2006, p. 343–343

164. *Use of a Kumakhov lens in analytic instruments*. 1996. – US patent no. 5497008 filed 1995
165. SCHIELDS, Paul J. ; GIBSON, David M. ; GIBSON, Walter M. ; GAO, Ning ; HUANG, Huapeng ; PONOMAREV, Igor Y.: Overview of polycapillary X-ray optics. in: *Powder Diffraction* 17 (2002), nr. 2, p. 70
166. PUTKUNZ, Corey T. ; PEELE, Andrew G.: Detailed simulation of a Lobster-eye telescope. in: *Optics Express* 17 (2009), July, nr. 16, p. 14156
167. KIRKPATRICK, Paul ; BAEZ, A. V.: Formation of Optical Images by X-Rays. in: *Journal of the Optical Society of America* 38 (1948), September, nr. 9, p. 766
168. BUNKER, Grant: *Introduction to XAFS-A practical guide to X-ray absorption fine structure Spectroscopy*. Illinois Institute of Technology, 2010. – ISBN 978-0521767750
169. BARGHEER, M. ; ZHAVORONKOV, N. ; BRUCH, R. ; LEGALL, H. ; STIEL, H. ; WOERNER, M. ; ELSAESSER, T.: Comparison of focusing optics for femtosecond X-ray diffraction. in: *Applied Physics B* 80 (2005), April, nr. 6, p. 715–719
170. BROGLIE, Louis D.: The wave nature of the electron. in: *Nobel lecture 12 December 1929., 1929*
171. BERGER, M.J. ; HUBBELL, J.H. ; SELTZER, S.M. ; CHANG, J. ; COURSEY, J.S. ; SUKUMAR, R. ; ZUCKER, D.S. ; OLSEN, K.: *NIST XCOM: Photon Cross Sections Database*. <http://www.nist.gov/pml/data/xcom/index.cfm>. Version: 2010, last checked: 18/11/11
172. LAMBERT, I.H.: Lambert law of absorption. Version: 1760. <http://imgbase-scd-ulp.u-strasbg.fr/displayimage.php?pos=-16594>. in: *Photometria sive de mensura et gradibus luminis, colorum et umbrae*. Eberhardt Klett, Germany, 1760, chapter 5, 391
173. BEER, August: Bestimmung der Absorption des rothen Lichts in farbigen Flüssigkeiten. in: *Annalen der Physik und Chemie* 86 (1852), p. 78–88
174. LANDAU, Lew D. ; LIFSCHITZ, Ewgeni M. ; ZIESCHE, Paul. (Publ.): *Quantenmechanik, Lehrbuch der theoretischen Physik, 10 Bde..* vol. 3. reprint 9th edition. Deutsch (Harri), 1992. – 142–152 S. – ISBN 3817113285
175. REHR, J J. ; ALBERS, R C.: Theoretical approaches to x-ray absorption fine structure. in: *Reviews of Modern Physics* 72 (2000), nr. 3, p. 621–654
176. NEWVILLE, Matthew: Fundamentals of XAFS. in: *Consortium for Advanced Radiation Sources, University of Chicago (USA)*[<http://xafs.org>] (2004). <http://streaming.lehigh.edu/rm/dept/IMI/VirtualGlassCourse/SuppReading/Tutorials.pdf>
177. KRAUSE, M. O. ; OLIVER, J. H.: Natural widths of atomic K and L levels, $K\alpha$ X-ray lines and several KLL Auger lines. in: *Journal of Physical and Chemical Reference Data* 8 (1979), nr. 2, p. 329
178. BERGMANN, Uwe ; GLATZEL, Pieter: X-ray emission spectroscopy. in: *Photosynthesis research* (2009), August
179. BROWN, Frank L. H. ; WILSON, Kent R. ; CAO, Jianshu: Ultrafast extended x-ray absorption fine structure (EXAFS)-theoretical considerations. in: *The Journal of Chemical Physics* 111 (1999), nr. 14, p. 6238
180. GROOT, Frank de ; VANKÓ, György ; GLATZEL, Pieter: The 1s x-ray absorption pre-edge structures in transition metal oxides. in: *Journal of Physics: Condensed Matter* 21 (2009), March, nr. 10, p. 104207

181. YANO, Junko ; YACHANDRA, Vittal K.: X-ray absorption spectroscopy. in: *Photosynthesis research* 102, nr. 2-3, p. 241–54
182. STÖHR, Joachim: *NEXAFS Spectroscopy (Springer Series in Surface Sciences)*. Springer, 1992. – ISBN 3540544224
183. GLATZEL, Pieter ; BERGMANN, U: High resolution 1s core hole X-ray spectroscopy in 3d transition metal complexes: electronic and structural information. in: *Coordination Chemistry Reviews* 249 (2005), January, nr. 1-2, p. 65–95
184. GROOT, Frank de: Multiplet effects in X-ray spectroscopy. in: *Coordination Chemistry Reviews* 249 (2005), January, nr. 1-2, p. 31–63
185. HENNIES, Franz ; PIETZSCH, Annette ; BERGLUND, Martin ; FÖHLISCH, Alexander ; SCHMITT, Thorsten ; STROCOV, Vladimir ; KARLSSON, Hans O. ; ANDERSSON, Joakim ; RUBENSSON, Jan-Erik: Resonant Inelastic Scattering Spectra of Free Molecules with Vibrational Resolution. in: *Physical Review Letters* 104 (2010), May, nr. 19
186. SCHWALBE, Matthias: *Heterosupramolekulare Oligometallkatalysatoren: Synthese und Reaktivitätssteuerung durch Photoelektronentransfer*, Friedrich Schiller Universitaet Jena, PhD Thesis, 2007
187. LEI, Pengxiang ; HEDLUND, Maria ; LOMOTH, Reiner ; RENSMO, Hå k. ; JOHANSSON, Olof ; HAMMARSTRÖM, Leif: The role of colloid formation in the photoinduced H₂ production with a Ru(II)-Pd(II) supramolecular complex: a study by GC, XPS, and TEM. in: *Journal of the American Chemical Society* 130 (2008), January, nr. 1, p. 26–7
188. OZAWA, Hironobu ; HAGA, Masa-aki ; SAKAI, Ken: A photo-hydrogen-evolving molecular device driving visible-light-induced EDTA-reduction of water into molecular hydrogen. in: *Journal of the American Chemical Society* 128 (2006), April, nr. 15, p. 4926–7
189. SMOLENTSEV, G. ; UHLIG, J. ; NAZARENKO, E. ; M., Pfeffer ; B., Dietzek ; RAU, S.: *working title: Evolution of Ru-Pt and Ru-Pd catalysts upon optical excitation*. Manuscript in preparation,
190. TSCHIERLEI, Stefanie ; PRESSELT, Martin ; KUHN, Christian ; YARTSEV, Arkady ; PASCHER, Torbjörn ; SUNDSTRÖM, Villy ; KARNAHL, Michael ; SCHWALBE, Matthias ; SCHÄFER, Bernhard ; RAU, Sven ; SCHMITT, Michael ; DIETZEK, Benjamin ; POPP, Jürgen: Photophysics of an intramolecular hydrogen-evolving Ru-Pd photocatalyst. in: *Chemistry (Weinheim an der Bergstrasse, Germany)* 15 (2009), August, nr. 31, p. 7678–88. – ISSN 1521–3765
191. MAGNUSON, Ann ; ANDERLUND, Magnus ; JOHANSSON, Olof ; LINDBLAD, Peter ; LOMOTH, Reiner ; POLIVKA, Tomas ; OTT, Sascha ; STENSJÖ, Karin ; STYRING, Stenbjörn ; SUNDSTRÖM, Villy ; HAMMARSTRÖM, Leif: Biomimetic and microbial approaches to solar fuel generation. in: *Accounts of chemical research* 42 (2009), December, nr. 12, p. 1899–909
192. GORDON, John C. ; KUBAS, Gregory J.: Perspectives on How Nature Employs the Principles of Organometallic Chemistry in Dihydrogen Activation in Hydrogenases . in: *Organometallics* 29 (2010), November, nr. 21, p. 4682–4701
193. CHEN, Lin X. ; ZHANG, Xiaoyi ; LOCKARD, Jenny V. ; STICKRATH, Andrew B. ; ATTENKOFER, Klaus ; JENNINGS, Guy ; LIU, Di-Jia: Excited-state molecular structures captured by X-ray transient absorption spectroscopy: a decade and beyond. in: *Acta crystallographica. Section A, Foundations of crystallography* 66 (2010), March, nr. Pt 2, p. 240–51

194. JOHNSON, S.L. ; MILNE, C.J.: Ultrafast X-ray science: structural transients in solution. in: *TrAC Trends in Analytical Chemistry* 29 (2010), June, nr. 6, p. 497–507
195. GAWELDA, Wojciech: *Time-resolved x-ray absorption spectroscopy of transition metal complexes*, École Polytechnique Fédérale de Lausanne, PhD Thesis, 2006
196. MATERIALS, Exafs: *EXAFS materials reference spectra*. <http://exafsmaterials.com/ReferenceSpectra.html>, last checked: 18/12/12
197. ABSORPTION SOCIETY, International X.: *IXAS database*. <http://ixs.iit.edu/database/>, last checked: 18/12/11
198. *With friendly permission from Wilfred Fullagar*. 2011
199. PONCHUT, Cyril: Characterization of X-ray area detectors for synchrotron beamlines. in: *Journal of synchrotron radiation* 13 (2006), March, nr. Pt 2, p. 195–203
200. HOWE, J. ; CHAMBERS, D. M. ; COURTOIS, C. ; FÖRSTER, E. ; GREGORY, C. D. ; HALL, I. M. ; RENNER, O. ; USCHMANN, I. ; WOOLSEY, N. C.: Comparison of film detectors, charged-coupled devices, and imaging plates in x-ray spectroscopy of hot dense plasma. in: *Review of Scientific Instruments* 77 (2006), nr. 3, p. 036105
201. HALL, C: 2D detectors for synchrotron X-ray sources, some comparative tests. in: *Nuclear Instruments and Methods in Physics Research Section A: Accelerators, Spectrometers, Detectors and Associated Equipment* 310 (1991), nr. 1-2, p. 215–219
202. HALL, C. J. ; LEWIS, R. A. ; PARKER, B. ; WORGAN, J. S.: The secret life of image plate phosphors. in: *Review of Scientific Instruments* 63 (1992), nr. 1, p. 697
203. KIM, Yong-Ki ; RUDD, M.: Binary-encounter-dipole model for electron-impact ionization. in: *Physical Review A* 50 (1994), November, nr. 5, p. 3954–3967
204. CARRON, N: *An introduction to the passage of energetic particles through matter*. Boca Raton : Taylor & Francis, 2007. – ISBN 9780750309356
205. FANO, U.: On the Theory of Ionization Yield of Radiations in Different Substances. in: *Physical Review* 70 (1946), July, nr. 1-2, p. 44–52
206. TUNG, C. ; ASHLEY, J. ; RITCHIE, R.: Electron inelastic mean free paths and energy losses in solids II: Electron gas statistical model. in: *Surface Science* 81 (1979), March, nr. 2, p. 427–439
207. VAVILOV, V: On photo-ionization by fast electrons in germanium and silicon. in: *Journal of Physics and Chemistry of Solids* 8 (1959), January, p. 223–226
208. BICHSEL, Hans: Straggling in thin silicon detectors. in: *Reviews of Modern Physics* 60 (1988), July, nr. 3, p. 663–699
209. BARENDS, R. ; BASELMANS, J. J. A. ; YATES, S. J. C. ; GAO, J. R. ; HOVENIER, J. N. ; KLAPWIJK, T. M.: Quasiparticle Relaxation in Optically Excited High-Q Superconducting Resonators. in: *Physical Review Letters* 100 (2008), June, nr. 25
210. TIMOFEEV, A. ; GARCÍA, C. ; KOPNIN, N. ; SAVIN, A. ; MESCHKE, M. ; GIAZOTTO, F. ; PEKOLA, J.: Recombination-Limited Energy Relaxation in a Bardeen-Cooper-Schrieffer Superconductor. in: *Physical Review Letters* 102 (2009), January, nr. 1

211. KOZOREZOV, A. ; WIGMORE, J. ; MARTIN, D. ; VERHOEVE, P. ; PEACOCK, A.: Electron energy down-conversion in thin superconducting films. in: *Physical Review B* 75 (2007), March, nr. 9
212. KOZOREZOV, A. ; PEPE, G. ; GOLUBOV, A. ; MARTIN, D. ; WIGMORE, J. K.: Thermalisation in metals on a sub-picosecond time scale, American Institute of Physics (AIP), 2009, 298–301
213. KOZOREZOV, A.: Energy down-conversion and thermalization in metal absorbers. in: *To be published as special issue in in the Journal of Low Temperature Physics*, 2011
214. FANO, U: Ionization Yield of Radiations. II. The Fluctuations of the Number of Ions. in: *Physical Review* 72 (1947), July, nr. 1, p. 26–29
215. ROOSBROECK, W. van: Theory of the Yield and Fano Factor of Electron-Hole Pairs Generated in Semiconductors by High-Energy Particles. in: *Physical Review* 139 (1965), August, nr. 5A, p. A1702–A1716
216. MAZZIOTTA, M.: Electron-hole pair creation energy and Fano factor temperature dependence in silicon. in: *Nuclear Instruments and Methods in Physics Research Section A: Accelerators, Spectrometers, Detectors and Associated Equipment* 584 (2008), January, nr. 2-3, p. 436–439
217. FRASER, G. ; ABBEY, A. ; HOLLAND, A. ; MCCARTHY, K. ; OWENS, A ; WELLS, A: The X-ray energy response of silicon Part A. Theory. in: *Nuclear Instruments and Methods in Physics Research Section A: Accelerators, Spectrometers, Detectors and Associated Equipment* 350 (1994), October, nr. 1-2, p. 368–378
218. HARRISON, M. ; MCGREGOR, D. ; DOTY, F.: Fano factor and nonuniformities affecting charge transport in semiconductors. in: *Physical Review B* 77 (2008), May, nr. 19
219. JANESICK, James: *Scientific charge-coupled devices*. Bellingham, Wash : SPIE Press, 2001. – ISBN 0819436984
220. ROBBINS, M S. ; HADWEN, B J.: The noise performance of electron multiplying charge-coupled devices. in: *Ieee Transactions on Electron Devices* 50 (2003), p. 1227–1232
221. INC e2v: *e2v datasheet L3C216 electron multiplying CCD*, <http://www.e2v.com/products-and-services/high-performance-imaging-solutions/datasheets/ccd-selector/>, last checked: 2011-11-22
222. LIMA, Frederico A. ; MILNE, Christopher J. ; AMARASINGHE, Dimali C V. ; RITTMANN-FRANK, Mercedes H. ; VEEN, Renske M. d. ; REINHARD, Marco ; PHAM, Van-Thai ; KARLSSON, Susanne ; JOHNSON, Steven L. ; GROLIMUND, Daniel ; BORCA, Camelia ; HUTHWELKER, Thomas ; JANOUSCH, Markus ; MOURIK, Frank van ; ABELA, Rafael ; CHERGUL, Majed: A high-repetition rate scheme for synchrotron-based picosecond laser pump/x-ray probe experiments on chemical and biological systems in solution. in: *The Review of scientific instruments* 82 (2011), June, nr. 6, p. 063111
223. LUTZ, G: Silicon drift and pixel devices for X-ray imaging and spectroscopy. in: *Journal of synchrotron radiation* 13 (2006), March, nr. Pt 2, p. 99–109
224. OWENS, Alan: Semiconductor materials and radiation detection. in: *Journal of synchrotron radiation* 13 (2006), March, nr. 2, p. 143–50
225. AHMED, Syed: *Physics and engineering of radiation detection*. San Diego London : Academic Press, 2007. – ISBN 0120455811

226. RICHMOND, Michael: *Modified from: Introduction to CCDs*.
<http://spiff.rit.edu/classes/phys445/lectures/ccd1/ccd1.html>, last checked: 2011-12-03
227. INC e2v: *e2v datasheet 30-11 deep depletion front illuminated CCD AIMO*,
<http://www.e2v.com/products-and-services/high-performance-imaging-solutions/datasheets/ccd-selector/>, last checked: 2011-11-22
228. HOLLAND, S.E. ; GROOM, D.E. ; PALAIO, N.P. ; STOVER, R.J.: Fully depleted, back-illuminated charge-coupled devices fabricated on high-resistivity silicon. in: *IEEE Transactions on Electron Devices* 50 (2003), January, nr. 1, p. 225–238
229. BURKE, Barry ; JORDEN, Paul ; VU, Paul: CCD Technology. in: *Experimental Astronomy* 19 (2005), nr. 1-3, p. 69–102
230. HOLST, Gerald: *CMOS/CCD sensors and camera systems*. Winter Park, FL Bellingham, Wash : JCD Pub. SPIE, 2007. – ISBN 0819467308
231. INC. e2v ; BROWN, P.: *technical support*. – Private communication
232. PAVLOV, G. ; NOUSEK, J.: Charge diffusion in CCD X-ray detectors. in: *Nuclear Instruments and Methods in Physics Research Section A: Accelerators, Spectrometers, Detectors and Associated Equipment* 428 (1999), nr. 2-3, p. 348–366
233. BAUTZ, M: X-ray CCD response functions, front to back. in: *Nuclear Instruments and Methods in Physics Research Section A: Accelerators, Spectrometers, Detectors and Associated Equipment* 436 (1999), nr. 1-2, p. 40–52
234. PRIGOZHIN, G. ; BUTLER, N.R. ; KISSEL, S.E. ; RICKER, G.R.: An experimental study of charge diffusion in the undepleted silicon of X-ray CCDs. in: *IEEE Transactions on Electron Devices* 50 (2003), nr. 1, p. 246–253
235. PRIGOZHIN, Gregory Y.: X-ray absorption near edge structure in the quantum efficiency of x-ray charge-coupled devices. in: *Optical Engineering* 37 (1998), nr. 10, p. 2848
236. HOFFMAN, Alan ; LOOSE, Markus ; SUNTHARALINGAM, Vyshnavi: CMOS Detector Technology. in: *Experimental Astronomy* 19 (2006), nr. 1-3, p. 111–134
237. ROGALSKI, Antoni: Infrared detectors: status and trends. in: *Progress in Quantum Electronics* 27 (2003), January, nr. 2-3, p. 59–210
238. DECTRIS Ltd. <http://www.dectris.com/sites/products.html>, last checked: 2011-11-24
239. EJDURUP, T ; LEMKE, H T. ; HALDRUP, K ; NIELSEN, T N. ; ARMS, D A. ; WALKO, D A. ; MICELI, A ; LANDAHL, E C. ; DUFRESNE, E M. ; NIELSEN, M M.: Picosecond time-resolved laser pump/X-ray probe experiments using a gated single-photon-counting area detector. in: *Journal of synchrotron radiation* 16 (2009), p. 387–90
240. KLEYMENOV, Evgeny ; BOKHOVEN, Jeroen A. ; DAVID, Christian ; GLATZEL, Pieter ; JANOUSCH, Markus ; ALONSO-MORI, Roberto ; STUDER, Marco ; WILLIMANN, Markus ; BERGAMASCHI, Anna ; HENRICH, Beat ; NACHTEGAAL, Maarten: Five-element Johann-type x-ray emission spectrometer with a single-photon-counting pixel detector. in: *The Review of scientific instruments* 82 (2011), June, nr. 6, p. 065107

-
241. INC., Intevac: *MicroVista Back illuminated CMOS*. online. <http://www.intevac.com/uploads/datasheets/MicroVistaNIR.pdf>. Version: 2011, last checked: 2011-11-24. – data sheet
242. INC., Intevac ; TRUE, Bruce: *back illuminated and back thinned CMOS build for near infrared*. – Private communication
243. SOLEIL, Synchrotron: *XPAD*. <http://www.synchrotron-soleil.fr/images/File/instrumentation/XPAD/ArticlesRS/XPAD.pdf>. Version: 2011, last checked: 2011-11-24
244. HUSTACHE-OTTINI, S. ; BÉRAR, J.-F. ; BOUDET, N. ; BASOLO, S. ; BORDESSOULE, M. ; BREUGNON, P. ; CAILLOT, B. ; CLEMENS, J.-C. ; DELPIERRE, P. ; DINKESPILER, B. ; KOUDOUBINE, I. ; MEDJOUBI, K. ; MEESSEN, C. ; MENOUNI, M. ; MOREL, C. ; PANGAUD, P. ; VIGEOLAS, E.: The Hybrid Pixel Single Photon Counting Detector XPAD. in: *AIP Conference Proceedings* vol. 879, AIP, 2007, p. 1087–1090
245. MEDJOUBI, K ; HUSTACHE, S ; PICCA, F ; BÉRAR, J F. ; BOUDET, N ; BOMPARD, F ; BREUGNON, P ; CLÉMENS, J C. ; DAWIEC, A ; DELPIERRE, P ; DINKESPILER, B ; GODIOT, S ; LOGIER, J P. ; MENOUNI, M ; MOREL, C ; NICOLAS, M ; PANGAUD, P ; VIGEOLAS, E: Performance and Applications of the CdTe- and Si-XPAD3 photon counting 2D detector. in: *Journal of Instrumentation* 6 (2011), January, nr. 01, p. C01080–C01080
246. BALLABRIGA, R. ; CAMPBELL, M. ; HEIJNE, E. ; LLOPART, X. ; TLUSTOS, L. ; WONG, W.: Medipix3: A 64k pixel detector readout chip working in single photon counting mode with improved spectrometric performance. in: *Nuclear Instruments and Methods in Physics Research Section A: Accelerators, Spectrometers, Detectors and Associated Equipment* 633 (2011), May, p. S15–S18
247. HENRICH, B. ; BECKER, J. ; DINAPOLI, R. ; GOETTLICHER, P. ; GRAAFSMA, H. ; HIRSEMANN, H. ; KLANNER, R. ; KRUEGER, H. ; MAZZOCCO, R. ; MOZZANICA, A. ; PERREY, H. ; POTDEVIN, G. ; SCHMITT, B. ; SHI, X. ; SRIVASTAVA, A.K. ; TRUNK, U. ; YOUNGMAN, C.: The adaptive gain integrating pixel detector AGIPD a detector for the European XFEL. in: *Nuclear Instruments and Methods in Physics Research Section A: Accelerators, Spectrometers, Detectors and Associated Equipment* 633 (2011), May, p. S11–S14
248. POTDEVIN, Guillaume ; GRAAFSMA, Heinz: Analysis of the expected AGIPD detector performance parameters for the European X-ray free electron laser. in: *Nuclear Instruments and Methods in Physics Research Section A: Accelerators, Spectrometers, Detectors and Associated Equipment* 659 (2011), December, nr. 1, p. 229–236
249. THIL, Ch. ; BARON, A.Q.R. ; FAJARDO, P. ; FISCHER, P. ; GRAAFSMA, H. ; RÜFFER, R.: Pixel readout ASIC for an APD based 2D X-ray hybrid pixel detector with sub-nanosecond resolution. in: *Nuclear Instruments and Methods in Physics Research Section A: Accelerators, Spectrometers, Detectors and Associated Equipment* 628 (2011), February, nr. 1, p. 461–464
250. BACKHAUS, M. ; BARBERO, M. ; GONELLA, L. ; KNETTER, J. Groß e. ; HÜGGING, F. ; KRÜGER, H. ; WEINGARTEN, J. ; WERMES, N.: Development of a versatile and modular test system for ATLAS hybrid pixel detectors. in: *Nuclear Instruments and Methods in Physics Research Section A: Accelerators, Spectrometers, Detectors and Associated Equipment* 650 (2011), September, nr. 1, p. 37–40
251. WERMES, N.: PIXEL 2010 Resumé. in: *Nuclear Instruments and Methods in Physics Research Section A: Accelerators, Spectrometers, Detectors and Associated Equipment* 650 (2011), September, nr. 1, p. 245–252

252. FULLAGAR, Wilfred ; UHLIG, Jens ; WALCZAK, Monika ; CANTON, Sophie ; SUNDSTRÖM, Villy: *The use and characterization of a backilluminated charge-coupled device in investigations of pulsed x-ray and radiation sources.*, 2008. (10) . – 103302 S. – This content was modified and reprinted with permission from this source. Copyright 2008 American Institute of Physics
253. LALENA, John N.: From quartz to quasicrystals: probing nature's geometric patterns in crystalline substances. in: *Crystallography Reviews* 12 (2006), nr. 2, p. 125–180
254. TOMMASINI, R ; BRUCH, R ; FILL, E ; BJEUMIKHOV, A: Convergent-beam diffraction of ultra-short hard X-ray pulses focused by a capillary lens. in: *Applied Physics B-Lasers and Optics* 82 (2006), nr. 4, p. 519–522
255. THOE, Robert: High-resolution spectrometer design using spherically curved crystals. in: *Journal of the Optical Society of America A* 3 (1986), September, nr. 9, p. 1407
256. HALL, T A.: A focusing X-ray crystal spectrograph. in: *Journal of Physics E: Scientific Instruments* 17 (1984), February, nr. 2, p. 110–112
257. KOPIETZ, P ; SCHARF, P ; SKAF, MS ; CHAKRAVARTY, S: A focusing Crystal von Hamos Spectrometer for X-ray Spectroscopy and X-ray Fluorescence Applications. in: *Advances in Laboratory-based X-Ray Sources and Optics* 4144 (1989), p. 148–154
258. MARTINOLLI, E. ; KOENIG, M. ; BOUDENNE, J. M. ; PERELLI, E. ; BATANI, D. ; HALL, T. A.: Conical crystal spectrograph for high brightness x-ray $K\alpha$ spectroscopy in subpicosecond laser-solid interaction. in: *Review of Scientific Instruments* 75 (2004), nr. 6, p. 2024
259. LEVY, A ; DORCHIES, F ; FOURMENT, C ; HARMAND, M ; HULIN, S ; SANTOS, J J. ; DESCAMPS, D ; PETIT, S ; BOULLAUD, R: Double conical crystal x-ray spectrometer for high resolution ultrafast x-ray absorption near-edge spectroscopy of Al K edge. in: *The Review of scientific instruments* 81 (2010), June, nr. 6, p. 063107
260. SHYMANOVICH, U ; NICOUL, M ; LU, W ; KÄHLE, S ; TARASEVITCH, A ; SOKOLOWSKI-TINTEN, K ; LINDE, D von d.: Toward ultrafast time-resolved Debye-Scherrer x-ray diffraction using a laser-plasma source. in: *The Review of scientific instruments* 80 (2009), August, nr. 8, p. 083102
261. HAUER, A. ; KILKENNY, J. D. ; LANDEN, O. L.: Toroidally curved crystal for time-resolved x-ray spectroscopy. in: *Review of Scientific Instruments* 56 (1985), nr. 5, p. 803
262. MISSALLA, T. ; USCHMANN, I. ; FÖRSTER, E. ; JENKE, G. ; LINDE, D. von d.: Monochromatic focusing of subpicosecond x-ray pulses in the keV range. in: *Review of Scientific Instruments* 70 (1999), nr. 2, p. 1288
263. STEPANENKO, M.: A spectral resolution of Johann-type X-ray spectrometers. in: *Plasma Devices and Operations* 17 (2009), September, nr. 3, p. 191–200
264. SHEVELKO, A P. ; KASYANOV, Y S. ; YAKUSHEV, O F. ; KNIGHT, L V.: Compact focusing von Hamos spectrometer for quantitative x-ray spectroscopy. in: *Review of Scientific Instruments* 73 (2002), nr. 10, p. 3458–3463
265. LEGALL, H. ; STIEL, H. ; ARKADIEV, V. ; BJEUMIKHOV, A. A.: High spectral resolution x-ray optics with highly oriented pyrolytic graphite. in: *Optics Express* 14 (2006), nr. 10, p. 4570

-
266. BILDERBACK, D. ; LAIRSON, B. ; BARBEE JR., T. ; ICE, G. ; SPARKS JR., C. J.: Design of doubly focusing, tunable (5-30 keV), wide bandpass optics made from layered synthetic microstructures. in: *Nuclear Instruments and Methods in Physics Research* 208 (1983), nr. 1-3, p. 251–261
267. ERKO, A. ; FIRSOV, A. ; HOLLACK, K. ; GARRETT, R. ; GENTLE, I. ; NUGENT, K. ; WILKINS, S.: New Developments in Femtosecond Soft X-ray Spectroscopy. in: *SRI 2009, 10TH international conference on radiation instrumentation*, SRI, 2010, p. 177–180
268. WILHEIN, T. ; REHBEIN, S. ; HAMBACH, D. ; BERGLUND, M. ; RYMELL, L. ; HERTZ, H. M.: A slit grating spectrograph for quantitative soft x-ray spectroscopy. in: *Review of Scientific Instruments* 70 (1999), nr. 3, p. 1694
269. DAIDO, Hiroyuki: Review of soft x-ray laser researches and developments. in: *Reports on Progress in Physics* 65 (2002), October, nr. 10, p. 1513–1576
270. HEIMANN, Philip A. ; KOIKE, Masato ; PADMORE, Howard A.: Dispersive x-ray absorption spectroscopy with gratings above 2 keV. in: *Review of Scientific Instruments* 76 (2005), nr. 6, p. 063102
271. ULLOM, J. N. ; BEALL, J. A. ; DORIESE, W. B. ; DUNCAN, W. D. ; FERREIRA, L. ; HILTON, G. C. ; IRWIN, K. D. ; REINTSEMA, C. D. ; VALE, L. R.: Optimized transition-edge x-ray microcalorimeter with 2.4 eV energy resolution at 5.9 keV. in: *Applied Physics Letters* 87 (2005), nr. 19, p. 194103
272. MOORE, Gordon E.: Cramming more components onto integrated circuits, Reprinted from *Electronics*, volume 38, number 8, April 19, 1965, pp.114 ff. in: *IEEE Solid-State Circuits Newsletter* 20 (2006), September, nr. 3, p. 33–35
273. IRWIN, Kent D. ; YOUNG, Betty ; CABRERA, Blas ; MILLER, Aaron: Shannon Limits for Low-Temperature Detector Readout. in: *The thirteenth international workshop on low temperature detectors -LTD13* vol. 1185, 2009. – ISBN 978-0-7354-0751-0, p. 229–236
274. reproduced with permission from Jochem Baselmans (*LTD-14 conference, Heidelberg 2011*), with minor modification
275. DORIESE, W. B. ; ADAMS, J. S. ; HILTON, G. C. ; IRWIN, K. D. ; KILBOURNE, C. A. ; SCHIMA, F. J. ; ULLOM, J. N. ; YOUNG, Betty ; CABRERA, Blas ; MILLER, Aaron: Optimal filtering, record length, and count rate in transition-edge-sensor microcalorimeters. in: *The thirteenth international workshop on low temperature detectors -LTD13* vol. 1185, 2009. – ISBN 978-0-7354-0751-0, p. 450–453
276. *International X-ray Observatory (IXO)*.
<http://ixo.gsfc.nasa.gov/whatIsIxO.html>, last checked: 2011.12.05
277. KILBOURNE, Caroline A. ; DORIESE, W. B. ; BANDLER, Simon R. ; BREKOSKY, Regis P. ; BROWN, Ari-David ; CHERVENAK, James A. ; ECKART, Megan E. ; FINKBEINER, Fred M. ; HILTON, Gene C. ; IRWIN, Kent D. ; IYOMOTO, Naoko ; KELLEY, Richard L. ; PORTER, F. S. ; REINTSEMA, Carl D. ; SMITH, Stephen J. ; ULLOM, Joel N.: Multiplexed readout of uniform arrays of TES x-ray microcalorimeters suitable for Constellation-X. in: *Proceedings of SPIE* vol. 7011, SPIE, 2008, p. 701104–701104–12
278. LANDAU, Lew D. ; LIFSCHITZ, Ewgeni M.: *Physikalische Kinetik, Lehrbuch der theoretischen Physik, 10 Bde.* vol. Bd.10. Berlin : Akademie-Verlag Berlin, 1990. – ISBN 3055000749
279. NYQUIST, H.: Thermal Agitation of Electric Charge in Conductors. in: *Physical Review* 32 (1928), July, nr. 1, p. 110–113

280. KITTEL, Charles: *Einführung in die Festkörperphysik*. München : Oldenbourg, 2006. – ISBN 3486577239
281. JOHNSON, J.: Thermal Agitation of Electricity in Conductors. in: *Physical Review* 32 (1928), July, nr. 1, p. 97–109
282. DELFT, Dirk van ; KES, Peter: The discovery of superconductivity. in: *Physics Today* 63 (2010), nr. 9, p. 38
283. BUZEA, Cristina ; ROBBIE, Kevin: Assembling the puzzle of superconducting elements: a review. in: *Superconductor Science and Technology* 18 (2005), January, nr. 1, p. R1–R8
284. SEIDEL, P. ; SCHMIDL, F. ; WALD, H. ; MANS, M. ; PEISELT, K. ; BALDEWEG, U. ; BECK, M. ; BIERING, S. ; BECKER, C. ; UHLIG, Jens ; GROSZLIGE, V.: Thin-Film Technology for HTSC Josephson Devices. in: *IEEE TRANSACTIONS ON APPLIED SUPERCONDUCTIVITY* 15 (2005), nr. 2, p. 161–164
285. BUCKEL, Werner: *Supraleitung (German Edition)*. Wiley-VCH, 2004. – 496 S. – ISBN 3527403485
286. TINKHAM, Michael ; PHYSICS: *Introduction to Superconductivity: Second Edition (Dover Books on Physics) (Vol i)*. Dover Publications, 2004. – 480 S. – ISBN 0486435032
287. POOLE, Charles P. J. ; FARACH, Horacio A. ; CRESWICK, Richard J. ; PROZOROV, Ruslan: *Superconductivity, Second Edition*. Academic Press, 2007. – ISBN 0120887614
288. MEISSNER, W. ; OCHSENFELD, R.: Ein neuer Effekt bei Eintritt der Supraleitfähigkeit. in: *Die Naturwissenschaften* 21 (1933), November, nr. 44, p. 787–788
289. GINZBURG, Vitaly L.: On superconductivity and superfluidity (what I have and have not managed to do), as well as on the ‘physical minimum’ at the beginning of the 21 st century. in: *Chemphyschem : a European journal of chemical physics and physical chemistry* 5 (2004), July, nr. 7, p. 930–45
290. GINZBURG, Vitaly L. ; LANDAU, Lew D.: On the theory of superconductivity. in: *Zhurnal Eksperimental’noi i Teoreticheskoi Fiziki (Journal of Experimental and Theoretical Physics)* 20 (1950), nr. 12, p. 1064
291. ABRIKOSOV, A.A.: On the Magnetic Properties of Superconductors of the Second Group. in: *Journal of Experimental and Theoretical Physics* 5 (1957), p. 1174
292. BARDEEN, J. ; COOPER, L. N. ; SCHRIEFFER, J. R.: Theory of Superconductivity. in: *Physical Review* 108 (1957), December, nr. 5, p. 1175–1204
293. MANDL, Franz: *Statistical physics*. 2nd. Chichester West Sussex New York : Wiley, 1988. – ISBN 0471915335
294. SZYMKOWIAK, A. E. ; KELLEY, R. L. ; MOSELEY, S. H. ; STAHL, C. K.: Signal processing for microcalorimeters. in: *Journal of Low Temperature Physics* 93 (1993), November, nr. 3-4, p. 281–285
295. ENSS, Ch.: *Cryogenic Particle Detection*. Berlin/Heidelberg : Springer-Verlag, 2005. – ISBN 3–540–20113–0
296. EFROS, A L. ; SHKLOVSKII, B I.: Coulomb gap and low temperature conductivity of disordered systems. in: *Journal of Physics C: Solid State Physics* 8 (1975), February, nr. 4, p. L49–L51

297. FRIEDRICH, Stephan ; FUNK, T. ; DRURY, O. ; LABOV, S. E. ; CRAMER, S. P.: A multichannel superconducting soft x-ray spectrometer for high-resolution spectroscopy of dilute samples. in: *Review of Scientific Instruments* 73 (2002), nr. 3, p. 1629
298. FRIEDRICH, Stephan: Cryogenic X-ray detectors for synchrotron science. in: *Journal of synchrotron radiation* 13 (2006), March, nr. Pt 2, p. 159–71
299. FRIEDRICH, Stephan ; DRURY, Owen B. ; HALL, John ; CANTOR, Robin ; GARRETT, R. ; GENTLE, I. ; NUGENT, K. ; WILKINS, S.: Development of Ta-based Superconducting Tunnel Junction X-ray Detectors for Fluorescence XAS. in: *SRI 2009, 10TH INTERNATIONAL CONFERENCE ON RADIATION INSTRUMENTATION*, 2010, p. 101–104
300. MAZIN, Benjamin A.: *Microwave kinetic inductance detectors*, California Institute of Technology, PhD Thesis, 2005. <http://resolver.caltech.edu/CaltechETD:etd-10042004-120707>
301. ULLOM, J. N. ; DORIESE, W. B. ; HILTON, G. C. ; BEALL, J. A. ; DEIKER, S. ; DUNCAN, W. D. ; FERREIRA, L. ; IRWIN, K. D. ; REINTSEMA, C. D. ; VALE, L. R.: Characterization and reduction of unexplained noise in superconducting transition-edge sensors. in: *Applied Physics Letters* 84 (2004), nr. 21, p. 4206
302. LINDEMAN, MA: *Microcalorimetry and the transition-edge sensor*, Univ. of California, Davis, CA (US), PhD Thesis, 2000. http://www.osti.gov/energycitations/product.biblio.jsp?osti_id=15009469
303. IRWIN, K. D. ; HILTON, G. C. ; WOLLMAN, D. A. ; MARTINIS, John M.: Thermal-response time of superconducting transition-edge microcalorimeters. in: *Journal of Applied Physics* 83 (1998), nr. 8, p. 3978
304. IRWIN, K. D.: An application of electrothermal feedback for high resolution cryogenic particle detection. in: *Applied Physics Letters* 66 (1995), nr. 15, p. 1998
305. SEIDEL, W. ; FORSTER, G. ; CHRISTEN, W. ; FEILITZSCH, F. von ; GOEBEL, H. ; PROEBST, F. ; MOESSBAUER, R.L.: Phase transition thermometers with high temperature resolution for calorimetric particle detectors employing dielectric absorbers. in: *Physics Letters B* 236 (1990), March, nr. 4, p. 483–487
306. CLARKE, John (Publ.) ; BRAGINSKI, Alex I. (Publ.): *The SQUID handbook*. Weinheim : Wiley-VCH, 2003. – ISBN 3527404082
307. IRWIN, K D. ; NIEMACK, M D. ; BEYER, J ; CHO, H M. ; DORIESE, W B. ; HILTON, G C. ; REINTSEMA, C D. ; SCHMIDT, D R. ; ULLOM, J N. ; VALE, L R.: Code-division multiplexing of superconducting transition-edge sensor arrays. in: *Superconductor Science and Technology* 23 (2010), March, nr. 3, p. 034004
308. REINTSEMA, C. D. ; ADAMS, J. S. ; BAKER, R. ; BANDLER, S. R. ; DORIESE, W. R. ; FIGUEROA-FELICIANO, E. ; HILTON, G. C. ; IRWIN, K. D. ; KELLY, R. L. ; KILBOURNE, C. A. ; KRINSKY, J. W. ; PORTER, F. S. ; WIKUS, P. ; YOUNG, Betty ; CABRERA, Blas ; MILLER, Aaron: Electronics for a Next-Generation SQUID-Based Time-Domain Multiplexing System. in: *The thirteenth international workshop on low temperature detectors -LTD13* vol. 1185, 2009, p. 237–240
309. Å STRÖM, K.J. ; MURRAY, R.M.: *Feedback systems: an introduction for scientists and engineers*. Princeton Univ Pr, 2008. – 424 S. – ISBN 0691135762
310. BENNETT, Stuart: *A History of Control Engineering 1930-1955*. (Iee Contr. Institution of Electrical Engineers, 1993. – 1993 S. – ISBN 0863412998

311. NOF, Shimon Y. (Publ.): *Springer Handbook of Automation*. Berlin, Heidelberg : Springer Berlin Heidelberg, 2009. – ISBN 978–3–540–78830–0
312. ADAMS, J. S. ; BANDLER, S. R. ; BROWN, L. E. ; BOYCE, K. R. ; CHIAO, M. P. ; DORIESE, W. B. ; ECKART, M. E. ; HILTON, G. C. ; KELLEY, R. L. ; KILBOURNE, C. A. ; PORTER, F. S. ; RABIN, M. W. ; SMITH, S. J. ; STEWART, D. D. ; ULLOM, J. N. ; YOUNG, Betty ; CABRERA, Blas ; MILLER, Aaron: Real-Time Data Processing for X-Ray Spectroscopy. in: *The thirteenth international workshop on low temperature detectors -LTD13* vol. 1185, 2009, p. 274–277
313. TAN, Hui ; BREUS, Dimitry ; HENNIG, Wolfgang ; SABOUROV, Konstantin ; WARBURTON, William K. ; DORIESE, W. B. ; ULLOM, Joel N. ; BACRANIA, Minesh K. ; HOOVER, Andrew S. ; RABIN, Michael W.: *High rate pulse processing algorithms for microcalorimeters*. IEEE, 2008. – 1130–1133 S.
314. GIFFORD, William E. ; R.C., Longsworth: Pulse Tube Refrigeration Progress. in: *International Advances in Cryogenic Engineering - Volume 10*. University of Pennsylvania, 1964
315. WAELE, A. T. A. M.: Basic Operation of Cryocoolers and Related Thermal Machines. in: *Journal of Low Temperature Physics* 164 (2011), June, nr. 5-6, p. 179–236
316. RADEBAUGH, R.: Development of the pulse tube refrigerator as an efficient and reliable cryocooler. in: *Proc. Institute of Refrigeration* vol. 2000. London, 1999
317. SHIRRON, Peter J.: Cooling Capabilities of Adiabatic Demagnetization Refrigerators. in: *Journal of Low Temperature Physics* 148 (2007), June, nr. 5-6, p. 915–920
318. SHULL, R. ; MCMICHAEL, R. ; RITTER, J.: Magnetic nanocomposites for magnetic refrigeration. in: *Nanostructured Materials* 2 (1993), March, nr. 2, p. 205–211
319. WOLF, B. ; TSUI, Y. ; JAISWAL-NAGAR, D. ; TUTSCH, U. ; HONECKER, A. ; REMOVIC-LANGER, K. ; HOFMANN, G. ; PROKOFIEV, A. ; ASSMUS, W. ; DONATH, G. ; LANG, M.: Magnetocaloric effect and magnetic cooling near a field-induced quantum-critical point. in: *Proceedings of the National Academy of Sciences* 108 (2011), April, nr. 17, p. 6862–6866
320. HÖLZER, G. ; FRITSCH, M. ; DEUTSCH, M. ; HÄRTWIG, J. ; FÖRSTER, E.: $K\alpha_{1,2}$ and $K\beta_{1,3}$ x-ray emission lines of the 3d transition metals. in: *Physical Review A* 56 (1997), December, nr. 6, p. 4554–4568
321. PORTER, F. S.: *private communication*. 2004. – remeasured and added 5899.417eV from Intensity 0.005 to .018 and adding 5902.712eV with I 0.004 and the width 1.5528
322. CHECHEV, V. P.: Certified Reference Tables on Decay Characteristics and Radiations of Radionuclides Used to Calibrate Semiconductor Spectrometers for Photon Radiation in the Energy Range 5-140 keV. in: *Measurement Techniques* 46 (2003), December, nr. 12, p. 1202–1206. <http://dx.doi.org/10.1023/B:METE.0000018733.56924.e2>. – DOI 10.1023/B:METE.0000018733.56924.e2
323. NOCKERT, Jens: (*working title*): *Features and Implementation of a parallelized optimal filter for dataprocessing of microcalorimeter data.*, Bachelor thesis. – defence Jan 20th 2012
324. KINNUNEN, K.: *Studies of Transition-edge Sensor Physics, Thermal Models and Noise*, University of Jyväskylä, PhD, 2011

ACKNOWLEDGMENTS

I owe my deepest gratitude to my thesis supervisor Professor Villy Sundström. His support and encouragement gave me the chance to develop into a new world of science and gain knowledge in a wide variety of topics that can not be sufficiently represented by this thesis. The german name for supervisor is "Doktorvater" (doctor father) and is definitely the best description for what you were. Supportive, encouraging and always there when needed to ask a question or to give me a little push in a better direction. Thank you Villy.

To Wilfred: "I just wanted to put this thought in your head" will be the sentence i gone miss most after this thesis. It would be hard to believe if somebody would say that there is a more dedicated and at the same time open minded scientist out there than Wilfred Fullagar. With his thinking "outside the box" and expertise in many a subject he is the mastermind behind much that was achieved in this project. Thanks for all your time, especially during the thesis writing weeks and your working "holidays". This thesis would not exist without you.

I am thankful to my opponent Professor Thomas Elsässer, and the thesis committee members: Professor Karin Schillén, Professor Tony Hansson and Professor Emad Mukhtar for accepting to evaluate this work.

I would like to thank Niklas Gador, Monika Walczak and Sophie Canton for their time and contributions to the project. Dimali Vithanage and Pavel Chabera had to fight the laser with me for many hours and i would like to thank them for their efforts and their friendship. Arkady Yartsev and Ivan Scheblykin had always an open ear and often just the right advice or lacking this a Russian joke that made things look brighter, thank you guys! Torbjörn Pascher deserves my gratitude for all the little electronic things he build and the hours we spent discussing. Yingyot, Thomas, Donatas, Ramunas, Oleg, Lotta Daniel, Tönu, Per and Ebbe and can only stand as examples for all the special peoples that are united in our department and i had the privilege to learn from. I enjoyed the time with all of you.

I would like to give my thanks to Professor Claes-Göran Wahlström for that we could perform the measurements at Lunds High Power Laser Facility and for some really interesting discussions and insights afterwards. I would like to thank Professor Anne L'Huillier who started and chaired the MAXLAS program that brought me to Lund and financed me the first years.

Marko Swoboda, Nino Cutic, Ralph Nüske, Guillaume Genoud, and Jörg Schwenke became much more than just fellows in the same European project. Thank you guys for all the nice hours. Thomas Björkman, Maria Levin, Jan Wegner, Anki Wikander, Tommy Ljungdell, Stefan Jonason and Rickard Holst took care of all the administrative sides and are as important to any science.

Kimmo Kinnunen and Ilari Maasilta brought us into the game of low temperature detectors and shall be thanked for this. Kimmo, it was quite a time in Boulder. Thanks for all the help and company.

I would like to thank the whole team in Boulder that built this nice detector for and with me. Joel Ullom, Randy Doriese, Dan Swetz and Joe Fowler traveled all the way over the big lake and carried the largest piece of work while developing this system. Joe and Joel you had to stand all my questions and demands during the last month, thanks for staying so patient. I'm looking forward to work with you guys.

My thanks goes also to the MAXLAS project that financed me the first years and to Villy who used parts of his ERC grant to support this research.

My special thanks to my new family Eriksson that gave me a home in this country from the very beginning.

Lisa, how many time have I been frustrated and found a save haven at home with you. Where would SAM be without you? I hope we hold together for the good and bad times that might come. I love you.

Last but not least: Mutsch, Pa, es ist ein tolles Gefühl zu wissen, das man immer eine Stelle in der Welt hat an der man zu Hause ist. Was auch immer ich für verrückte Pläne auheckte, es gab immer Euch, mit Eurer Liebe und Unterstützung. DANKE!

COMMENTS ON THE PAPERS

I A broadband laser plasma x-ray source for application in ultrafast chemical structure dynamics.

I took part in most of the experiments and contributed substantial parts to the manuscript.

II The use and characterization of a backilluminated charge-coupled device in investigations of pulsed x-ray and radiation sources.

I took major part in all experiments and contributed substantial parts to the manuscript.

III Lab-based Ultrafast Molecular Structure

I took major part in all experiments and contributed to the manuscript.

IV Laser generated 300 keV electron beams from water

I was responsible for the experiments, data analysis and writing of the manuscript.

V Table-top ultrafast x-ray microcalorimeter spectrometry for molecular structure

I was responsible for the experiments, data analysis and writing of the manuscript.

PAPERS

PAPER I

A broadband laser plasma x-ray source for application in ultrafast chemical structure dynamics.

W. Fullagar, M. Harbst, S. Canton, J. Uhlig, M. Walczak,
C.-G. Wahlström, V. Sundström.

Review of Scientific Instruments **78(11)**, 115105 (2007).

PAPER II

The use and characterization of a backilluminated charge-coupled device in investigations of pulsed x-ray and radiation sources.

W. Fullagar, J. Uhlig, M. Walczak, S. Canton, I. Maasilta, V. Sundström.
Review of Scientific Instruments **79(10)**, 103302 (2008).

PAPER III

Lab-based Ultrafast Molecular Structure

W. Fullagar, J. Uhlig, N. Gador, K. Kinnunen, I. Maasilta,
C.-G. Wahlström, V. Sundström.

AIP Conference Proceedings **1234(1)**, 919-922 (2010).

PAPER IV

Laser generated 300 keV electron beams from water

J. Uhlig, C.-G. Wahlström, M. Walczak, V. Sundström, W. Fullagar.

Laser and particle beams **29-4**, 415-424(2011).

PAPER V

Table-top ultrafast x-ray microcalorimeter spectrometry for molecular structure

J. Uhlig, W. Fullagar, J. Ullom, W.B. Doriese, N. Gador, S. Canton,
K. Kinnunen, J. Fowler, C. Reintsema, D. Swetz, D. Bennett, G. Hilton,
K. Irwin, D. Schmidt, V. Sundström.

Physical Review Letter **110(13)**, 138302(2013).

